NTNU – Trondheim
Norwegian University of
Science and Technology

Laboratory Demonstration of Provision of Primary Frequency Control Services from VSC-HVDC Connected Wind Farms

Hanne Støylen

Master of Energy and Environmental Engineering
Submission date: June 2014
Supervisor: Kjetil Uhlen, ELKRAFT
Co-supervisor: Kamran Sharifabadi, Statoil ASA

Norwegian University of Science and Technology
Department of Electric Power Engineering

Acknowledgements

I would like to thank my supervisor, Professor Kjetil Uhlen, for his valuable supervision and guidance. I strongly appreciate his encouragement in letting me find my own way, and supporting me all the while. Special gratitude goes to my co-supervisor, Dr. Kamran Sharifabadi, who has a one-of-a-kind understanding of electrical components and how they interact in the power system. His advice on my research has been essential and treasured. I would also like to thank Dr. Olimpo Anaya-Lara for taking the time to visit and evaluate the laboratory set-up, and for valuable discussions on key findings. Further, I would like to express my deepest appreciation to my partner, Atle, for the love and support he has given me during my entire time at NTNU. I feel blessed to have him in my life, and I am very grateful that we can share so much of our work-life together. His advise on my work has been invaluable. In addition, I would like to thank Kalle Teearu, Tommy Berre, Kjell Ljoekelsoey, and others on SINTEF/NTNU that have contributed to the development of the laboratory set-up. I would like to thank my friends for all the good times we've had during our spare times. Last but not least, I want to thank my family for their unconditional love.

Abstract

Frequency control is a particularly significant issue with high levels of rotating generating units interfaced with power electronics in the power system. Since the power electronic converter decouples the generating unit from the grid, the generating unit will not inherently participate in the regulation of grid frequency. This is often referred to as a reduction of the system inertia. A lower level of system inertia leads to a worsened frequency response following an imbalance between power generation and load. With an increasing integration of renewable energy, and a growing interest in power transmission technologies that require power electronic interfaces such as HVDC, it is likely that grid operators will require services such as inertia provision from future VSC-HVDC connected power plants.

In this thesis a communication-less method for obtaining inertial response from a VSC-HVDC connected wind farm is proposed and verified experimentally. A simplified sketch of the laboratory set-up used in the experiments can be seen in Figure 1. An induction motor-generation set is used as a wind farm equivalent and a synchronous generator together with a transmission line equivalent is used to represent a weak AC grid. The wind farm equivalent and the weak grid are interconnected through a DC network using two VSC converters. The DC cables are modelled as resistances. Some simplifications are made regarding modelling of the wind farm. The generator representing the wind farm is directly connected to the HVDC converter terminal VSC_A. In other words, the wind farm collection grid and the turbine frequency converter are neglected. In a real system, the frequency converter in the turbines would directly relate to the kinetic energy stored in the rotating parts of the wind turbine, whereas the converter control in VSC_A modifies the frequency in the collection grid.

The objective of the work is to enhance the frequency control in the weak grid following a disturbance in the power balance by emulating an inertial response from the VSC-HVDC connected wind farm. This is done by implementing additional controls in the VSC converter terminals. On the weak grid connected converter, the control relates the DC voltage $V_{DC,B}$ to changes in system frequency f_{WG}. Further, the control on the wind farm connected converter relates changes in DC voltage $V_{DC,A}$ to changes in the electrical torque reference T_e in the wind turbines.

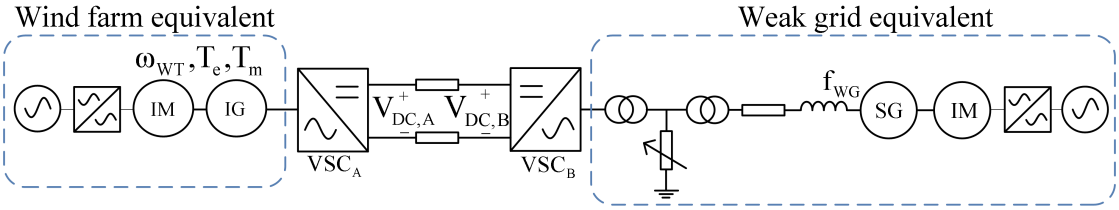

Figure 1: The system studied in this thesis.

This approach provides a coupling of the inertia of the wind turbines and the weak grid. During frequency changes in the weak grid, the wind farm equivalent will absorb or release kinetic energy. This behaviour is referred to as inertial response. In addition to the laboratory model, a Matlab/Simulink model is developed for comparison purposes and for evaluating the effect of changing key parameters in the proposed control system.

The results show that the inertial response from the wind farm has a beneficial impact on the frequency response in the weak grid during the transient event following a power imbalance. The wind farm equivalent is able to modify the frequency low-point and the time at which it occurs. In the best case the first frequency dip is reduced from 3.7 Hz to 2.5 Hz, which corresponds to an improvement of 48.2 % based on the steady-state frequency deviation. The first dip is also delayed in time with approximately 1.3 seconds, compared to base case. In addition, the effect of varying control system parameters was extensively investigated. It is found that the main constraint to the amount of inertial support possible to obtain in the laboratory model is the stability of the system. Also, the performance of the controls is limited by significant time delays associated with filtering. Further studies should investigate the possibility of adding an additional VSC terminal to the DC network. Also, some thought should be put into methods to increase the efficiency of the control system by for instance reducing the filter time constants. In addition, an optimization of key control parameters and the combination of these, should be made.

Samandrag

Frekvenskontroll er viktig i kraftnett der store delar av kraftproduksjonen er integrert ved hjelp av kraftelektronikk (KE). Sidan eit KE-grensesnitt gjer at rotasjonssnøggleiken til den kraftproduserande eininga er uavhengig av frekvensen til kraftnettet den er kopla til, vil produksjonseininga ikkje automatisk delta i regulering av nettfrekvensen. Dette vert ofte referert til som ein reduksjon av kraftnettet sin tråleik. Eit lågare nivå av tråleik fører til ein forverra frekvensrespons etter ein ubalanse mellom kraftproduksjon og last. I samband med ein aukande integrasjon av fornybar energi, og ei aukande interesse for kraftoverføringskonfigurasjonar som krev KE-grensesnitt, t.d. likestraumsoverføring (HVDC), er det sannsynleg at nettselskap vil kunne krevje frekvenskontrolltenester også frå VSC-HVDC-tilkopla krafteiningar.

Denne avhandlinga foreslår ein kommunikasjonslaus metode for å utnytte rotasjonstråleiken til ein VSC-HVDC tilkopla vindpark til frekvensstøtte i nettet. Metoden er også validert i eit laboratorieoppsett. Ei forenkla skisse av laboratorieoppsettet som er brukt i eksperimenta kan sjåast i Figur 2. Eit induksjons-motor-generator-sett representerer vindparken, medan ein synkrongenerator saman med ein transmisjonslinje-ekvivalent representerer eit svakt vekselstraumsnett. Vindparken og vekselstraumsnettet er kopla saman gjennom ein likestraumskabel ved å bruke to spenningsstyrte omformarar (VSC-ar). Likestraumskablane er modellert med motstandar. I samband med modellering av vindparken er det gjort nokre forenklingar. Generatoren som representerer vindparken er direkte kopla til omformarterminalen VSC_A. Intern-nettet og vindturbinomformaren er med andre ord neglisjert. I eit ekte system vil turbintransformatoren i turbinane vere direkte knytta til rotasjonsenergien lagra i vindturbinen, medan kontrollen i VSC_A er knytta til frekvensen i internnettet.

Målet med arbeidet er å forbetre frekvenskontrollen i vekselstraumsnettet etter ein kraftubalanse ved å etterlikne ein tråleiksrespons frå den likestraumstilkopla vindparken. Dette vert gjort ved å implementere ytre kontrollsløyfer på dei spenningsstyrte omformarane. Kontrollen i omformaren som er kopla til vekselstraumnettet relaterer likespenning VSC_B til endringar i f_{WG}. Kontrollen i omformaren som er kopla til vindparken knyttar endring i likespenning VSC_A til endringar i

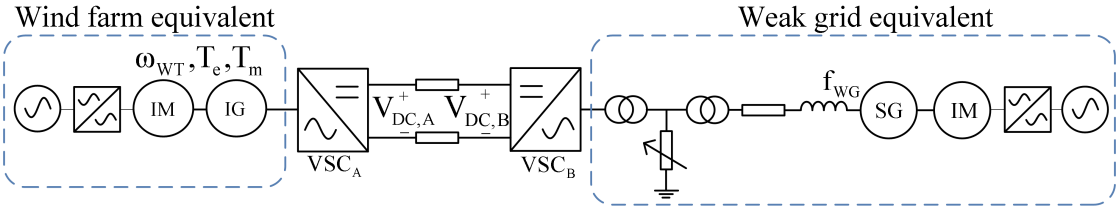

Figur 2: Systemet som vert studert i denne oppgåva.

momentreferansen T_e i vindturbinane. På denne måten vert vindparken sin rotasjonstråleik kopla til vekselstraumnettet. Når det skjer ei endring i frekvensen i nettet, vil vindparkekvivalenten reagere ved å absorbere eller avgje kinetisk energi. Denne oppførselen vert kalla vindparkekvivalenten sin tråleiksrespons. I tillegg til laboratoriemodellen, er ein Matlab/Simulink-modell utvikla for samanlikning og for å vurdere effekten av å endre viktige parametrar i det føreslåtte styresystemet.

Resultata viser at tråleiksresponsen frå vindparken har ein gunstig innverknad på frekvensresponsen til vekselstraumsnettet som følgjer av kraftubalansen. Ein kan sjå at både lågpunktet i frekvensresponsen og tida når denne oppstår vert tydeleg forbetra. Den beste forbetringa i lågpunktet vart observert til å vere 48.2 %, med en forbetring i tid på 1.3 sekund, samanlikna med responsen utan støtte frå vindparken. Effekten av å variere nokre av dei viktigaste parametrane i styresystemet er òg undersøkt. Det er funne at den største avgrensinga i kor mykje frekvensresponsen kan forbetrast er stabiliteten til systemet, i tillegg til betydelige tidsforseinkingar i samband med implementerte filter. Vidare studiar bør undersøke moglegheita for å legge til ein ekstra omformarterminal i likestraumsnettverket. I tillegg kan det arbeidast med å gjere kontrollane meir effektive, ved til dømes å redusere filtertidskonstantar. Ei optimering av sentrale styringsparameterar og kombinasjonen av desse, er òg føreslått som vidare arbeid.

Abbreviations

Abbreviation	
AC	Alternating current
AVR	Automatic voltage regulator
B2B	Back-to-back
DAQ	Data acquisition device
DC	Direct current
DCNO	DC network operator
DSO	Distribution system operator
EURELECTRIC	The union of the electricity industry
ENTSO-E	European network of transmission system operators for electricity
FCR	Frequency containment reserve
HVDC	High voltage direct current
IE	Inertia emulation
MTDC	Multi-terminal direct current
PE	Power electronics
PLL	Phase locked loop
ROCOF	Rate-of-change-of-frequency
SP	Set-point
TSO	Transmission system operator
VSC	Voltage source converter
WG	Weak grid
WT	Wind turbine

Contents

List of Figures

List of Tables

1. Introduction

1.1 Background and motivation

One of the most important operational targets in a power system is to maintain a perfect balance between power production and power consumption at all times. In AC systems, the frequency indicates the energy balance. Following a load imbalance leading to a deficit of power, the system frequency will fall. Typically the frequency reaches its lowest point 5 to 10 seconds after the disturbance [1]. For conventional utilities to be allowed to connect to a power grid, in most situations, the grid operator requires that the power plant is able to provide primary frequency support to contain or restore the frequency during or after a load imbalance. A commonly used term for such supportive actions is "ancillary services".

High voltage direct current (HVDC) is presently being considered the most suitable technology for long-distance bulk power transmission. It is also favourable compared to AC for integration of large-scale offshore wind power plants located far from shore [2]. There are even ambitions of developing HVDC grids, called multi-terminal DC grids, to facilitate more integration of renewable energy, and increase the transmission capacity for balancing services and power trading [3]. Power electronics play an important role in integration of DC transmission systems and renewable energy, as they are essential to ensure high efficiency and performance [4]. Due to its flexibility and wide range of possible control objectives, the voltage-source-converter (VSC) is considered to be the most viable converter technology in the context of multi-terminal HVDC grids [3]. However, since the DC link in the VSC fully decouples the AC side power system from the power generating unit on the other side, the predicted integration of power electronics following the integration of DC systems and wind energy, may lead to frequency stability issues in the AC system they are interfaced with.

Traditionally, wind power has not been required to provide ancillary services, as most wind turbines do not automatically provide grid services that are available with conventional generators. However, since the amount of wind and other renewables are increasing, system operators have started to impose new requirements for future wind plant installations to be capable of, for instance, frequency regulation services. Otherwise, the frequency might exceed given limits and the grid stability might be compromised. Grid codes are becoming more demanding, and some are requiring that the wind turbines behave as conventional power plants and take an active role in network operation [5].

Inertia support is the fastest supportive action for contributing in power balance. Conventional power plants with synchronous generators have a large rotational energy that will automatically support the grid when the frequency changes. This is a property that is beneficial to maintain also with a higher percentage of power electronic interfaces in the system. The inertial response is highly influenced by integrating renewables, and with an increase of renewable energy sources in the power systems, the methods for maintaining the system frequency may need to be redefined [6]. Since the power electronic interface creates an electrical decoupling of the power generation unit and the AC grid, the generating unit is not allowed a direct implementation of inertial support. Therefore, inertia support from power electronic interfaces must be realised through control systems. In the context of multi-terminal DC grids and DC connected wind farms, this is challenging since the inertia support must be activated within a few seconds. Today, there exist no unified method for delivering inertial support from DC-transmission systems.

1.2 Scope of work

The objective of this thesis is to investigate the topic of exchange of primary frequency control services from VSC-HVDC connected wind farms. A two-terminal HVDC grid, connecting a wind farm with variable speed wind turbines and a weak AC grid, is used to analyse the possibility of inertial support during a load imbalance event. Previous works have demonstrated frequency response from wind farms and variable speed wind turbines [7, 8, 9]. Some works have also focused on frequency response from HVDC connected wind farms [10, 11]. This work focuses on the control strategies on the HVDC VSC converter terminals. Similar control strategies have been investigated in [2, 12].

The power electronic interface that is part of the HVDC network separates the wind farm from the AC grid in such a way that the wind farm will not automatically respond to changes in the system frequency. To achieve an inertial response from the VSC-HVDC connected wind farm, it is necessary to implement additional controls. In this thesis, an inertial response control is proposed. The goal is to contribute to reducing the rate-of-change-of-frequency and limit the frequency dip in the AC grid during the occurrence of a significant load imbalance. The control strategy should be flexible towards integrating additional terminals in the DC network. This is a important step towards being able to fulfil future grid requirements for HVDC connected power modules.

1.3 System description

Figure 3 shows a sketch of the system that is studied in this work. The laboratory model is made of two VSC terminals in which one is connected to a wind farm equivalent, and the other is connected to an AC island grid, also called a weak grid. The DC cables are modelled as resistances. Some simplifications are made regarding modelling of the wind farm. The generator representing the wind farm is directly connected to the HVDC converter terminal VSC_A. Hence, the wind farm collection grid and the turbine frequency converter are neglected. The control strategy for emulating an inertial response from the wind farm equivalent during a load imbalance in the weak grid is implemented on the VSC-HVDC converter terminals, VSC_A and VSC_B.

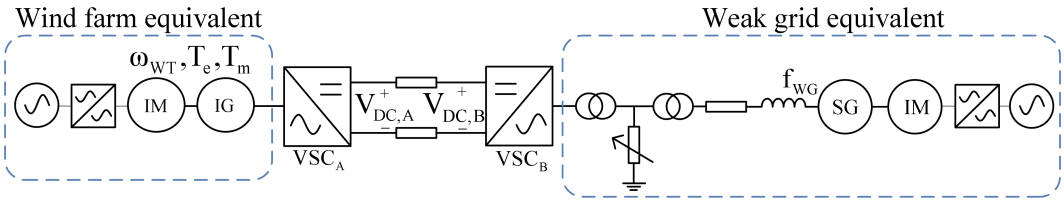

Figure 3: The system studied in this thesis.

1.4 Outline of thesis

Originally, the intent was to investigate primary frequency control services in the context of multi-terminal HVDC grids. This would serve as an extension of the work performed in the specialization project report [3]. Due to time consuming technical challenges in the lab, mainly regarding measurement techniques and limitations of equipment, the scope of work was revised to only consider a two-terminal HVDC configuration. Some parts of the original plan is suggested as further work in Chapter 9.

As mentioned in the introduction, grid codes concerning HVDC connections will become more demanding in the future, and it is likely that VSC-HVDC connected power plants and power grids will be required to provide ancillary services. In Chapter 2 some notions regarding system services and ancillary services in the context of HVDC grids are presented. Chapter 3 encompasses the possibility of exchanging frequency containment reserves through HVDC grids. Here, basic theory regarding inertia in power systems can be found. Chapter 4 concerns modelling and control of the voltage-source-converter, and is meant to give the reader a basic understanding of modelling aspects related to this converter technology that is considered to be most suitable for HVDC grids. Proposed converter control

strategies for emulating inertial response are presented in Chapter 5. Ultimately, the laboratory model and the simulation model are presented in Chapter 6 and Chapter 7, respectively. A great effort was put into developing a simulation model in Matlab/Simulink to be used for comparison purposes and sensitivity analysis of key parameters. Validation of the simulation model is made in Chapter 7. Additionally, simplifications that were made and challenges with the laboratory set-up are highlighted and discussed. In Chapter 8 results from selected case studies are shown. In the last part of this chapter, sensitivity analyses of key parameters are presented, and a discussion is made on the overall performance of the control system.

1.4.1 Relation to specialization project

This thesis is an extension of the work that was done as part of the "specialization project" at NTNU in the fall of 2013 [3]. The project report was titled "Laboratory Demonstration of an Offshore Grid in the North Sea with DC Droop Control". Due to the relation with some parts of the work in the thesis, some of the material from the specialization project has been utilized. This includes the following sections:

- Chapter 4: Modelling and Control of VSC
- Section 5.2: State-of-the-art control strategies for MTDC grids

1.5 Publication of results

A paper based on the results from the work performed in the fall of 2013 as part of the specialization project course at NTNU, was submitted to the Ninth International Conference on Ecological Vehicles and Renewable Energies. The co-authors were Atle Rygg Årdal (SINTEF Energy Research), Kamran Sharifabadi (Statoil ASA) and Prof. Kjetil Uhlen (NTNU). The paper was presented in Monaco on March 26 in 2014 and can be seen in Appendix 10.9. The paper was also invited for submission to the IEEE Transactions on Industry Applications and is currently under review.

2. Trading System Services through HVDC grids: DC grid Ancillary Services

2.1 Definition of concepts

In order to maintain a high degree of reliability, guarantee security of supply to end users, and to increase the stability of AC transmission systems, grid connected generating units provide ancillary services to the grid operator. In this context, the grid operator will be referred to as the transmission system operator (TSO) or distribution system operator (DSO). The provided services are related to system functioning, and Eurelectric describes them as follows [13]:

*"**Ancillary services** are all services required by the transmission or distribution system operator to enable them to maintain the integrity and stability of the transmission or distribution system as well as the power quality."*

What is considered ancillary services in particular, differs depending on the relevant TSO. Nevertheless, frequency control and voltage control are considered ancillary services in most countries. However, in an AC transmission system, it is not only the users or stakeholders that can contribute to maintaining a reliable operation of the system. The TSO or DSO can also offer services which enhance stability. If such services are offered from system operator to system users, such as a power plant owner, they are called system services. Eurelectric distinguished between system services and ancillary services as follows [13]:

*"**System services** are all services provided by some system function (such as a system operator or a grid/network operator) to users connected to the system. **Ancillary services** are services procured by a system functionality (system operator or grid/network operator) from system users in order to be able to provide system services."*

Most of the ancillary services are set as requirements in grid codes. This means that they are required by the TSO or DSO to keep the system frequency and voltages within operational limits or to help restore the system in case of a large

disturbance or an outage. However, some ancillary services are paid for, and there are even markets to trade some of them. Which services are mandatory and which are incentive based (paid for) depends on the relevant grid code. Table 1 gives an overview of the which ancillary services are mandatory (M) and which are not for some selected European countries. Not all the listed services are defined as ancillary services in all countries. These are marked "NA" in the table.

Table 1: An overview of which ancillary services that are considered mandatory (M) in European countries. "NA" means that that it is not considered as ancillary service in the particular country [13].

Service	**Norway**	**Denmark**	**Germany**	**UK**
Frequency control	M	M	M	M
Voltage control	M	M	M	M
Spinning reserve		M	M	NA
Standing reserve		M	M	
Black start capability	NA	M	M	
Remote automatic generation control	NA	NA	M	NA
Grid loss compensation	NA	NA	M	NA
Emergency control actions	NA	NA	M	NA

The above-mentioned definitions of ancillary services apply to AC grid transmission systems and AC grid connected stakeholders. The question is, how would the interaction between the AC grids change if they were connected through a HVDC network? With the increased interest in DC grids for bulk power transmission between AC systems, this question becomes increasingly relevant. It is possible to operate HVDC systems solely based on the objective of transferring a certain amount of power from point A to point B. This does not require advanced control strategies for services intended to enhance AC system functioning. However, the voltage source converter (VSC), which is considered to be the most viable technology in the context of HVDC grids, can satisfy a wide range of control objectives [14]. For instance, it is possible to control real and reactive power independently at its terminals. If taking advantage of this flexibility offered from the VSC, a HVDC grid can offer ancillary services to interconnected AC grids. Given this potential for HVDC grids to improve operation of interconnected AC systems, this chapter addresses the opportunity of exchange of ancillary and system services between AC systems interconnected through a multi-terminal HVDC grid.

2.2 Independent operation of multi-terminal DC grids

Few works have been published that address the issue of who will operate the multi-terminal HVDC grids that are planned in the future. For point-to-point HVDC connections that interconnects two TSOs, it might be mutually beneficial to have a shared operational responsibility. One reason for this can be that in case of a fault that leads to shut down of the DC-link it will affect both TSOs. This makes it a mutual interest to make investments and decisions that secure a stable operation of the DC cable. In a multi-terminal DC grid the situation is somewhat different, since a coordinated operation becomes more challenging with more than two terminals. In [15] three different types of multi-terminal HVDC grid operators are discussed. These are:

- **Coordinated operation** of the grid through an entity consisting of members from each interconnected TSO that aims to operate the grid such that it benefits all members.
- **Independent operation** of the network by an self-sufficient entity, independent of all TSOs, that aims to operate the HVDC network to maximize its own operational benefits.
- **Integrated operation** of the network where the DC grid becomes an expanded part of one of the interconnected AC systems.

In relation to ancillary services, a coordinated operation of the DC network can be most challenging since all decisions should benefit all members of the entity, i.e. the TSOs. As discussed earlier in this chapter, the interconnected AC systems might have different definitions on which services are considered ancillary and which are not. This can make it difficult to harmonize the viewpoints of every TSO. An integrated operation makes it easier to control the network as the control objective will be to satisfy one single TSO. However, it may not produce incentives to why other TSOs should be part of the DC grid. The TSO in charge will operate the grid such that it benefits the operation of its AC system, not considering the profit of the other TSOs. Having an independent entity that controls the HVDC grid may be the best fitted solution. The entity would have to operate in accordance with rules and the economic policies of each interconnected TSO, but it would seek to maximize its own profit. It is assumed that this will facilitate an operation based on demand and supply of services, which is considered to be a good solution from a socio-economic viewpoint. The remaining part of this chapter discusses ancillary and system services in the context of having independent operation of HVDC grids and a DC network operator.

2.3 The DC network operator

It is proposed that the integrated operation entity is referred to as the DC network operator (DCNO [1]), and that it is responsible for the DC transmission network as well as the VSC converters.

From the AC TSO point of view the HVDC grid is a system user, similar to a conventional power plant. Hence, the DC Network might be subjected to grid codes resemblant to those who apply to conventional power plants, and the DCNO should be able to offer ancillary services to the AC system in the same manner. In addition, the AC system should be able to provide system services to the DC grid such that the DCNO is able to maintain reliable operation of the DC grid. Other contributors to system services might be DC components connected to the DC grid, for instance battery storages. It is suggested that the DCNO should be able to manage and trade system services between TSOs. The obtained system services will serve as the DCNOs product range, which can further be offered as ancillary services to the TSOs individually. Trading system services from AC grids as ancillary services is where the DCNO obtains its revenues. The flow of ancillary and system services between the DCNO and interconnected TSOs is explained in Figure 4.

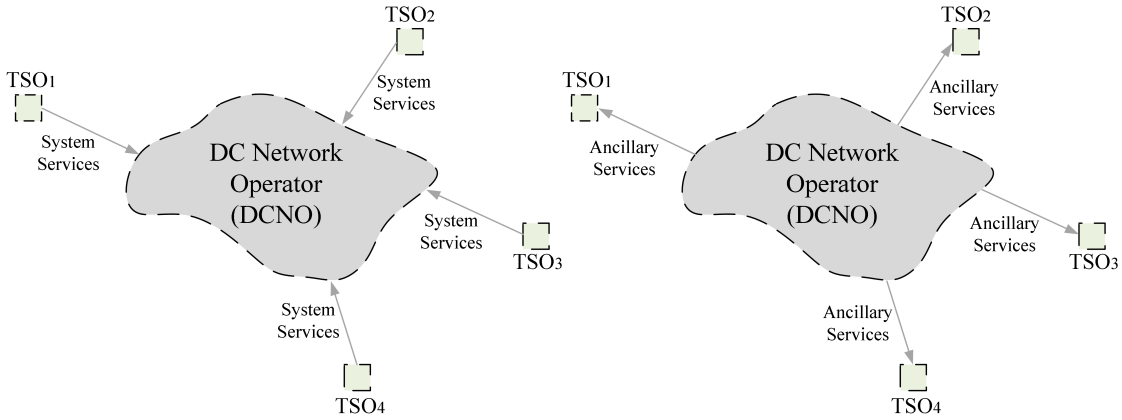

Figure 4: The flow of ancillary and system services between the TSOs and the DCNO. The left figure shows the flow of system services from the TSOs to the DCNO, and the right figure shows the flow of ancillary services from the DCNO to the individual TSOs. The DCNO can trade system services from one TSO as ancillary services to another TSO.

[1] Abbreviation proposed in this thesis

The DCNO should provide ancillary services to the TSOs in terms of maintaining the system frequency, voltages and stability as well as restarting the system under certain circumstances. It is proposed to refer to these services as DC grid ancillary services, and they are defined as follows [2]:

DC Grid Ancillary Services *are all services that the DC Network Operator (DCNO) can offer to an AC Transmission System Operator (TSO). These can either be required or paid for by the TSOs, and is either obtained through trade with other TSOs or supplied locally by an HVDC converter terminal.*

The services supplied from the TSOs or from DC components to the DCNO that are intended to ensure a stable and reliable operation of the DC network itself are defined as follows [3]:

AC System Services to the DC Grid *are services provided to the DC Network Operator (DCNO) from the interconnected AC Transmission System Operators (TSOs) to maintain the integrity and stability of the DC transmission network.*

DC Equipment services to the DC grid *are services provided to the DC Network Operator from interconnected DC components to maintain the integrity and stability of the DC transmission network.*

A classification of DC Grid ancillary services has been made based on the classification of ancillary services in [16] and is illustrated in Figure 5. The three main categories are frequency support, AC voltage support and system restoration. The classification of system services supplied to the DC grid are shown in Figure 6. The definition of system services to the DC grid distinguished between AC system services to the DC grid and DC equipment services to the DC grid. Examples of DC grid components that are installed to enhance the stability of the grid might be a DC storage to maintain the voltage, a DC-DC chopper solution to dissipate excess energy that cannot be transmitted by the converters, or a reactor to limit fault currents. It should be mentioned that the definitions of ancillary services and system services are flexible and might involve additional features beyond the applied definitions in this work, depending on the configuration of the DC grid itself.

The following sections go into detail about the three categories of DC grid ancillary services. The ENTSO-E draft network code on high voltage direct current connections and DC-connected power park modules has been used to discuss the

[2]Definition proposed in this thesis.
[3]Definitions proposed in this thesis.

various demands for the HVDC grid related to the categories of ancillary services shown in Figure 5. The HVDC draft network code can be found in [17]. In short, it establishes common rules for HVDC systems and sets up a common framework for network connection agreements between network operators and HVDC system owners.

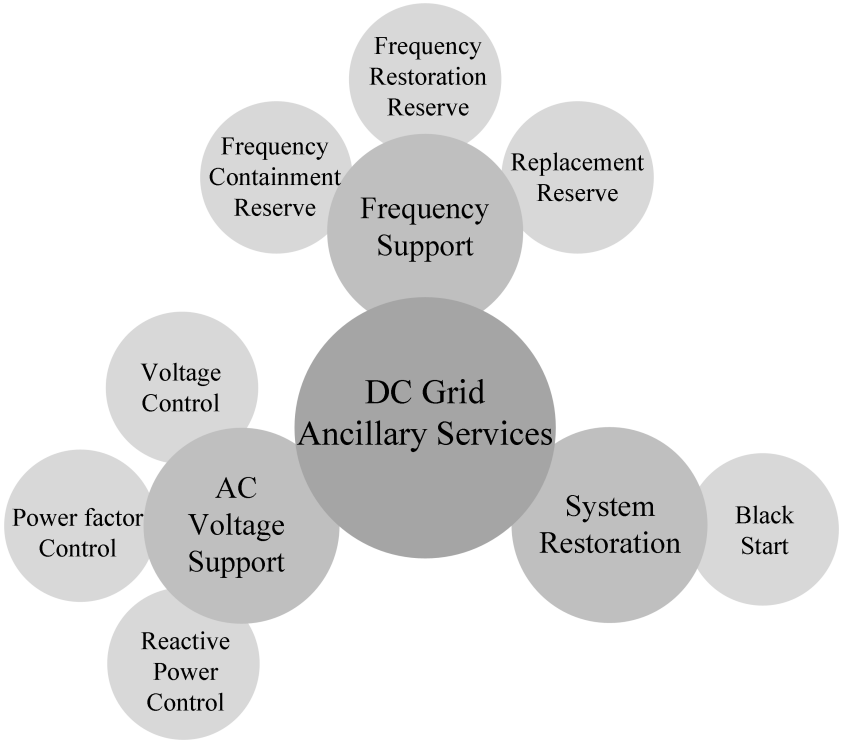

Figure 5: Overview of DC Grid Ancillary Services using ENTSO-E terminology [18].

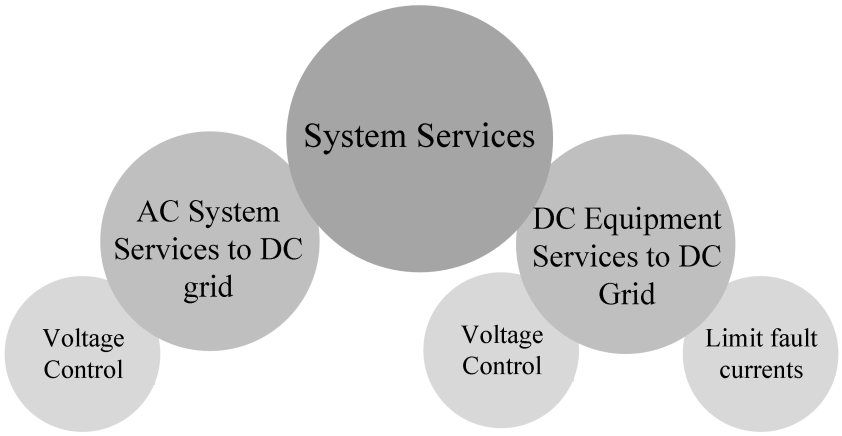

Figure 6: Overview of DC Grid System Services.

2.3.1 Frequency support

When the AC grid frequency deviates from its nominal value, it is due to a real-time difference between power generation and load in the system. The potential value of frequency support from a DC grids is therefore dependent on its ability to contribute with active power during imbalances in the interconnected AC grids. The following sections use the ENTSO-E definitions and terminology associated with resources that supply balancing services [16, 18, 19].

Frequency support is normally divided into three subsequent actions in time. The first measure after the occurrence of an imbalance, is to get the frequency under control and stabilize it. The operational reserves dedicated for this purpose are called Frequency Containment Reserves (FCRs). These are also called "primary reserves". After stabilizing the frequency, the next step is to restore it to its nominal value. The reserves activated for this purpose are called Frequency Restoration Reserves (FRRs). These are also called "secondary reserves". The FCRs and FRRs can be activated fast, but may not be capable of operating for more than a short period of time. After the frequency has been contained and restored to its nominal value, some of the FCRs and FRRs must be replaced with other reserves. The reserves used to replace the shorter-lasting reserves are called Replacement Reserves (RR) and their activation time can be in the range from several minutes to hours. Another term used for such reserves are "tertiary reserves".

The time constants associated with an HVDC grid are normally smaller than the time constants associated with an AC system. This is illustrated in Figure 7. On the occurrence of a power imbalance in a DC grid, the DC voltage will fall or rise similar to the frequency in an AC grid. When DC voltage decreases, the capacitances in the DC grid will immediately release some of their stored energy. The time constant associated with this capacitive response is smaller than that of the inertial response in an AC grid. Following a drop in voltage, the voltage controllers will stabilize the system at a new operation point. This corresponds to primary response in AC grids, but typically has a shorter activation time. After stabilizing the DC voltage, power reserves will be activated in order to restore it to its nominal value. This is equivalent to secondary response in AC grids. In order to restore the DC voltage, a DCNO is dependent on power reserves from interconnected AC grids. The restoration time is therefore dependent on the activation time of power reserves in the AC grids. As a final remark, the draft network code on HVDC-connections [17] suggests that the relevant TSO can if needed require an inertial response from the HVDC system, with associated performance parameters defined by the TSO.

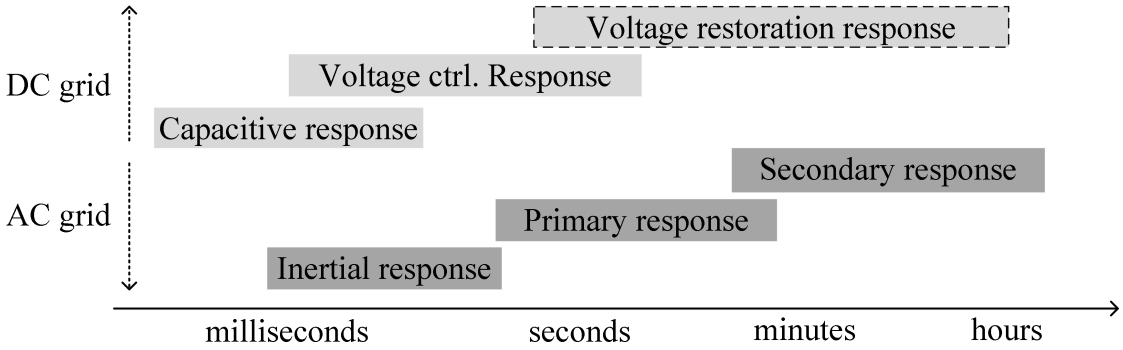

Figure 7: Comparison of time constants associated with DC and AC grid response after occurrence of a power imbalance. Voltage restoration time is dashed since the restoration time is dependent on activation of power reserves in interconnected AC grids.

2.3.2 AC voltage support

In a HVDC network, the interconnected TSO should have the right to specify voltages at the point of connection. In terms of voltage stability, the potential of the DC network to provide voltage support is dependent on the HVDC converter's ability to control the reactive power at its AC terminals, since the DC grid itself is not capable of providing reactive power compensation. Another solution might be to utilize additional compensation equipment to provide the necessary reactive power.

As shown in Figure 5, there are three reactive power control modes in which the HVDC converter station should be capable of operating in. In voltage control mode, each HVDC converter station should be able to provide voltage support within a predefined range of voltages associated with a voltage set-point that can be modified. This should be done in accordance with the HVDC converter's capabilities. For the purpose of Reactive Power Control, the converter should be able to provide a certain percentage of its maximum reactive power capability. In Power factor Control, the HVDC converter station should be able to control the power factor at the connection point within a specified range defined by the relevant TSO [17].

2.3.3 System restoration

The requirements for power system restoration concerns the black-start capability of the HVDC system. For a conventional generating unit, black-start capability is the ability to go from a shut-down condition to an operating condition and start delivering power without assistance from the electric system [20]. Extending this definition to the HVDC system means that black-start capability from HVDC

systems is the ability to energize interconnected AC-substations from shut down, without any external energy supply. The system is restored when the HVDC network is synchronized within the frequency and voltage limits defined by the relevant TSO.

3. Exchange of Frequency Containment Reserves through HVDC grids

In an AC system, the frequency reflects balance between power supply and demand. However, whenever there is an imbalance in load and generation, the frequency will change. For instance, the frequency will drop whenever there is a shortage of generation, and the frequency will increase whenever there is excess of energy. Hence, the frequency indicates the state of the system, making it an important control parameter in AC systems. Thus, keeping the frequency stable and close to its nominal value is a requirement for transmission systems to operate correctly and ensure stability in the power system.

As mentioned in Section 2.3.1, FCRs is a collective term used for power reserves that can be activated to contain system frequency after the occurrence of an imbalance. Within the category of FCRs there are two types of responses, namely inertial response and primary frequency response. These correspond to inertial reserves and primary reserves shown in Figure 8. The difference between them is that the inertial reserves can restrain the change in frequency during the first part of the transient trajectory, whereas the primary reserves can limit the stationary frequency deviation from its nominal value. The inertial reserves are expected to be activated close to instantaneously after a disturbance but they are short lasting, limited by the moment of inertia of the rotational parts of the machine. The primary frequency reserves should be activated within 30 seconds and may last for minutes [18].

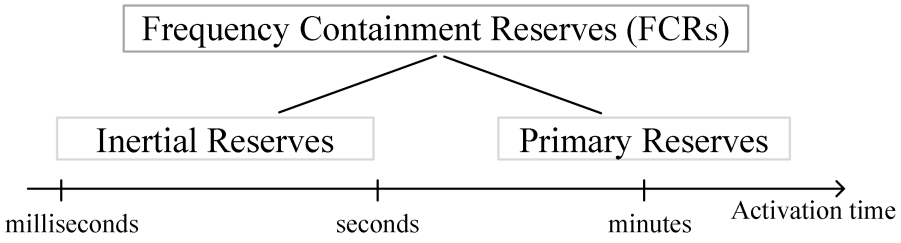

Figure 8: Classification of FCRs and associated activation times.

3.1 Inertial reserves

Inertia is defined as the resistance of an physical object to change in its state of motion. Considering a power system composed of multiple AC machines, the total inertia is defined as the systems collective ability to limit the rate of change of system frequency during an imbalance in power generation and load. The inertia is closely related to the mass of the rotating machines. A heavy machine has a larger inertia than a light one. Thus, the heavier machine has a higher ability to resist changes in its rotational speed. This is expressed in the swing equation, seen in its general form in Equation 3.1 [21]:

$$2H_{tot}\frac{df_s}{dt} = P_{production} - P_{losses} - P_{load} \tag{3.1}$$

Where H_{tot} is the inertia constant, and represents the total system inertia, given in seconds. f_s is the system frequency in per unit. $P_{prodction}$ is the total power production, P_{losses} is the total active power losses and P_{load} is the total load in the system, expressed in per unit. It can be seen that H_{tot} is inversely proportional to the frequency derivative. Hence, for a given change in load ΔP_{load}, during the first seconds, when the power production $P_{production}$ and system losses P_{losses} are constant, the rate of change of frequency is only limited by the inertia of the system, see Equation 3.2.

$$\frac{df_s}{dt} = \frac{1}{2H_{tot}}\Delta P_{load} \tag{3.2}$$

Figure 9 shows a typical frequency response in an AC system following a large imbalance in load. As mentioned, the inertial reserves can restrain the change in frequency during the first part of the transient frequency trajectory. In Figure 9, this corresponds to the initial rate-of-change-of-frequency (ROCOF) and the frequency low-point (Nadir). By extracting kinetic energy from its rotational parts, a machine can limit the ROCOF which will indirectly lead to an improvement in the nadir since it gives other reserves more time to activate. When a generator absorbs or releases kinetic energy to counteract changes in frequency it is said to have an inertial response.

Without a sufficient amount of inertia in a power system, the system frequency will be sensitive towards load imbalances. With an increasing penetration of power electronics (PE) in power systems, the total inertia in the system goes down. This is because the PE separates the AC sides of the interconnected components through a DC-link. The DC-link makes changes in frequency on one AC side invisible to the other. Hence, the inertia of one AC side is not automatically inherited by the other AC side. Since the inertial response is important to contain the frequency, current research is directed towards finding methods to emulate inertial response

between AC systems that are connected through PE interfaces by implementing additional control schemes.

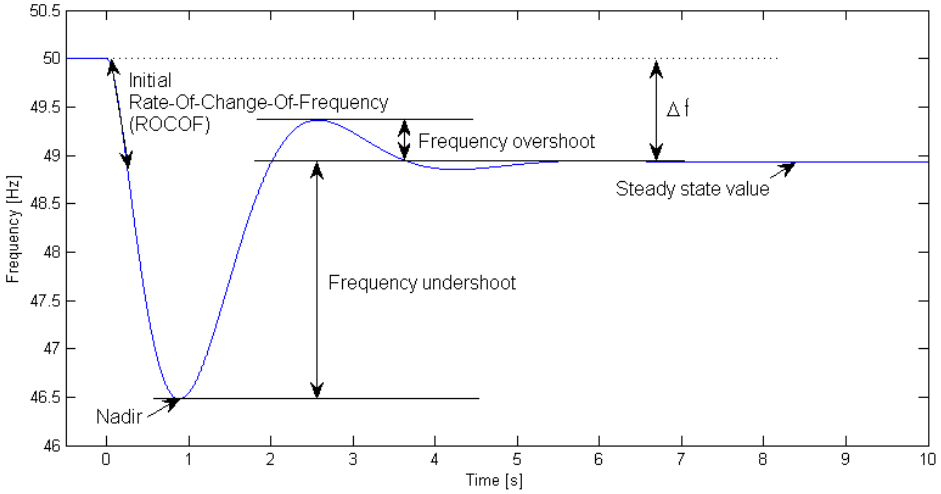

Figure 9: A typical frequency response following a significant power deficit.

3.2 Inertial response from variable speed wind turbines

As mentioned in the previous section, the initial frequency response following an imbalance in power production and power consumption is dominated by the inertial response of the on-line generation. In an AC grid, synchronous machines inherently contributes with some of their stored kinetic energy to the grid whenever there is a change in frequency. By implementing special controls, a similar performance can also be achieved with wind power plants.

Figure 10 shows a principal sketch of the variable speed wind turbine and its generator. When the electrical torque T_e is greater than the mechanical torque T_m from the wind, the rotation of the generator decreases and stored kinetic energy is extracted from the rotating mass. Variable speed wind turbines can operate in a wide range of speeds, and are controlled to maximize the power production. To facilitate this, each turbine is coupled to the wind farm internal grid through a PE interface, see the AC-AC converter in Figure 10. This allows the turbine to change its power output almost instantly. In steady state, the power delivered to the grid is determined by the available wind energy, but for a transient moment in time, the power can be controlled by using or storing kinetic energy in the mechanical

system of the turbine. Nevertheless, the AC-AC converter creates an electrical decoupling of the wind turbine and the grid which means that the wind turbine and thus the wind plant as a whole, does not inherently participate in regulation of grid frequency. However, modern wind plants have the ability to control active power output in response to grid frequency in ways that may benefit the overall grid performance [22].

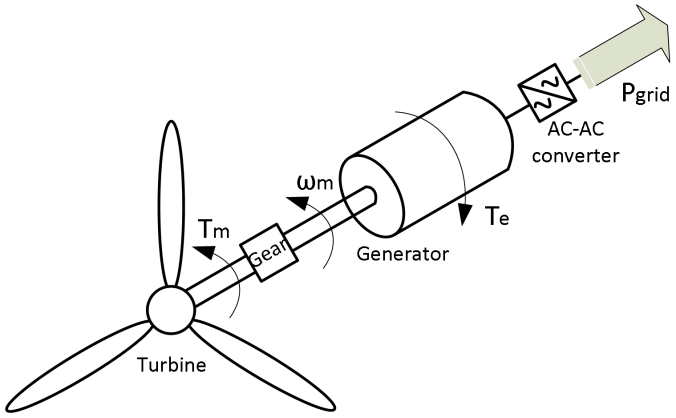

Figure 10: Electromechanical interactions in a wind turbine.

The amount kinetic energy that can be extracted from a wind turbine is a trade-off between grid codes, determined by the system TSO, and maximum mechanical stress on the components, which is determined by the turbine manufacturer. Without considering any constraints, the relation between energy, power and rotational speed is illustrated in Figure 11. This is based on a turbine with a cut-in speed of 4 m/s, rated speed of 12 m/s and a cut-out speed of 25 m/s is used. Disregarding electrical losses, the mechanical power that can be extracted from the turbine is given by 3.1.

$$P_{mech} = \frac{1}{2} C_p(\lambda, \beta) \rho A v^3 \tag{3.1}$$

Where C_p is the coefficient of power, ρ is the air density, A is the area swept by the rotor blades, and v is the wind speed. The power coefficient is a function of the pitch angle β and tip speed ratio λ. According to Betz law, the theoretical maximum power that can be extracted from a certain multitude of wind is 59.3 %. By adjusting the tip speed ratio and pitch angle, variable speed wind turbines seek to operate as close to this limit as possible. For more details on wind turbine aerodynamics see [23]. The tip speed ratio is the ratio between the speed of the tip of the rotor blade and the wind speed, see Equation 3.2.

$$\lambda = \frac{\omega_{mech} r}{v} \tag{3.2}$$

Where ω_{mech} is the mechanical speed of the turbine and r is the radius of the rotor. For a given tip speed ratio λ_{opt}, the mechanical speed of the wind turbine as a function of the wind speed is given by Equation 3.3.

$$w_{mech} = \frac{\lambda_{opt} v}{r} \tag{3.3}$$

The kinetic energy stored in the rotating parts of the turbine, $E_{turbine}$ is determined by the mechanical speed of the turbine and its mass. Equation 3.4 expresses the rotational energy stored in a turbine with a given moment of inertia, J, as a function of w_{mech}.

$$E_{turbine} = \frac{1}{2} J \omega_{mech}^2 \tag{3.4}$$

The allowed rotational speed reduction of a wind turbine for the purpose of releasing kinetic energy is determined by the turbine manufacturer. For a given reduction in speed $\Delta\omega_{mech}$ the maximum energy that is possible to extract is given by Equation 3.5 [24].

$$\Delta E_{turbine} = \frac{1}{2} J(\omega_{mech}^2 - (\omega_{mech} - \Delta\omega_{mech})^2) \tag{3.5}$$

For a speed reduction of 10 %, this relation is illustrated in bottom plot in Figure 11. It can be seen that for this turbine, and a maximum reduction of speed $\Delta\omega_{mech} = 10\%$, the maximum possible energy that can be extracted from the turbine is approximately 19 %.

3.3 Exchange of inertial reserves between HVDC connected AC systems

In the future it is expected that the use of HVDC for bulk power transmission purposes will increase. HVDC transmission is favourable to HVAC transmission when the transmission distance is above 600 kilometres for overhead lines, and 50-100 kilometres for cables [25]. When large power systems are linked together, or when remote power resources are connected to a power system, the chance is that HVDC technology will be utilized. One example of a large project featuring a multi-terminal HVDC grid is the planned North Sea offshore grid, which is part of an even larger project called the "European Super-grid" [3]. Other examples of use of HVDC are typically for connecting one power system to another, such as the "Skagerrak" and "Nordned" projects are connecting Norway to Denmark and the Netherlands, respectively [26]. These are large scale projects in terms of power, which means that the HVDC connection will have a large stability impact on the system it is connected to.

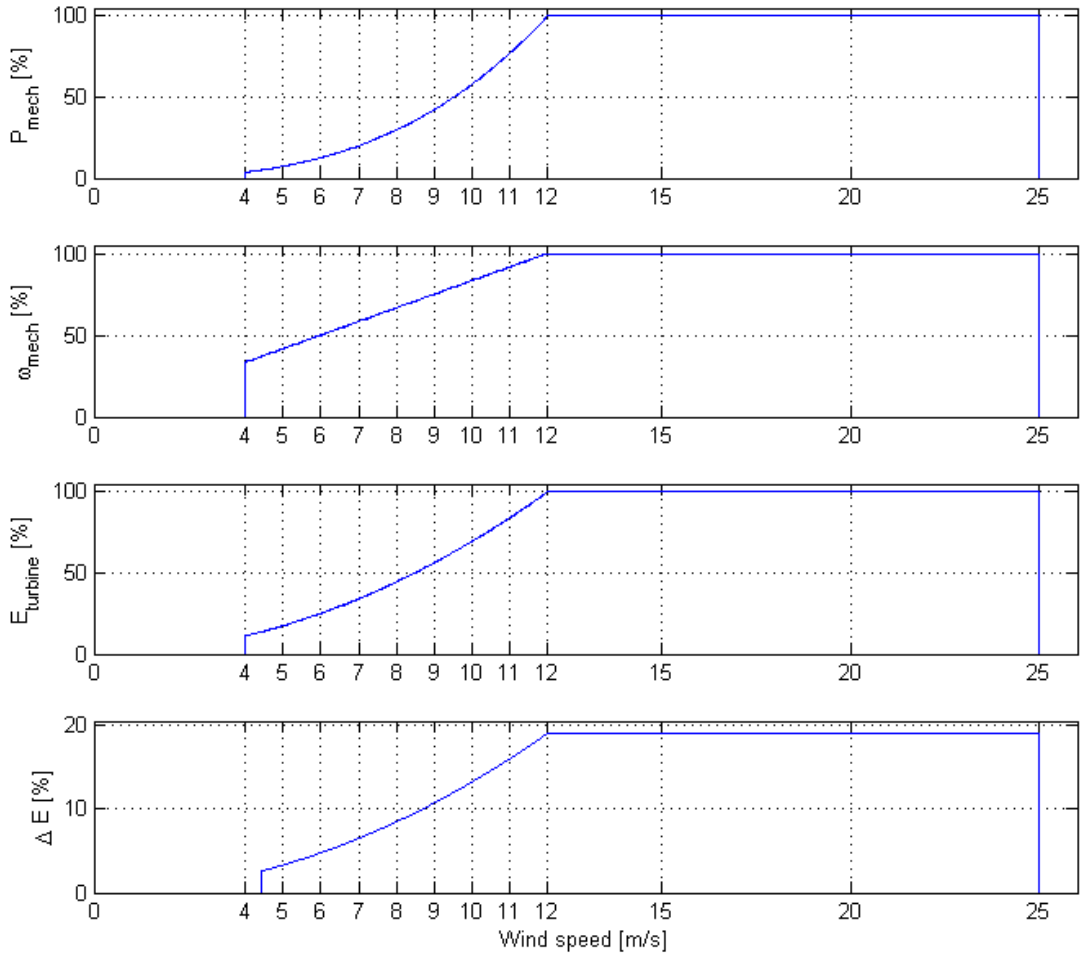

Figure 11: From top to bottom: Mechanical power from wind as a function of wind speed, wind turbine rotational speed as a function of wind speed, kinetic energy stored in the mechanical system of the turbine as a function of wind speed, and the available energy that can be drawn from the mechanical system of the turbine for a 10 percent change in the rotational speed of the turbine as a function of wind speed.

VSC-HVDC terminals do not automatically react with inertial response to disturbances in frequency in the AC grid it is connected to. This characteristic must be implemented through control systems. It is, however, not sufficient that one HVDC terminal is implemented with controls that makes it respond to the frequency event in the AC grid it is connected to. The power deficit or power surplus following an imbalance in load must be supplied from one or several of the other interconnected HVDC terminals. This means that a coordinated control system between all the interconnected HVDC terminals is required in order to success-

fully exchange inertial reserves between them. Inertial reserves must be activated based on local measurements, preferably in the range of 0 to 1 seconds. It is essential that this is performed without using communication links because of large distances between the terminals which may lead to significant time delays from sending to receiving signals. Additionally, communication systems may decrease the reliability of the system as they may be subject to down-time.

When designing the controls without using communication systems, it is useful to define energy balance indicators in the different subsystems. For instance, in AC grids, the frequency reflects the balance between power supply and demand. AC grids contain rotating masses with the ability to store or release energy and the amount of stored energy is proportional to the frequency squared, see Equation 3.1 expressed in per unit. In DC grids the voltage is proposed to be an energy balance indicator. Similarly to rotating masses in an AC grid, a DC grid contains capacitances with the same ability to store or release energy. The amount of stored energy is proportional to the voltage squared V_{DC}^2, see Equation 3.2. C is the total capacitance in the DC network. It is suggested that each converter control system relates the energy balance indicators on each sides of the converter.

$$E_{rot} = H_{tot} f_s^2 \tag{3.1}$$

$$E_{cap} = \frac{1}{2} C V_{DC}^2 \tag{3.2}$$

Figure 12 shows an example of a multi-terminal HVDC grid composed of one AC grid, grid A, and an offshore wind farm. As seen in Figure 3, this is similar to the system that is studied in the later chapters in this thesis. The example is used to illustrate how energy balance indicators can be utilized to exchange inertial reserves between the HVDC connected AC systems. In order to exchange inertial reserves from the wind farm to the AC grid denoted "grid A", inertial response controls are implemented in the converter connected to grid A, VSC_A, and the wind farm connected converter, VSC_{WIND}. In the event of a step in load in grid A the following subsequent sequences in time are executed:

1. The frequency f_A drops as a consequence of power imbalance.

2. Converter VSC_A senses change in frequency in grid A, and its control system immediately reduces the DC-voltage V_{DC}.

3. Converter VSC_{WIND} senses change in DC-voltage, and its control system immediately reduces the frequency f_WIND.

4. Frequency converters in all wind turbines sense the change in f_WIND, and immediately supply stored kinetic energy from the rotor blades. This kinetic

energy will reach Grid A shortly after, and compensate for the frequency drop.

Inertial response in wind turbines has been available as a commercial solution for a few years. One example is the inertia technology from General Electrics: GE WindInertia^{TM}[27] which is based on local frequency measurements. Such turbine controls should be coordinated with the VSC-HVDC control in order to emulate an inertial response between HVDC terminals. In Chapter 5 a control strategy for achieving exchange of inertial reserves between two AC terminals similar to the system discussed in this section is presented and explained in detail.

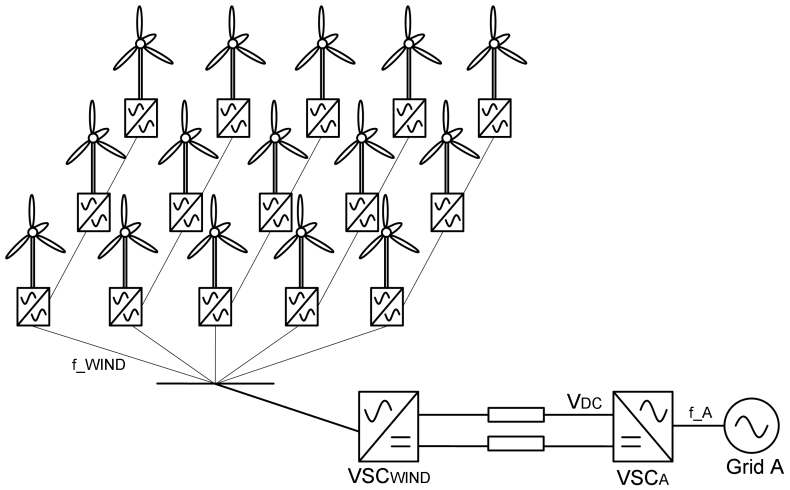

Figure 12: An example of a two-terminal HVDC grid composed interconnecting an AC grid and an offshore wind power plant.

4. Modelling and Control of VSC

The VSC can be modelled with various degrees of detail; including semiconductor components, or by using a time-averaged approach. When it is modelled in detail, semiconductor switching operation is represented. This approach provides the accurate dynamic behaviour of the converter in detail, and may be preferred when investigating harmonics and fast transients in voltage and current. However, it increases the model's complexity, which in turn makes simulations complex and time-consuming. The following sections go into detail about modelling in the dq-reference frame and control theory used as a basis for the control system. The notation is the same as in [28]. A small overview of this is given below:

Convention of symbols:

- variables that are functions of time v i
- space vectors $\vec{v}(t)$ $\vec{i}(t)$

Subscripts:

- AC phases a, b, c
- d-axis d
- q-axis q
- AC source s
- AC side of converter c

Superscripts:
Superscripts indicate the parameter's reference for defining a space vector

- three phase frame, referred to phase a A
- the stationary $\alpha\beta$-frame α
- the rotating dq-reference frame d

Figure 13 shows a detailed model of a two-level VSC. Figure 14 shows how to model the two-level VSC by using an average approach. This is achieved by considering each converter terminal as a controllable voltage source (v_c) connected

to an AC transmission network (v_s). The AC transmission network is modelled by means of its thevenin equivalent, i.e. the voltage sources are connected through a series reactor (L) and resistance (R). Since the average model will not capture harmonics or fast transients, it will not distinguish between different types of VSCs, i.e. two-level and multilevel. Nevertheless, since this report does not aim to study harmonics originated from power electronic switching or fast transients in voltage and current, the average approach is used to model the VSCs in the simulation model. The approach is similar to the one used in [25].

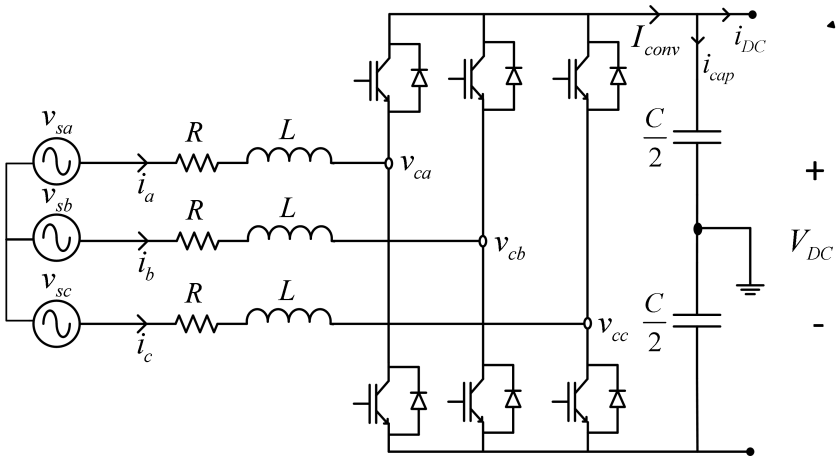

Figure 13: Detail VSC model.

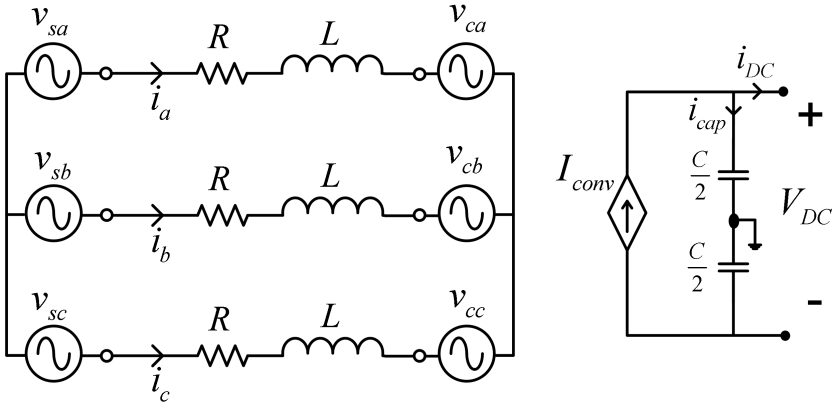

Figure 14: Average VSC model.

4.1 Parks transformation and the dq-reference frame

The dq-reference frame allows us to represent time-varying currents and voltages as constant DC-quantities. This is achieved by synchronising the d- and q- axis with the grid voltage. The detection of phase angle and frequency is done by equipping the model with a phase lock loop (PLL). There are especially two advantages with using the dq-reference frame in control strategy:

- DC-quantities are easier to control.
- The d and q axis are perpendicular to each other which makes it possible to achieve a decoupling of the d and q axis and control the quantities independent of each other.

In this work, voltage invariant Park transformations and inverse Park transformations have been used. Note that the d-axis is assumed to lag the q-axis by 90°. When voltage invariant transformation is chosen, the transition matrix is multiplied with $\frac{2}{3}$ and the amplitude of the phase voltages in the dq- and abc-frame will be equal. The voltage invariant Parks transformation and the inverse transformation are included in Equation 4.1 and Equation 4.2 respectively [28].

$$\begin{bmatrix} v_d \\ v_q \\ v_0 \end{bmatrix} = \frac{2}{3} \cdot \begin{bmatrix} \cos(\theta) & \cos(\theta - \frac{2\pi}{3}) & \cos(\theta - \frac{4\pi}{3}) \\ -\sin(\theta) & -\sin(\theta - \frac{2\pi}{3}) & -\sin(\theta - \frac{4\pi}{3}) \\ \frac{1}{2} & \frac{1}{2} & \frac{1}{2} \end{bmatrix} \cdot \begin{bmatrix} v_a \\ v_b \\ v_c \end{bmatrix} \tag{4.1}$$

$$\begin{bmatrix} v_a \\ v_b \\ v_c \end{bmatrix} ul = \frac{2}{3} \cdot \begin{bmatrix} \cos(\theta) & -\sin(\theta) & 1 \\ \cos(\theta - \frac{4\pi}{3}) & -\sin(\theta + \frac{4\pi}{3}) & 1 \\ \cos(\theta + \frac{2\pi}{3}) & -\sin(\theta + \frac{2\pi}{3}) & 1 \end{bmatrix} \cdot \begin{bmatrix} v_d \\ v_q \\ v_0 \end{bmatrix} \tag{4.2}$$

Where $\theta = \omega t$ is the voltage phase angle. The parameter v_0 is the zero sequence voltage which is zero under normal, balanced conditions, i.e. $v_0 = 0$. The above transformation and inverse transformation is also valid for currents.

4.2 Converter modelling in the dq-reference frame

The average model of the VSC shown in Figure 14 can also be expressed mathematically by Equation 4.1:

$$v_s(t) - v_c(t) = R \cdot i(t) + L\frac{\mathrm{d}}{\mathrm{d}t}i(t) \tag{4.1}$$

In [28] a dynamic analysis of induction machines in terms of dq-windings is performed. The method for modelling the VSC in terms of dq-windings is identical. This section renders parts of the procedure in [28], regarding the relation between phase variables and dq-variables with the aim of expressing the average model mathematically in the dq-reference frame.

Before the dq-winding voltages can be expressed, it is common to introduce the orthogonal $\alpha\beta$-axes. These are defined such that α is aligned with phase A, see Figure 15 which illustrated this. Space vectors allows us to express any parameter in the three phase frame in the $\alpha\beta$-frame by Equation 4.2:

$$\vec{v}^{\,\alpha}(t) = v_a(t)\mathrm{e}^{-jwt} + v_b(t)\mathrm{e}^{-j(wt-120^\circ)} + v_c(t)\mathrm{e}^{-j(wt-240^\circ)} \tag{4.2}$$

Using this relation, the expression for the average model in Equation 4.1 can be expressed in the $\alpha\beta$-frame by Equation 4.3.

$$\vec{v_{s_{\alpha\beta}}}^{\,\alpha} - \vec{v_{c_{\alpha\beta}}}^{\,\alpha} = R \cdot \vec{i_{\alpha\beta}}^{\,\alpha} + L\frac{\mathrm{d}}{\mathrm{d}t}\vec{i_{\alpha\beta}}^{\,\alpha} \tag{4.3}$$

Figure 15 also shows the rotating dq-axes. The rotational speed is ωt. It can be shown that the space vectors with respect to the α-axis is related to those with respect to the d-axis as follows

$$\vec{v}^{\,\alpha} = \vec{v}^{\,d} \cdot \mathrm{e}^{jwt} \tag{4.4}$$

By multiplying each term in Equation 4.3 with e^{jwt} the mathematical expression for the VSC in the dq-reference frame can be expressed by Equation 4.5:

$$\vec{v_s}^{\,d}\mathrm{e}^{jwt} - \vec{v_c}^{\,d}\mathrm{e}^{jwt} = R \cdot \vec{i}^{\,d}\mathrm{e}^{jwt} + L\frac{\mathrm{d}}{\mathrm{d}t}(\vec{i}^{\,d}\mathrm{e}^{jwt}) \tag{4.5}$$

or,

$$\vec{v_s}^{\,d}\mathrm{e}^{jwt} - \vec{v_c}^{\,d}\mathrm{e}^{jwt} = R \cdot \vec{i}^{\,d}\mathrm{e}^{jwt} + jwL\vec{i}^{\,d}\mathrm{e}^{jwt} + L\mathrm{e}^{jwt}\frac{\mathrm{d}}{\mathrm{d}t}(\vec{i}^{\,d}) \tag{4.6}$$

Divide by e^{jwt} gives Equation 4.7:

$$\vec{v_s}^{\,d} - \vec{v_c}^{\,d} = R \cdot \vec{i}^{\,d} + jwL \cdot \vec{i}^{\,d} + L\frac{\mathrm{d}}{\mathrm{d}t}(\vec{i}^{\,d}) \tag{4.7}$$

On matrix form and in the frequency domain the original expression for the average model of the VSC in Equation 4.1 can now be expressed in the dq-reference frame on matrix form by Equation 4.8.

$$\begin{bmatrix} v_{sd} \\ v_{sq} \end{bmatrix} - \begin{bmatrix} v_{cd} \\ v_{cq} \end{bmatrix} = R \begin{bmatrix} i_d \\ i_q \end{bmatrix} + sL \cdot \begin{bmatrix} i_d \\ i_q \end{bmatrix} - wL \begin{bmatrix} i_q \\ -i_d \end{bmatrix} \tag{4.8}$$

It should be noticed that there is a coupled interaction between the d- and q-axis found in the last term in Equation 4.8. This means that any change in the d-axis current will affect the q-axis current and vice versa. This is undesired since a completely decoupled system is required in order to have the most efficient control. Based on Equation 4.8 circuit diagrams for the AC side of the VSC in the d- and q-axis can be drawn, see Figure 16.

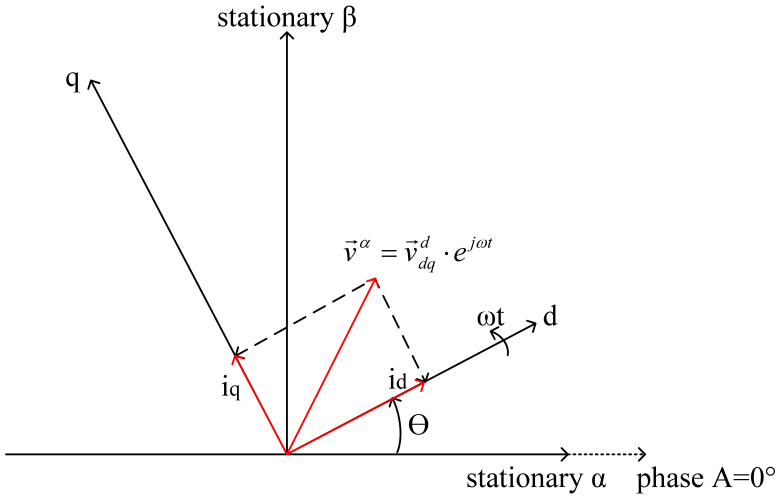

Figure 15: The relation between the stationary $\alpha\beta$- reference frame and the rotating dq-reference frame.

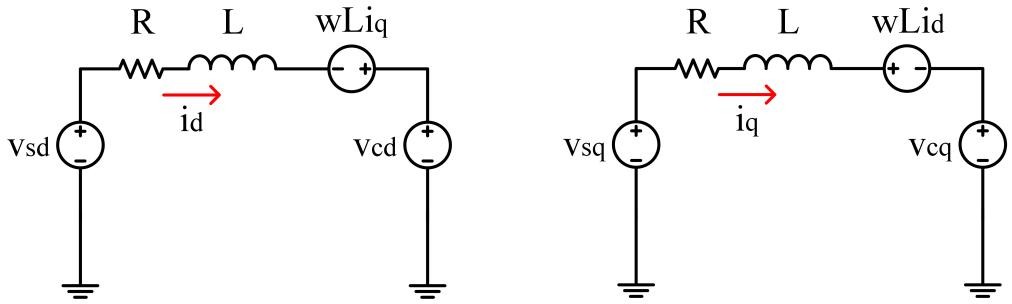

Figure 16: The AC side of the VSC modelled in the d- and q-axis.

5. Converter Control Strategies

5.1 System description

The system studied in this thesis is seen in Figure 17. As explained in Chapter 1, the main part of the work is performed on a laboratory model. Some of the main components in the laboratory model are indicated in the figure, such as the induction machine and synchronous generator. The representation of each of the components used in the laboratory set-up is described in detail in Chapter 6. Overall, the figure shows a two-terminal HVDC grid connecting a wind farm equivalent to a weak AC grid equivalent. It has been decided to put the work in the context of the ability of VSC-HVDC connected wind farms to contribute with primary frequency control services. To test this, a procedure connecting a significant load in the AC grid while examining the response from the wind farm equivalent is used. This involves implementing special controls in the VSC terminals.

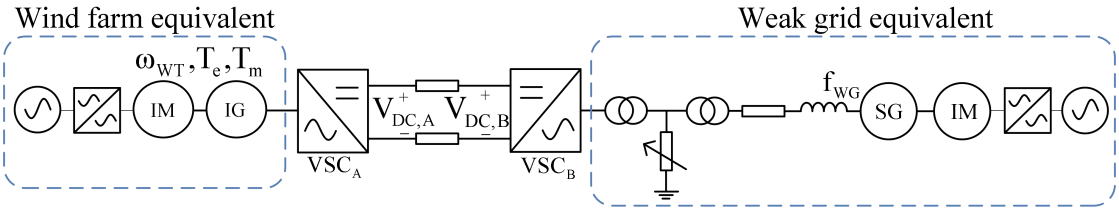

Figure 17: A two-terminal HVDC grid connecting a wind farm equivalent to a weak AC grid.

In the following sections, state-of-the-art control strategies for multi-terminal HVDC grids are presented as well as the control strategies that are implemented in the wind farm connected converter and the weak grid connected converter VSC_A and VSC_B. It can be seen that the system studied in this thesis is similar to the system shown in Figure 12, which shows a more complete model of the wind farm. The differences between a full scale wind farm and the wind farm equivalent used for the analyses in this thesis are highlighted in Section 5.4.1.

5.2 State-of-the-art control strategies for multi-terminal HVDC-grids

In a DC network it is possible to control the DC voltage based on current or power. The current based control uses a I-V characteristic to control the voltage, whereas the power based control uses a P-V characteristic. In this section, only power based state-of-the-art is considered. This is similar to what is studied in [25]. Other works related with MTDC control strategies can be found in [29, 30, 31].

Master-Slave control is an extension of the conventional point-to-point control where one terminal controls the DC-link voltage and the other terminal controls the power flow. In master-slave control one terminal is responsible for maintaining the DC-link voltage (master-node) and the other terminals are defined to be constant power nodes (slave-nodes) [25]. Graphs showing the relation between voltage and power for the master-node and slave-nodes are shown in the two top graphs in Figure 18. Although master-slave control is uncomplicated and easy to implement in a system it has some significant disadvantages. For instance, the master-node may be subjected to large strains, since it is responsible for handling all power deviations. To keep the voltage from rising or falling in situations when the system is subjected to disturbances, it is important to maintain the current balance between the terminals. The system is entirely dependent on the master-node to maintain the DC-link voltage, such that in the incident of an outage of the master-node, a voltage collapse is inevitable, and the N-1 criterion is not fulfilled. Therefore, a more sophisticated control strategy is necessary to ensure stable operating conditions in a multi-terminal DC grid.

Voltage-Margin control is a modified version of the master-slave control where the constant power and constant voltage characteristics are combined. The slave-nodes are assigned a constant power region for a given voltage range and a constant voltage for any voltage outside this range [25, 31]. The relation between voltage and power for the slave-nodes is given in the rightmost middle graph in Figure 18. It can be seen that a semi-distributed voltage control is achieved since the slave-nodes can contribute to maintain the voltage when the voltage deviation is large enough. However, in steady-state, it is still the master-node that is responsible for balancing the power. Thus, the master-node may still be subjected to large strains. Also, this approach may impose instability issues on the AC grid as the power transfer to the converter may change quickly with large increments.

Voltage-Droop control is based on the philosophy of having distributed voltage control in the MTDC system. Each terminal is assigned a linear relationship between its DC-link voltage and the power flowing through its terminals, see the middle graph to the left in Figure 18. This way, the terminals share the task of maintaining the system voltage as well as the duty of instantaneous power balancing in the power grid [25]. How large share each terminal contributes with as a balancing unit is dependent on the droop constant, which is the slope of the droop line. If the droop constant is zero the node will act as a constant-voltage node as opposed to a constant power node which will be the case if the droop constant is infinite. The droop control does not rely on fast communication between the terminals. Neither is the system dependent on one particular node, since all nodes are active in maintaining the voltage.

The DC voltage droop is similar to the frequency control in an AC power system. The DC voltage acts as an indicator for power balance the same way as frequency in an AC network. The DC-link voltage at each terminal will react to changes in power flow at that terminal. Given that all other voltages in the system are constant, if the power flow into the DC grid increases or decreases at a certain terminal, the voltage on this terminal consequently increases or decreases. The difference between the conditions for DC voltage droop and frequency droop is that opposed to the node voltages in a MTDC network, the frequency is the same throughout the entire AC system. For a cable between two points in a MTDC grid there will be a certain voltage drop due to resistance. This means that for all cases except zero power transmission, the voltage between two terminals will never be exactly the same.

Dead-band and undead-band droop control are combinations of the voltage margin and voltage droop control strategies. The principles are shown in the two bottom graphs in Figure 18. For the dead-band droop control the terminal is a constant power node for a given voltage range but for any voltage outside this range, a droop is defined. For the undead-band droop control the relation between voltage and power is always linear, but the droop constant differs for normal and disturbed operation [31].

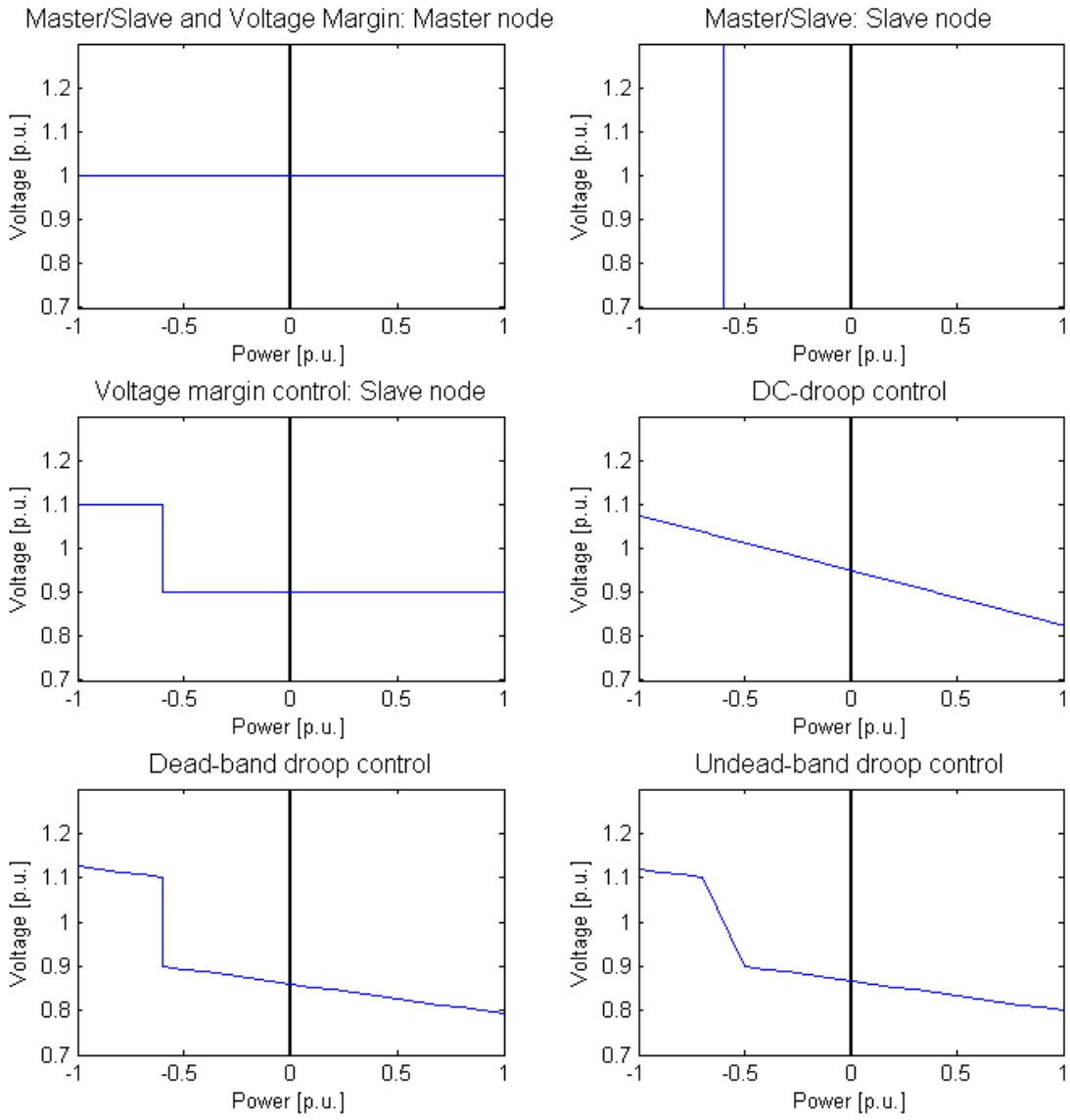

Figure 18: Power based voltage control methods in a MTDC network. Negative power means that power flows from the DC side of the converter to the AC side of the converter, i.e. the converter is in inverter mode. The figures only show the relation between voltage and power for one terminal. In a system with two or more terminals the operating point will be in the equilibrium point where power balance is achieved in the system.

5.3 Control strategy on the weak AC grid connected converter

Seeing that the system studied in this report only consists of two terminals, implementing DC droop on the converter that is connected to the AC grid may seem excessive. Since the wind farm node is implemented as a power node, meaning that it is allowed to export power restricted only by its own production, the AC grid connected converter will control the DC voltage. This means that the AC grid connected converter could be controlled as a constant voltage node instead of having DC droop. The conventional control strategy for a two terminal DC grid configuration is precisely this; to have one terminal controlling the voltage (master node) and the other terminal controlling the power (slave node). However, to keep the laboratory model flexible towards adding an extra DC terminal, it is chosen to keep the DC droop control that was developed in the specialization project [3]. It should be noted that the droop control that is implemented in this laboratory set-up acts according to a droop line consisting of only one segment. In a real system, the droop is implemented with a piecewise linear characteristic. This is to restrain the controller from acting outside the rated conditions of the system [32].

In section 3.3 the basic control procedure was explained. The control on the weak grid converter should relate AC system frequency to the DC voltage. In this thesis, this additional control that is used to create this relation is "Inertia Emulation". Its design is explained in detail in the following section.

5.3.1 Inertia emulation

Figure 19 shows the proposed inertial emulation control structure that is implemented on the AC grid connected VSC converter. The outer control loop is the DC voltage droop. To emulate an inertial response, a term that is proportional to the rate of change of frequency is added to the droop control error. If the frequency derivative is negative, for instance in case of a sudden increase in the system load, the inertia emulation control will reduce the voltage set-point in the DC droop. Reducing the voltage set-point is equivalent to vertically moving the droop line in the downwards direction. To find a new operating point, the droop will increase the power import, thus increasing the voltage, and as the frequency derivative gradually becomes less negative and eventually goes to zero, the voltage set-point rises and the droop line is moved back to its original position. This is explained in detail in Section 5.5. On the output of the inertia emulation control a dead-band is included to avoid that the controller reacts on noise from the frequency measurement. The standard cascaded control, namely the DC voltage control and current control, are explained in detail in the report of the laboratory converter control systems [33].

5.4 Control strategy on "wind farm"-connected converter

The wind farm connected converter controls the torque in the induction generator which is used to represent a wind farm. The wind farm connected converter is embedded with a control loop that allows the wind farm to react to changes in the DC voltage by releasing energy or increasing the energy that is stored in the rotational parts of the wind turbines. The intent of this action is to support the weak grid which the wind farm is connected to, by contributing with primary reserves that can help contain the AC system frequency. In this thesis, this action from the wind farm connected converter is called "voltage support". Its layout is explained in detail after highlighting some differences between the laboratory and a full-scale wind farm in the following sections.

5.4.1 Difference between the laboratory wind farm equivalent and a full scale wind farm

In the laboratory set-up, some simplifications are made regarding modelling of the wind farm. The generator that is used to represent the wind farm is directly connected to the HVDC converter. In a full-scale system the generator would be connected to the HVDC converter by means of a fully controlled frequency converter, as shown in Figure 12. In this way, it would be integrated with the HVDC grid through a converter terminal facing the DC grid in one direction, and the AC-AC converters in the individual turbines in the other direction. Since these turbine converters are not included in the wind farm equivalent in the lab, the internal grid is neglected. As a consequence, the internal control in the wind farm between the park controller and the individual turbines is also neglected. As discussed in Section 3.3, the control in the wind farm connected converter would have to relate to the frequency in the internal grid, whereas the turbine converters would be directly related to the kinetic energy stored in each turbine. As can be seen in the next section, the control implemented in the laboratory model assumes that the HVDC terminal is able to extract kinetic energy from the turbines, although in reality, it could only relate to the energy balance indicator in the internal grid. More investigation on this is proposed as further work in Chapter 9.

5.4.2 Voltage support

Figure 20 shows the suggested voltage support control strategy on the wind farm connected converter. The control responds to the change in DC voltage caused

by the inertia emulation control in the AC grid connected converter, explained in Section 5.3.1. The objective is to support the AC grid by using rotational energy stored in the wind farm equivalent. In order to propagate change in frequency in the AC grid into giving an inertia response from wind farm, a term that is proportional to changes in the DC-link voltage, is added to the torque reference, T_e^*. In steady state, the DC voltage may deviate from the nominal DC voltage, but the effect of this will be eliminated by the PI controllers in the speed control loop.

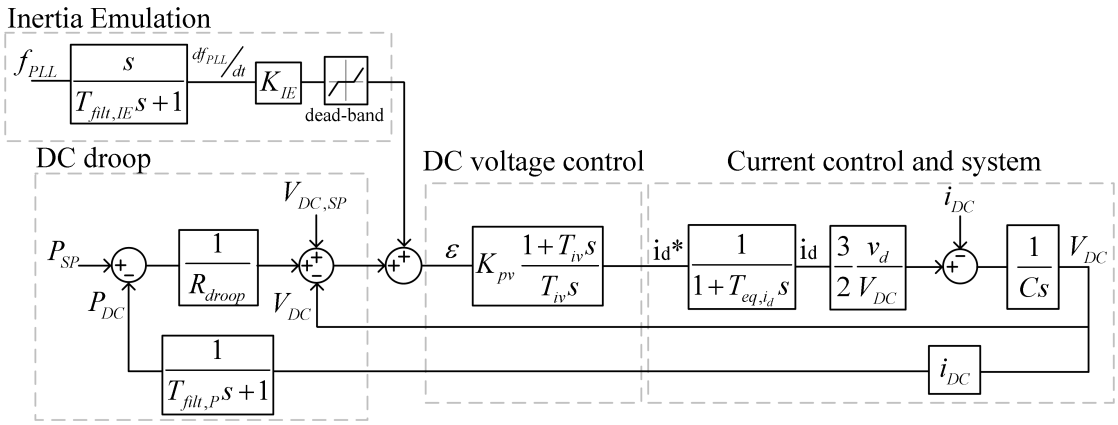

Figure 19: Block diagram showing control design in the AC grid connected VSC-HVDC converter.

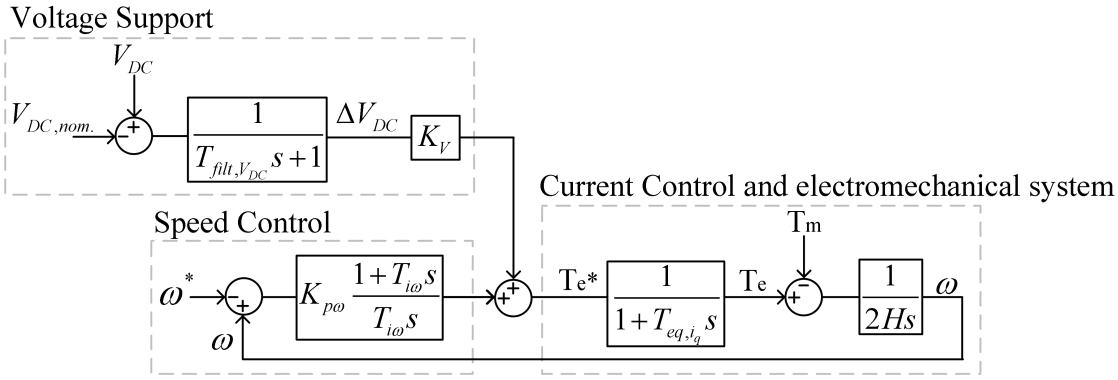

Figure 20: Block diagram showing the control design in the wind farm connected VSC-HVDC converter.

5.5 Illustration of interactions between implemented controls

This section aims to illustrate the coordinated response of the proposed control system shown in Figure 19 and Figure 20. In addition, simplified formulas are developed to get an idea of which range the inertia emulation and voltage support gains will lie in. Figure 21 supports the derivation of equations presented below. The following assumptions are laid at ground:

- The frequency in the weak grid f_{system} follows the trajectory in Figure 21. This is meant to correspond with the initial phase of a more realistic frequency response.
- The inertia emulation filter $T_{filt,IE}$ and voltage support filter $T_{filt,Vdc}$ are neglected.
- All losses are neglected.
- The response times of the DC voltage control and wind farm torque control are neglected, i.e. they respond instantaneously.
- The power extracted from the wind turbine during the event is constant.
- The speed controller in the wind turbine does not respond within the time scale under consideration.
- All units are expressed in per unit of their rated values.

The rate of change of frequency, α is defined as

$$\alpha = \frac{df_s}{dt} \tag{5.1}$$

When the control system senses a change in frequency, the inertia emulation control will immediately modify the DC voltage set point in the DC droop control with a magnitude of $\alpha \cdot K_{IE}$. As a consequence of the voltage drop, the voltage support control contributes with a change in the wind farm power output equal to ΔP_{DC}. Meanwhile, the DC droop control will counteract the change in the DC voltage with a magnitude equal to $\Delta P_{DC}/R_{droop}$, where R_{droop} is the DC droop coefficient. The resulting DC voltage drop can be expressed as

$$\Delta V_{DC} = K_{IE} \cdot \alpha - \frac{\Delta V_{DC} \cdot K_V \cdot \omega_{mech}}{R_{droop}} \tag{5.2}$$

Which can be solved for ΔV_{DC}

$$\Delta V_{DC} = \frac{K_{IE} \cdot \alpha}{1 + \frac{K_V \cdot \omega_{mech}}{R_{droop}}} \tag{5.3}$$

The change in power ΔP_{DC} can be expressed as follows

$$\Delta P_{DC} = \Delta V_{DC} \cdot K_V \cdot \omega_{mech} \tag{5.4}$$

Substituting for ΔV_{DC} yields

$$\Delta P_{DC} = \frac{K_{IE} \cdot K_V \cdot \omega_{mech} \cdot \rho \cdot \alpha}{R_{droop} + K_V \cdot \omega_{mech}} \tag{5.5}$$

The voltage support gain can be expressed by Equation 3.5 and Equation 5.4

$$\Delta E = \Delta P_{DC} \cdot \Delta t = K_V \Delta V_{DC} w_{mech} \Delta t \tag{5.6}$$

By substituting for ΔE and rearranging the voltage support gain can be expressed as follows

$$K_V = \frac{\frac{1}{2} J(\omega_{mech,0}^2 - (\omega_{mech,0} - \Delta\omega_{mech})^2)}{\omega_{mech} \Delta V_{DC} \Delta t} \tag{5.7}$$

Based on Equation 5.3, the inertia emulation gain can be estimated as

$$K_{IE} = \frac{\Delta V_{DC}}{\alpha}(1 + \frac{K_V \omega_{mech}}{R_{droop}}) \tag{5.8}$$

To illustrate the utility of the formulas, an example is made based on the experimental set-up. The allowable changes in DC voltage and wind turbine speed are the main constraints. In this case, they are chosen according to Table 2.

Table 2: Example of values of parameters.

Parameters	**Value [SI]**	**Value [pu]**
α	5 Hz/s	0.1 pu
ΔV_{DC}	10 V	0.016 pu
$\omega_{mech,0}$	600 rpm	0.6 pu
$\Delta\omega_{mech}$	40 rpm	0.04 pu
Δt	0.5 s	0.5 s
ρ	-	6.67 %
J	-	3 s

This give the following gains

$$K_V = 14.5 \tag{5.9}$$

$$K_{IE} = 0.246 \tag{5.10}$$

This is used as starting point for practical tuning procedure performed in Section 8.1. It is remarked that this is close to the values obtained by trial-and-error tuning in Chapter 8.

Figure 22 shows the DC droop dynamics during the change in frequency in the weak grid. The points a-e indicate the operation points of the converter during different sequences in time, and correspond to those shown the second illustration in Figure 21. When the frequency in the weak grid decreases, the DC voltage set-point will drop leading to a vertical shift of the droop line. This corresponds to the change in operating point from a to b. Since the DC droop will counteract the immediate change in DC voltage, the control will respond by increasing the power import which results in a new operating point, c. The total change in DC voltage is ΔV_{DC}. When the AC grid frequency stabilizes, the frequency derivative becomes zero, and the droop-line set-point goes back to its original value (point c to d). The droop control will counteract the sudden increase in DC voltage by reducing the power import, leading to operating point e.

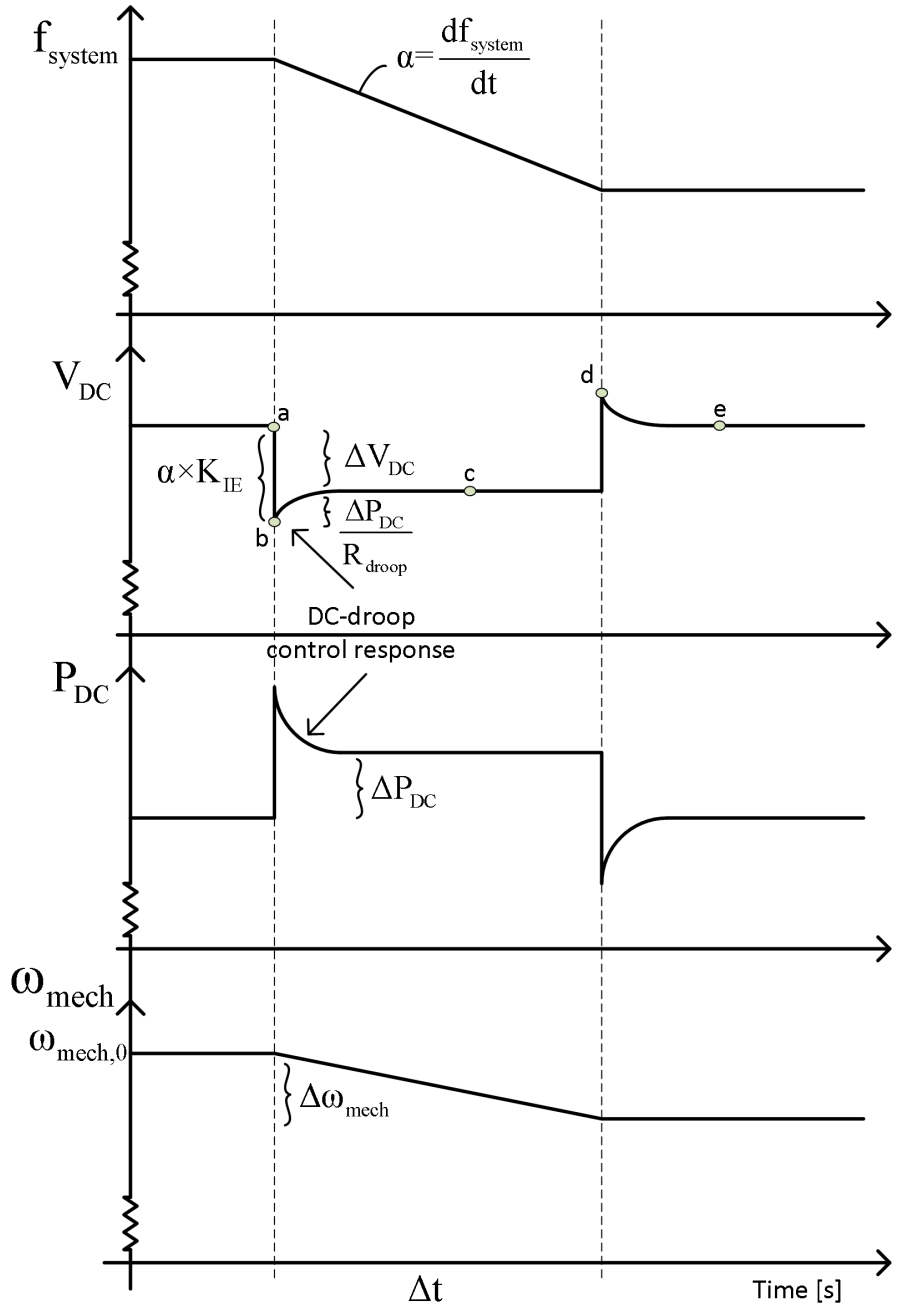

Figure 21: Illustration of inertia support controls during a simplified frequency transient.

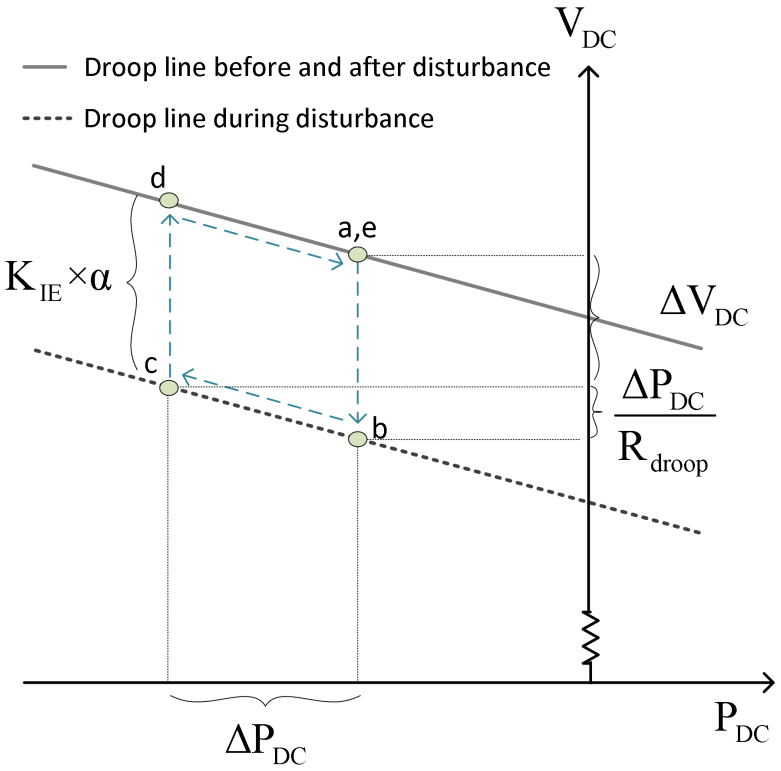

Figure 22: The droop line during change in frequency in the weak grid with implemented control loop for inertial response.

6. The Laboratory Set-up

This section describes the laboratory model of the scaled two-terminal HVDC system shown in Figure 23. The model has been implemented in the SINTEF/NTNU Renewable Energy Systems Laboratory [34] and consists of the components listed below:

- A wind farm equivalent
  - A 55 kVA motor-generator set
  - Motor-drive for the 55 kVA motor
- A DC grid
  - Two 60 kVA Voltage Source Converters (VSC)
  - A Resistor network
- A weak grid equivalent
  - A transmission line equivalent including a transformer
  - A 17 kVA synchronous generator-induction motor set
  - A 22 kW frequency converter for controlling induction motor driving the 17 kVA synchronous generator
  - A controllable resistor load
- A remote control program in Labview

The induction motor-generator set is used as wind farm equivalent and the motor drive is used to emulate wind power input. The converters separate the wind farm and weak grid equivalent through a DC cable. The resistor network is used to model the DC cable. The synchronous generator-induction motor set is used to represent a stand alone AC grid, called a weak grid. The weak grid also contains a transmission line equivalent including a transformer and a controllable resistor bank.

The converters and the motor-drive are equipped with an interface which enables receiving status messages and measurements and sending control actions. This is a so-called CAN-bus interface. The control is achieved by using the Labview programming environment. This will be further discussed in the following sections together with detailed descriptions of the components that compose the laboratory model.

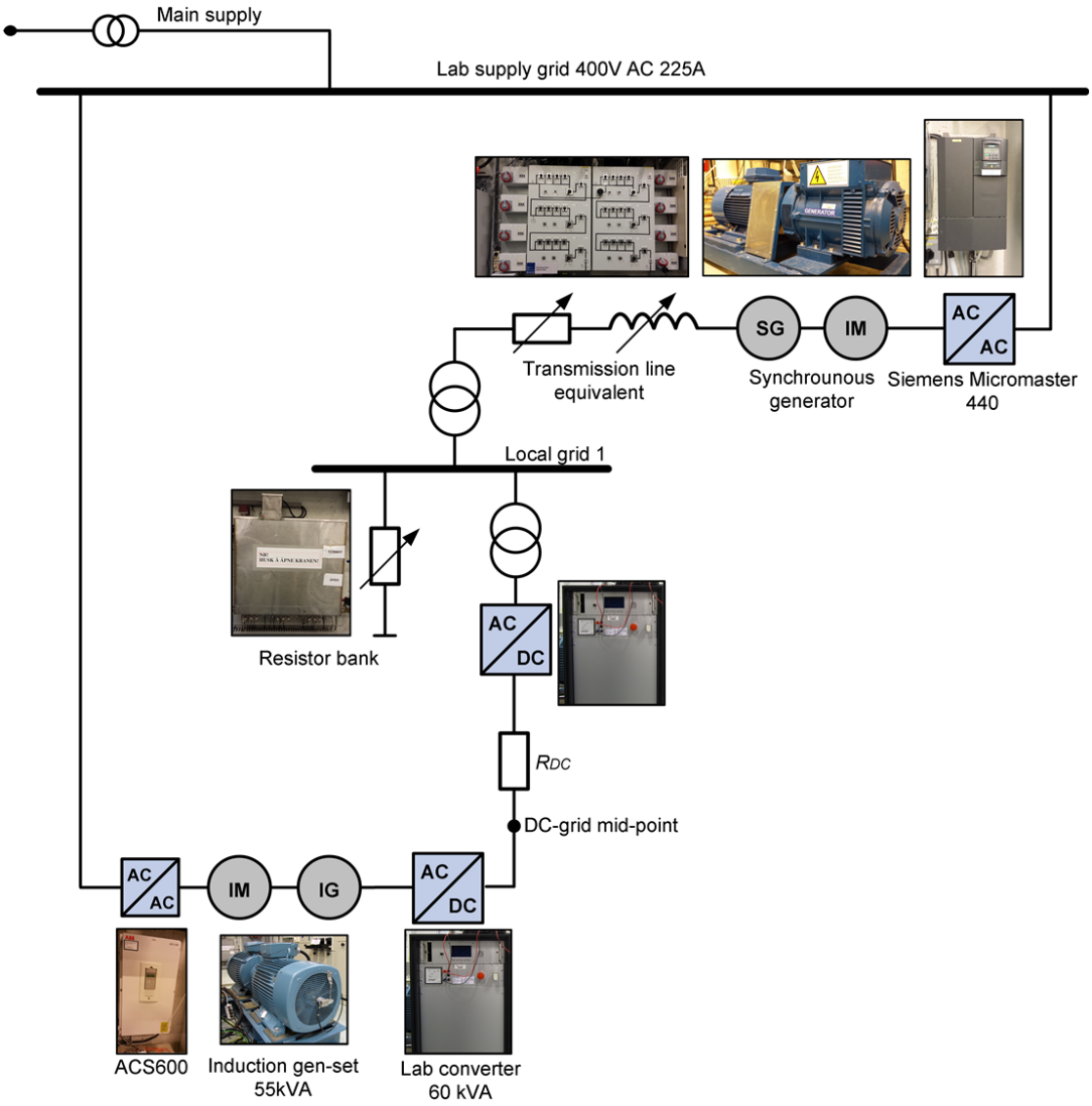

Figure 23: A single line diagram of the laboratory model studied in this work. This part of the SINTEF/NTNU Renewable Energy Systems Laboratory [34].

6.1 Description of the wind farm equivalent

The wind farm equivalent consists of a frequency converter used to emulate wind and an induction motor-generator set used to represent the wind farm. Pictures of these components are shown in Figure 24 and Figure 25.

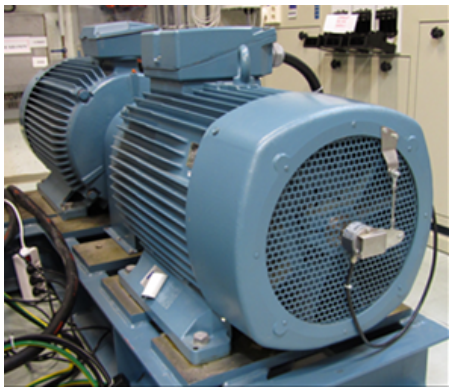

Figure 24: The 55 kVA induction machine set.

Figure 25: The ABB frequency converter used to emulate wind.

6.1.1 The induction motor-generator set

The induction motor-generator is a standard squirrel cage induction machine set. Table 3 gives the induction generator data [35].

Table 3: Induction generator rated values.

Parameter	**Value**
Power rating	55 kVA
Voltage	380 V
Power factor	0.81^o
Nominal speed	990 rpm

6.1.2 The wind emulator

The drive used to control the motor of the induction motor-generator set is an ABB ACS 600 unit. Its main specifications are shown in Table 4. The drive can be controlled and monitored remotely with Labview through a National Instrument DAQ-unit. It can be turned on/off, and the torque-reference can be dynamically changed. In addition, speed and torque measurements can be logged. See Section 6.4 for a description on how the wind emulator is implemented in the Labview environment.

Table 4: ABB ACS600 rated values.

Parameter	**Value**
Rated power	75 kW
Input voltage	400 V AC

6.2 Description of the DC grid

The DC grid contains two VSCs and a variable resistor network to emulate the DC cables. A picture of one of the VSCs and a picture of the resistor cabinet are shown in Figure 27 and Figure 26, respectively.

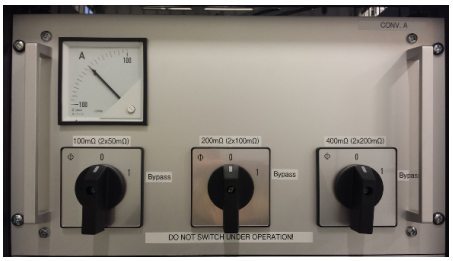

Figure 26: Variable resistor cabinet to emulate DC cable.

Figure 27: One of the VSC converters.

6.2.1 Description of the VSC

The data for the converters used in this experiment can be found in Table 5. The data are retrieved from [36].

Table 5: Laboratory converter data [36].

Parameter	Value
Main supply voltage	0-400 V RMS (AC)
DC voltage	550-750 V
Rated Power	60 kVA
Rated current	100 A RMS (AC)
Switching frequency	maximum 7 kHz
LCL filter	500 μH 50 μF 200 μH
DC filter capacitance	14 mF

The control system for the 60 kVA laboratory converters is developed by SINTEF and is documented in [33]. It runs on a Xilinx Virtex5 FPGA-based processor system. Time critical parts are implemented as FPGA blocks while the rest is implemented as processor software routines.

The control system is configured with a wide range of parameter settings and possible operation modes. It can act either as a motor-drive or as a grid-connected converter controller. Depending on the application, different control objectives can be chosen, e.g. DC-voltage, active/reactive current, frequency (grid-connected mode), torque, speed, flux (motor-drive mode). Details on the implementation can be found in Appendix 10.8.

6.2.2 Description of the DC line model

The DC line model uses resistances to emulate the DC cable, meaning that the capacitance and inductance of the cable are neglected. This is because of limitations in available equipment. The model consists of three resistor units that are series connected and coupled in parallel with a set of switches that makes it possible to bypass any one of them, see Figure 28 [37]. The resistor network makes it possible to obtain resistances in the range of 0-350 $m\Omega$.

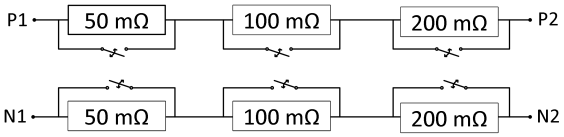

Figure 28: Resistive DC line model [37].

6.3 Description of the weak grid equivalent

The weak grid equivalent is made up of a transformer, a transmission line equivalent, an induction motor and a synchronous generator set and a frequency converter. These are shown in Figure 29-Figure 32. In addition, a controllable resistor bank is available and can be connected/discontented automatically.

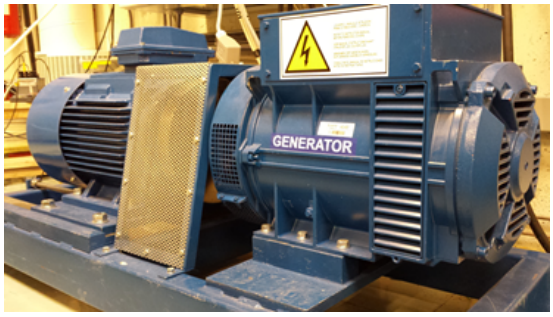

Figure 29: The induction motor-synchronous generator set.

Figure 30: The frequency converter controlling the induction motor.

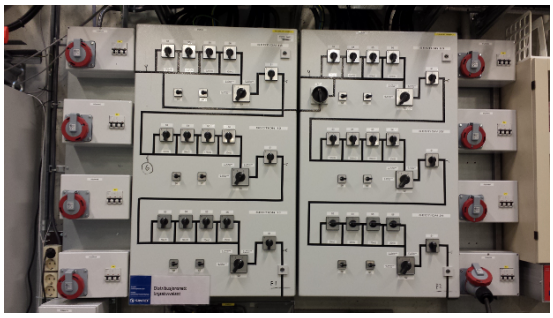

Figure 31: The transmission line equivalent.

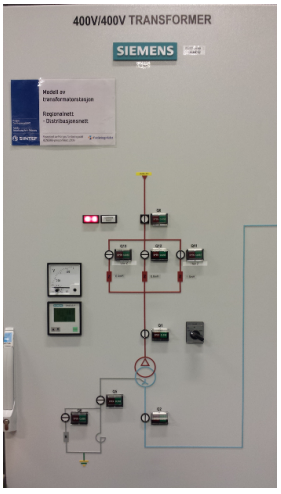

Figure 32: 400 V/400 V Transformer.

6.3.1 The induction motor-synchronous generator set

The synchronous generator referred to throughout this report is connected to the frequency controlled induction motor. The synchronous generator represents conventional generation in the AC grid. Excitation and governor is similar to an full-scale power plant. Table 6 gives an overview of synchronous generator ratings whereas Table 7 contains information about the induction motor driving the synchronous generator.

Table 6: Synchronous generator data [38].

Parameter	**Value**
Rated power	17 kVA
Rated voltage	400 V
Rated power factor	0.8
Rated speed	1500 rpm
Inertia	0.109 kgm^2 kVA

Table 7: Induction motor data [38]

Parameter	**Value**
Rated power	18.5 kVA
Rated voltage	380-414 V
Rated power factor	0.86
Rated speed	1465 rpm

6.3.2 The frequency converter

The frequency converter in the weak AC grid equivalent is used to control the induction motor. It has a rating of 22 kVA and an encoder is used to measure the motor speed. For details see [39]. The block diagram of the vector control with encoder, as well as droop control and governor settings are included in Appendix 10.4.

6.3.3 The transmission line equivalent

The laboratory is equipped with a transmission line equivalent. Line impedance and resistance can be configured through a control panel, see Figure 31. In order to make the impact of transmission losses as small as possible, the lowest setting for R and L were chosen in all measurements. This corresponds to $Z_{tot} = 88 + j120m\Omega$. For more information, see [40].

6.3.4 The transformer

A 400:400 V transformer is placed between the transmission line equivalent and the bus bar "Local grid 1" in Figure 23. A picture from the lab can be seen in Figure 32. The series impedance can be selected as "low" or "medium". To limit the impact from the voltage drop, "medium" impedance is selected. For further information about the transformer, see [41].

6.3.5 The resistor bank

The resistor bank can be changed in steps of 1 kW from 1 to 31 kW. This can be done either manually or via an interface such as Labview.

Figure 33: The controllable resistor bank.

6.4 Labview

As part of the specialization project, a Labview program was developed. This program can communicate with the converters through the CAN-bus, discussed in Section 6.2.1. The purpose of the program is to control the DC voltage and power flowing on the converter terminals according to a droop line [3]. In this thesis this program has been further modified to include controls proposed in Chapter 5. Since inertial support should be provided within seconds, the control system requires even faster communication with the converters than in the last version of the Labview program.

An illustration of the procedure in the Labview program is shown in Figure 34. There are two main loops in the Labview program. One is used to calculate the frequency derivative in the weak grid with a sampling time of 1 millisecond. Since the frequency derivative is one of the most important inputs in the control system,

it should be measured as often as possible. The other main loop contains the control loops and calculates the DC voltage and torque reference and sends these to the FPGA converter control cards on the weak grid and wind equivalent connected converters, respectively. The program is also capable of turning on/off the contactors and drivers of both converters. Finally, it is possible to read measurement signals from each converter. The most important converter measurements are the DC-voltages, the induction generator speed, and the DC-power. Due to the time-delay associated with CAN-bus communication and program execution, the sampling time of this loop is presently limited to 25 milliseconds. Screen-shots of the Labview block diagram and front panel are included in Appendix 10.7 and Appendix 10.6, respectively.

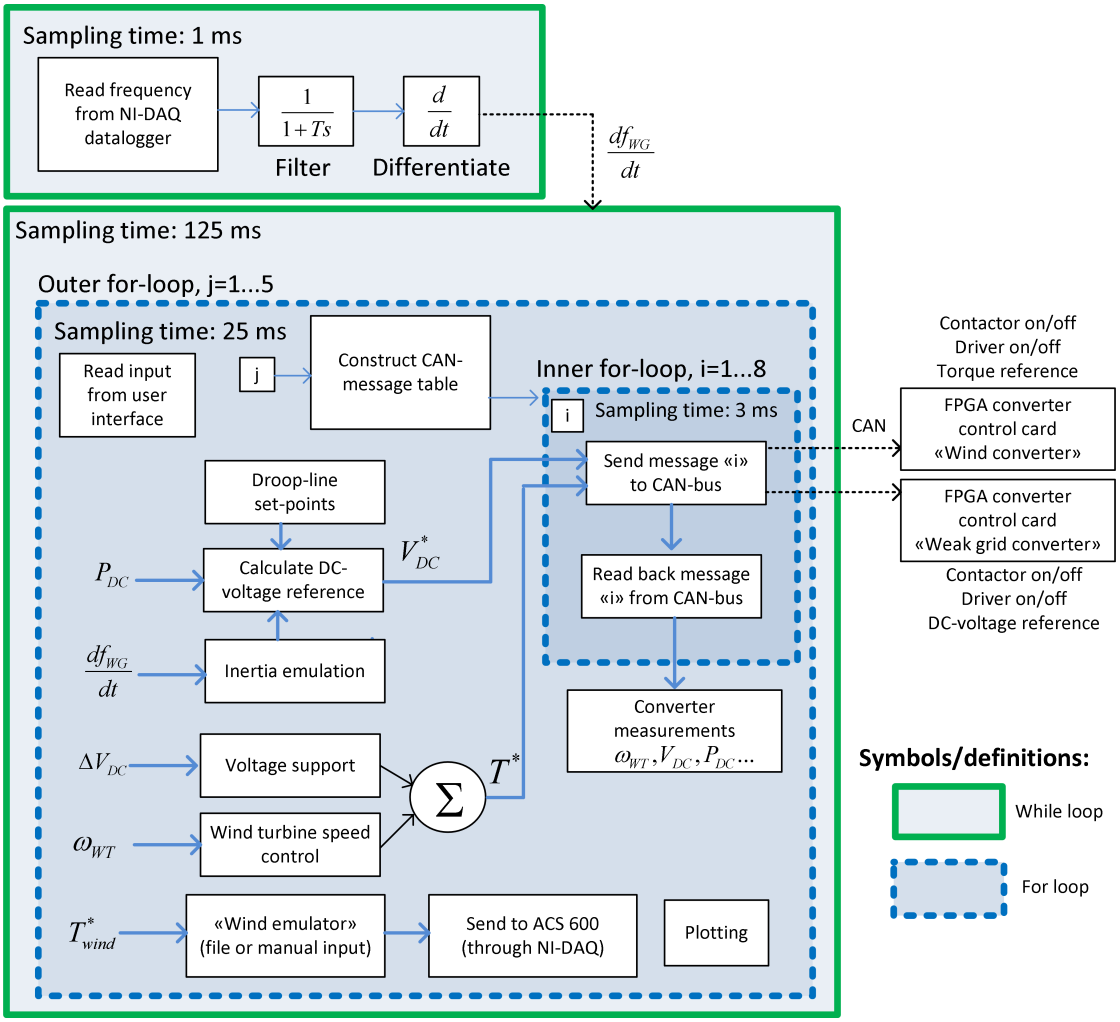

Figure 34: A flowchart of the Labview program

7. Simulink Modelling and Validation

Figure 35 shows the Simulink model of the laboratory set-up. The upper part of the model represents the weak grid equivalent implemented with the inertia emulation control explained in Section 5.3.1. The middle part of the model is the DC voltage control with DC droop, and the lowest part of the model represents the wind farm equivalent implemented with the voltage support control, explained in Section 5.4.2. Block colors are used to distinguish between controls and the physical system. The blocks that are light blue are control blocks or filters implemented in Labview. Grey blocks are converter control blocks and yellow blocks represent the physical system. The parts of the physical system that are modelled are the capacitance of the DC network, the inertia of the weak AC grid equivalent and the inertia of the wind farm equivalent. The light blue blocks with pictures of a step shaped response, represent the sampling time associated with the Labview control program.

It can be seen that the model only consists of Simulink blocks. Therefore, the it cannot be used to perform electric circuit simulations. Nevertheless, it is able to recreate important dynamics seen in measurements from the laboratory set-up. The simulation model was built with the purpose of investigating possible reasons for power oscillations that were observed in the laboratory set-up. In addition, it will be used for evaluating the effect of varying key parameters, such as filter time constants.

In general, this chapter goes into detail on how each part of the laboratory system is represented in the simulation model. Also, the following sections describe how the simulation model is validated through comparisons with measurements from the laboratory model. Further, some of the challenges with the system are discussed along with some assumptions made in the simulation model. A list of the parameters used in the model, and their respective values, is given in the next section.

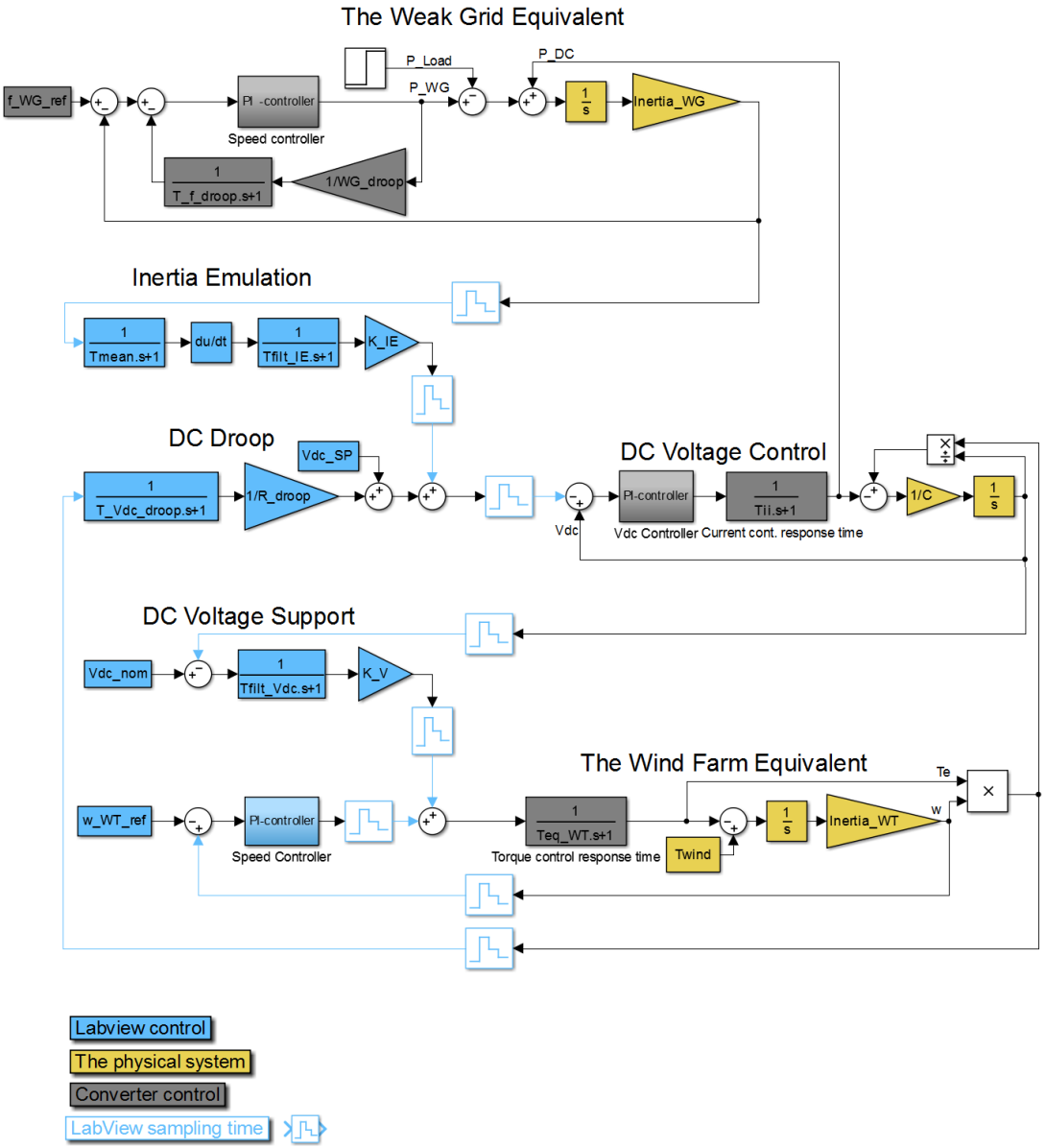

Figure 35: Simulink model of the laboratory set-up.

7.1 List of parameters

An explanation of the different parameters used to model the laboratory set up is given in Table 8. The complete model can be seen in Figure 35.

Table 8: Explanation of the parameters and their values used to model the system in Simulink. FTC = Filter Time Constant.

Ratings and parameters	**Symbol**	**Value**
Nominal Power		20 kW
Nominal AC voltage		400 V (L-L, rms)
Nominal DC voltage	$V_{dc,nom}$	630 V
Nominal Wt speed	$w_{WT,ref}$	1000 rpm
Weak grid inertia	H_{WG}	0.5 s
Wind farm equivalent inertia	H_{WT}	1.5 s
Frequency set-point WG	$f_{WG,ref}$	50 Hz
AC frequency droop FTC	$T_{f,droop}$	150 ms
Frequency droop coefficient in WG	WG_{droop}	9.93 p.u.
Inertia constant of WG	Inertia_{WG}	1.18 s^{-1}
AC frequency FTC	T_{mean}	200 ms
Frequency derivative FTC	$T_{filt,IE}$	100 ms
Inertia emulation gain	K_{IE}	-
DC voltage set-point	$V_{DC,SP}$	1 pu
Active power FTC in DC droop	$T_{Vdc,droop}$	25 ms
DC droop coefficient	R_{droop}	15 (6.67 %)
Converter current control time constant	T_{ii}	1.5 ms
Total DC network capacitance	C	56 mF (1.1 s)
DC voltage support FTC	$T_{filt,Vdc}$	100 ms
Voltage support gain	K_V	-
Converter torque control time constant	$T_{eq,WT}$	2 ms
Mechanical torque	T_{wind}	-
Inertia constant of WT	Inertia_{WT}	0.33 s^{-1}

7.2 The weak grid equivalent (WG)

Figure 36 shows the set up used for validating the simulation model of the weak grid. The AC frequency f_{WG} is compared with the reference frequency in the synchronous generator governor $f_{WG,ref}$. In a real system, it would be necessary to use the converter's PLL frequency as input in the inertia emulation control, since measurements must be taken locally. In the lab converters, however, the resolution of the frequency measurement from the PLL is 0.1 Hz, which is too low to achieve a precise calculation of the frequency derivative in the AC grid. For this reason, and because the scope of this work is not on making an optimal PLL, it is chosen to use a "raw-signal" frequency measurement from the synchronous generator as input in the inertia emulation control. See Section 7.6 for further discussion on this.

The speed controller operates according to a frequency droop modelled with the filter time constant $T_{f,droop}$ which is the same as in the laboratory model, and the droop gain WG_{droop}, which was found through data fitting according to the steady state value of the frequency following a load imbalance. The power produced is compared to the load in the system, and any imbalance is reflected in a change in frequency according to the total inertia of the system. The inertia of the system is expressed by the inertia constant, H_{WG}. As discussed in Section 3.1, the inertia constant is inversely proportional to the change in frequency. In the model the term containing the inertia constant is called $Inertia_{WG}$.

A comparison of the laboratory and simulation model response in the frequency f_{WG} for different steps in the system load, P_{Load}, was performed, see Figure 42. It can be seen that the frequency response from the simulation model matches the frequency response from the lab for all the different steps in load.

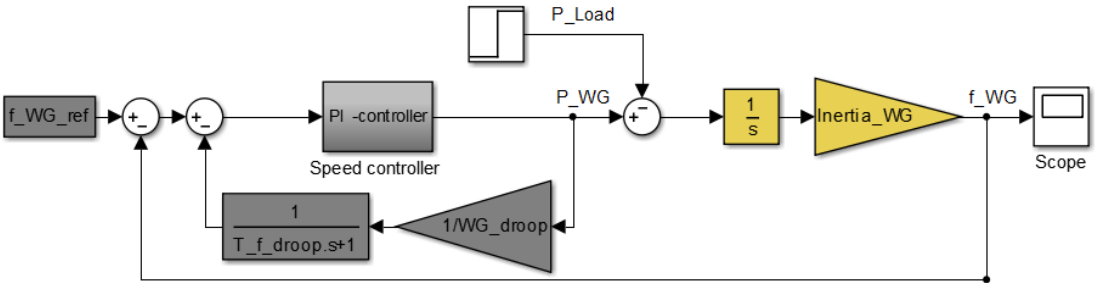

Figure 36: Simulink model of the Weak Grid (WG)

7.3 The wind farm equivalent (WT)

7.3.1 The inner torque control

The torque control is modelled as a first order response with time constant $T_{eq,WT}$ which is estimated based on the control parameters, see Figure 37. The sampling time of the Labview program is included since the torque reference is sent from the Labview control loop. The inertia of the induction motor-generator set that is used to model the wind farm, $Inertia_{WT}$, was found from the laboratory measurements of the resulting speed when a step in the torque reference was applied. Figure 37 shows the set up used for tuning the torque control. For different steps in the torque reference $T_{e,step}$ the resulting wind turbine speed is measured. The speed will increase linearly and the slope of the curve will be proportional to the inertia of the machine, as well as the step in torque reference. During the tuning the wind torque T_{wind} is set to zero.

The outer speed control is left out during tuning of the torque control. A comparison of the speed response of the simulated wind farm equivalent and the laboratory model is shown in Figure 43. Since there is no speed control, for any given torque, the speed of the turbine will increase. It can be seen that the simulation model is able to recreate the response to a great extent. Some deviations are visible, and especially the simulations do not match the laboratory results for the highest and lowest step in torque. Nevertheless, the simulation model is considered acceptable. It should be noted that during this experiment the sampling time of the speed of the laboratory model was slow. Hence, the graph showing the laboratory results are less smooth than the results from the simulation model.

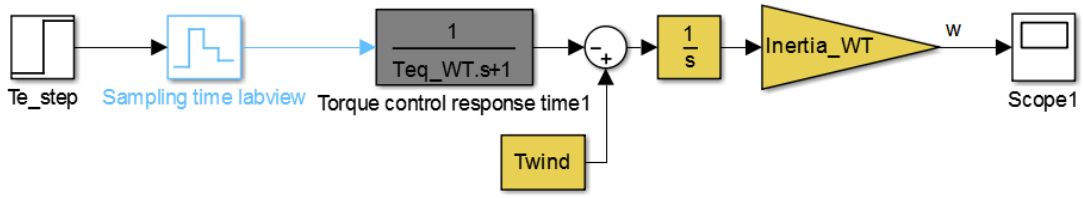

Figure 37: Validation of torque control in wind turbine equivalent with step in torque reference and measurement of turbine speed. During the validation the wind torque T_{wind} was zero.

7.3.2 The outer speed control

As explained in Section 6.4, the WT speed control is embedded in Labview. The Labview sampling time is therefore included on the speed controller output, as well as on the input where measured WT speed is compared to the speed reference $\omega_{WT,ref}$. For different steps in speed reference, the speed response is measured and compared with measurements from the laboratory model, see Figure 38. The results are shown in Figure 44. It can be be seen that the speed response from the model in Simulink is somewhat slower than the one from the laboratory model, but that the steady state value is the same for all cases.

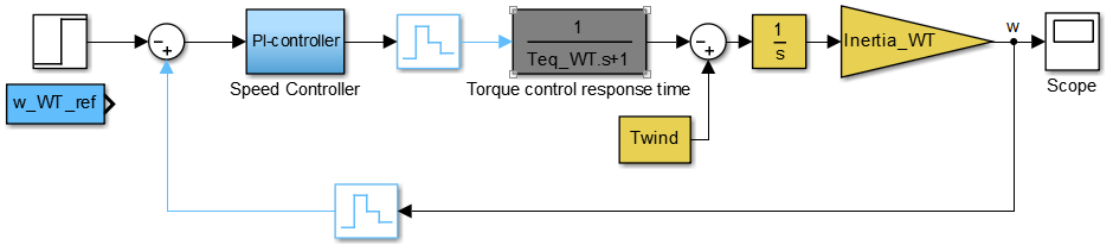

Figure 38: The block diagram of the WT speed control. During the validation the wind torque T_{wind} was zero.

7.4 LabView control blocks

The Labview control blocks are the inertia emulation control in the converter connected to the weak grid equivalent, and the voltage support control in the converter connected to the wind farm equivalent. Since these blocks are Labview-implemented controls, validation with the laboratory model should strictly not be necessary. In theory the control blocks should behave equally whether they are implemented in Labview or in Simulink. However, the inertia emulation control contains a block that measures the frequency in the weak grid. Measuring the frequency in a real system is challenging, and care must be taken to ensure that the measurement is correct. Therefore, in the following sections, comparisons of the responses from Labview control blocks and the corresponding Simulink control blocks are made.

7.4.1 Inertia emulation

Figure 39 shows how the inertia emulation discussed in 5.3.1 is implemented in Simulink. The filter time constant $T_{filt,IE}$ is the same as the filter time constant used in the Labview control, and T_{mean} is found through data fitting since parts of the control system in the synchronous generator in the lab is unknown. During the validation of the model the inertia gain K_{IE} was equal to 1.0. Figure 45 shows a comparison of the frequency derivative in the weak grid for different steps in load in the simulations and the laboratory model. It can be seen that the match is good.

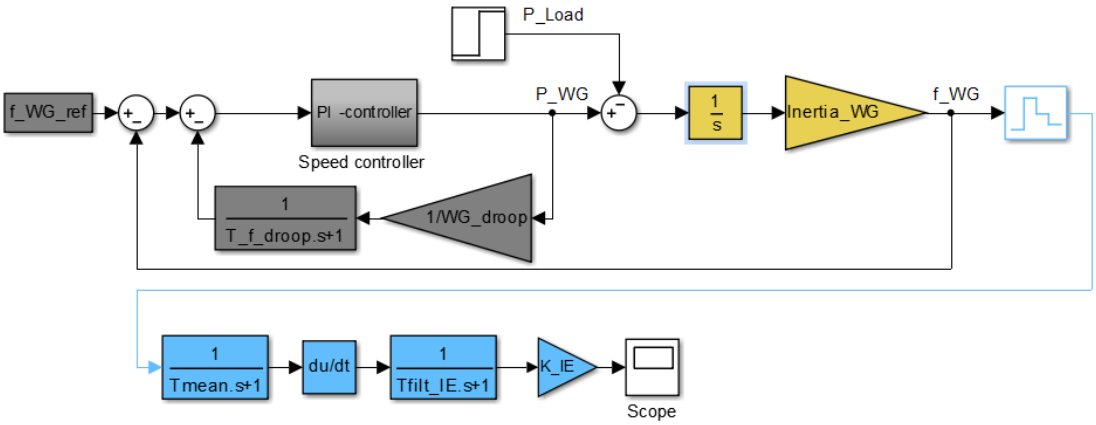

Figure 39: The Simulink model of the weak grid with inertia emulation control.

7.4.2 Voltage support

Figure 40 shows how the responding voltage support discussed in 5.4.2 is implemented in Simulink. In the WT connected converter the measured DC voltage is compared to the nominal DC voltage $V_{dc,nom}$. The filter time constant $T_{filt,Vdc}$ is the same as the filter time constant in Labview. The voltage support gain K_V amplifies the changes is DC voltage and acts on the WT torque control reference. K_V was set equal to one during the validation of the model. A test was performed with only the weak grid converter connected. The voltage droop and the inertia term in the weak grid were both disabled. A step in the voltage set-point was applied and the voltage response was measured. Figure 46 shows a comparison of the response in the simulation model and the laboratory set-up.

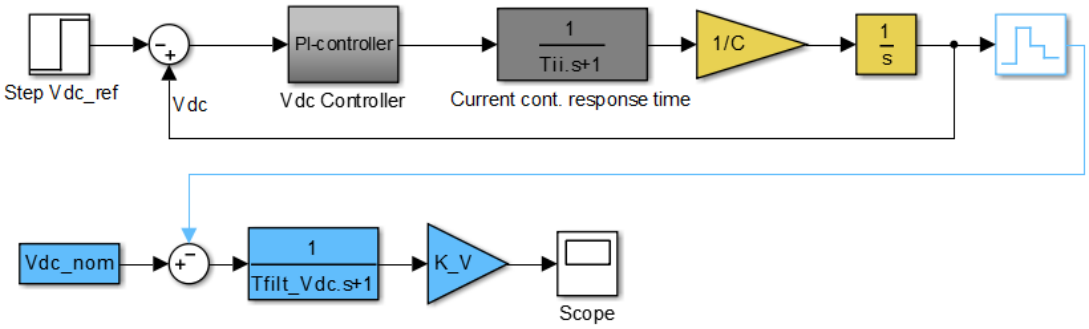

Figure 40: Validation of the voltage support control in the WF.

7.5 DC voltage Control

Figure 41 shows the voltage control as it is implemented in Simulink. The voltage PI controller parameters are found through data fitting with measurements from the lab. The inner current control loop is modelled as a first order response with the time constant T_{ii}. The value of T_{ii} was found from measurements performed in the specialization project [3]. One of the assumptions made when developing the simulation model is to neglect the resistance in the DC transmission network. This is further explained in Section 7.6. With this simplification, all capacitances can be aggregated into a single value, C which is estimated from the converter filter capacitances. Figure 47 shows a comparison of the voltage response from the simulation model and the laboratory model when a step in the reference is applied. It can be seen that the match is good.

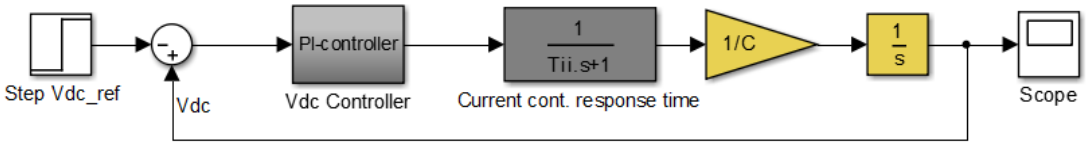

Figure 41: Validation of DC voltage control with step in DC voltage reference. Comparison between laboratory measurements and simulation results.

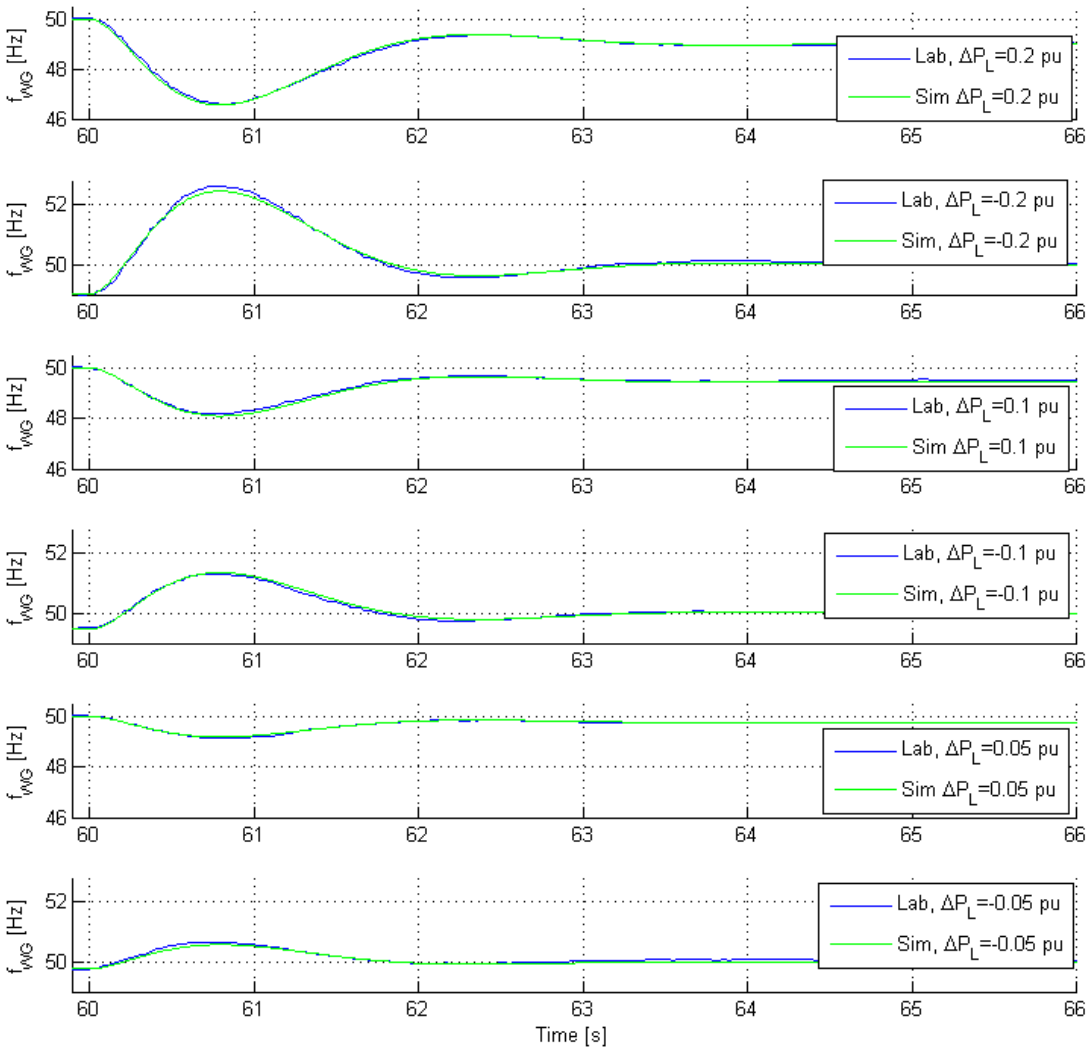

Figure 42: The frequency response in the weak grid during different imbalances in system load. Positive ΔP_L results in deficit of power, while negative ΔP_L results in surplus of power.

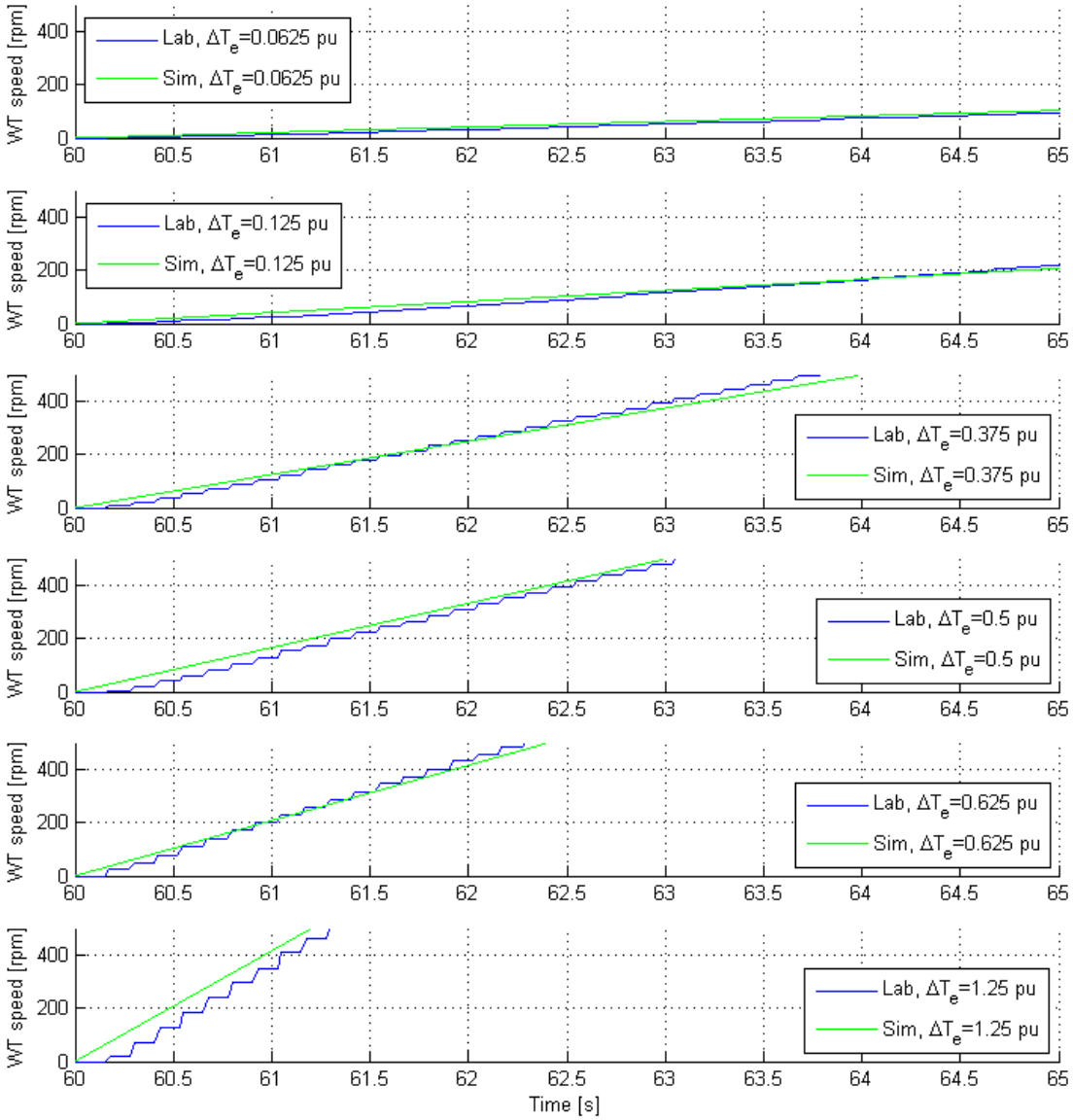

Figure 43: The wind farm speed for different steps in electrical torque. Comparison between laboratory measurements and simulation results.

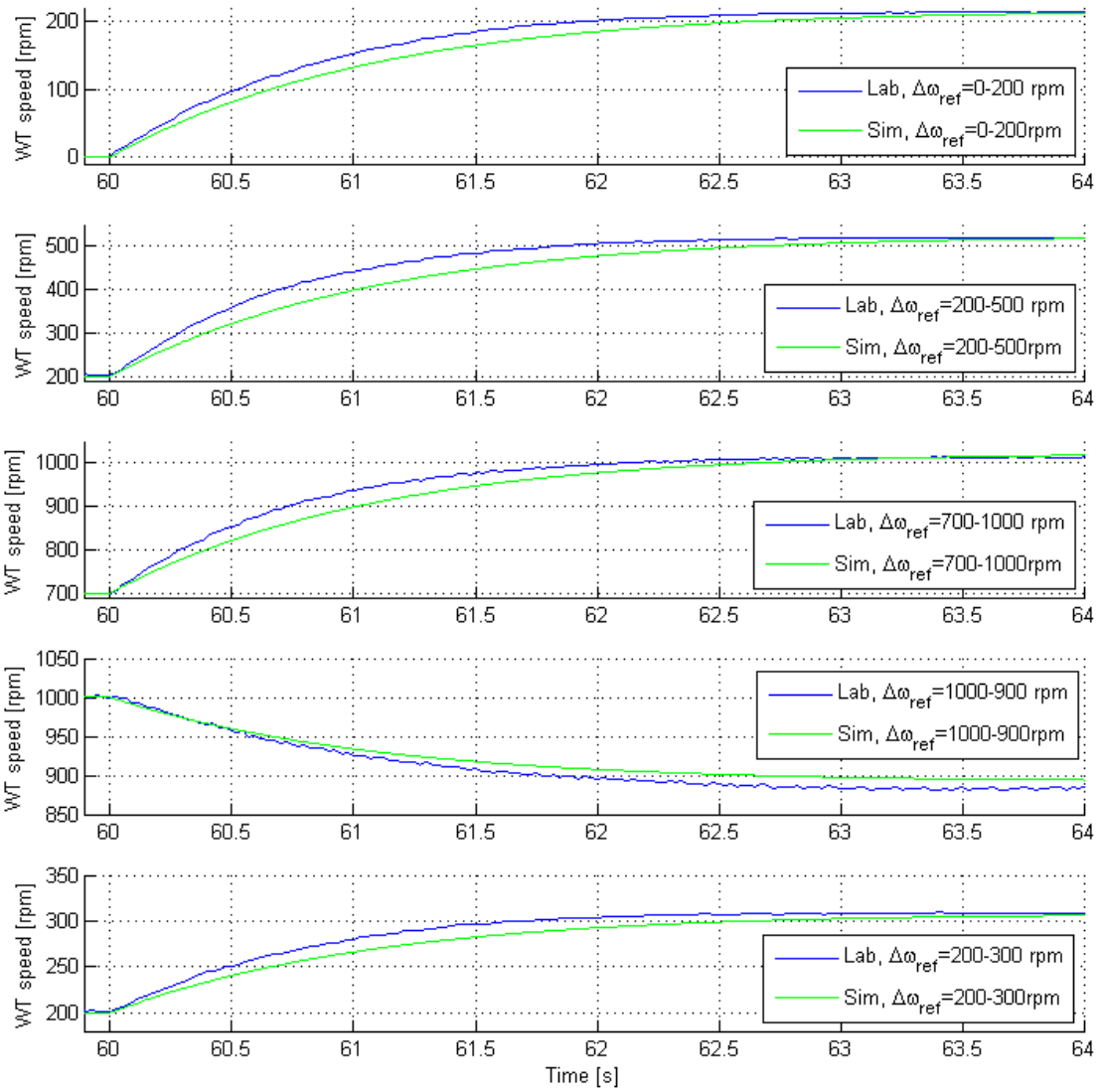

Figure 44: The wind speed as function of time when different steps in the speed reference is applied. Comparison between the response in the lab and the response in the simulation model. During the experiment the wind torque T_{wind} was zero.

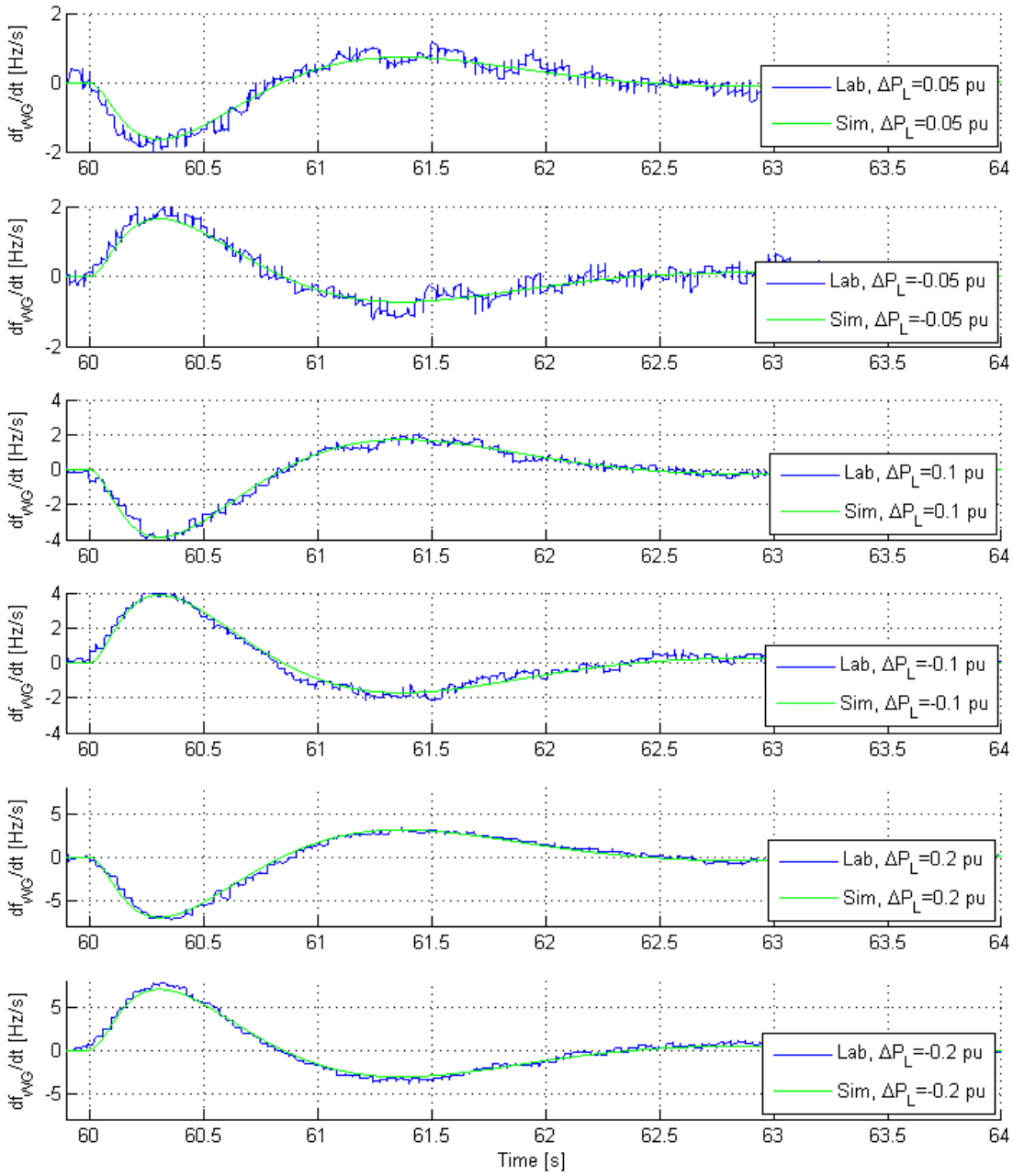

Figure 45: The frequency derivative in the weak grid during different imbalances in system load. Comparison between laboratory measurements and simulation results.

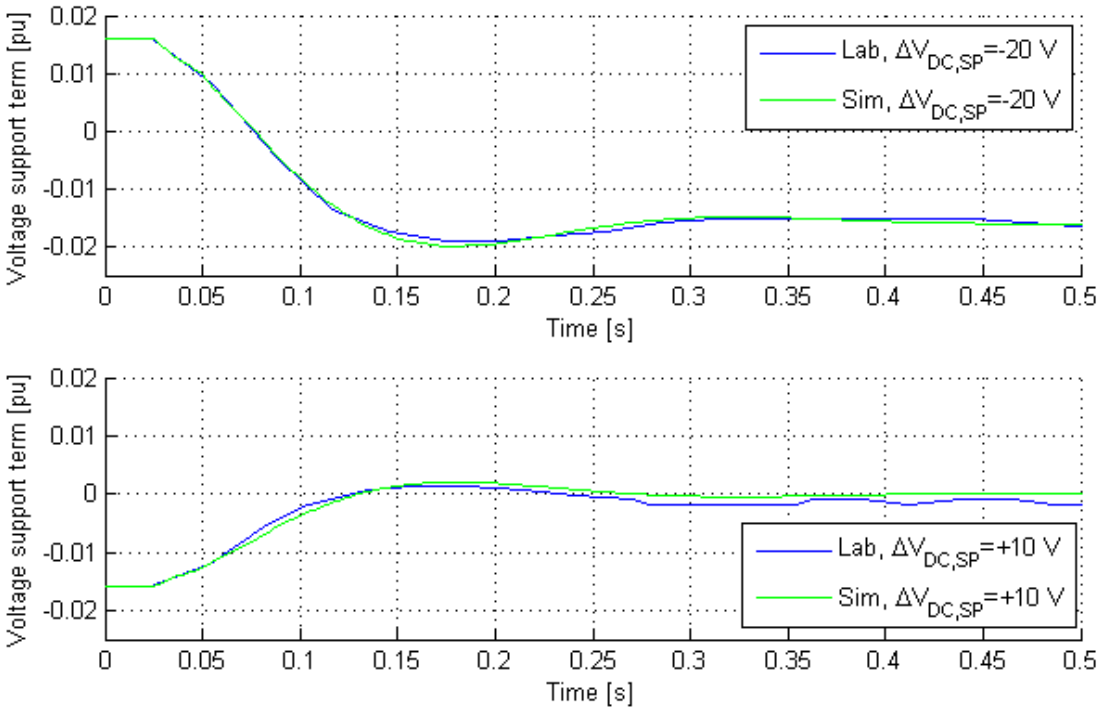

Figure 46: Inertia term in wind farm converter. Comparison between laboratory measurements and simulation results.

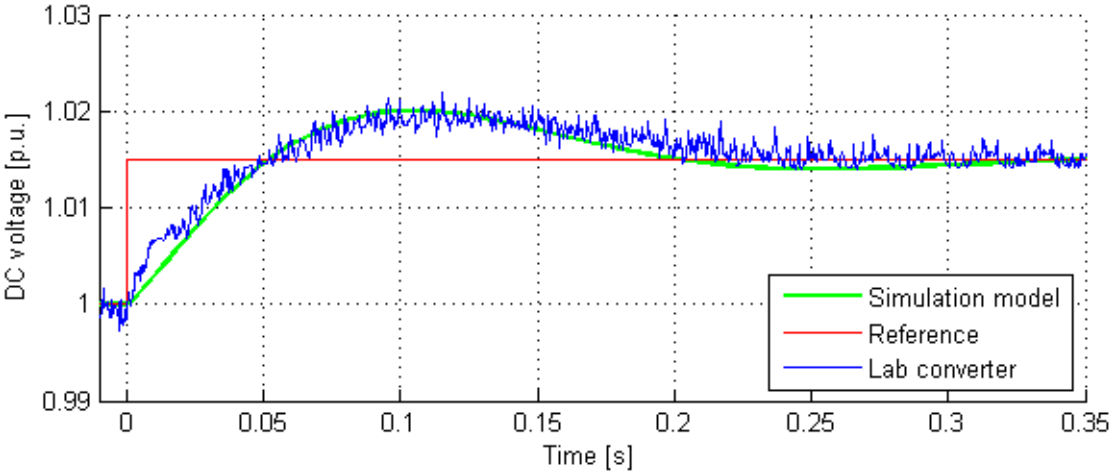

Figure 47: DC voltage during step in reference from 1-1.015 p.u. at t=0. Comparison between laboratory measurements and simulation results.

7.6 Challenges and assumptions

During the course of this work some challenges with the laboratory model were discovered. Some of these challenges led to simplifications in the simulation model, while others were solved. This section addresses some of the challenges and discusses the assumptions laid at ground in the simulation model.

7.6.1 Assumption: the WG AC voltage is constant

It is possible to suddenly connect or disconnect a load resistor bank in the laboratory set-up. Still, the power consumed by the load does not follow a step response due to the voltage drop associated with the increased loading of the generator. The upper graph in Figure 48 shows the RMS AC voltage in the weak grid during a step in load. The inertia emulation and voltage support are disabled. It can be seen that at the connection of the load, the voltage drops and is eventually brought back to its initial value by the AVR. The voltage drops to as low as 370 V which is 92.5 % of its nominal value. Since the load is proportional to the AC voltage squared, the size of the load will be 85.6 % of its value in the point where the voltage is at its lowest. This relation is not embedded in the Simulink model. The simulation model assumes that the AC voltage in the weak grid is constant equal to 1 pu. However, it is clear that that this does not apply in the real system.

7.6.2 Assumption: the DC voltage is the same at both terminals

The simulation model assumes that the DC voltage is the same at both terminals. In reality, the steady state DC voltages will be slightly different due to the resistances in the DC cables. The maximum RC time constant of the DC cable corresponding to the maximum DC cable resistance is:

$$\tau_{max} = R_{DC,max}C = 0.3\ \Omega \cdot 14\ mF = 4.2\ ms \tag{7.1}$$

Since τ_{max} is small, it is assumed that the dynamics of the DC cable has a small impact on the frequency response in the weak grid and it is considered valid to assume that the DC voltages are the same at both terminals. Since the losses in the DC cable are neglected, the power extracted from the wind farm is assumed equal to the power injected to the weak grid.

7.6.3 Assumption: the inner loop controls can be modelled as first order responses

The inner loop controls in both converters are modelled as first order responses. In [3] the time response of the converter current control was found to be in the range of 1-2 milliseconds. The time constant of the inner torque control in the second converter is in the same time range. Hence, the assumption is considered valid.

7.6.4 Challenge: frequency measurement in the laboratory model

In practice, the frequency measurement should be made locally, which in most cases means that the frequency is obtained within the converter, typically from the PLL. In general, this is challenging because there are no rotating parts in a VSC, so the frequency must be obtained from voltage measurements, which are typically distorted and contains noise. This will in turn make it even more challenging to differentiate the frequency. It is therefore necessary to use filters when calculating the frequency derivative in a converter. The converters that are used in the laboratory model presents another challenge since the PLL frequency measurement has a resolution of 0.1 Hz. This is too low to achieve a precise measurement of the frequency derivative.

To solve this problem, the speed measurement from the synchronous generator is used instead of the PLL frequency. The generator speed is measured by using an encoder. However, the dynamic response of the encoder is not known. In addition, the use of filters in the National Instrument Data Acquisition device (DAQ) which is used to log the frequency, is also unknown. When comparing the frequency signal from the DAQ to the PLL frequency, the DAQ-frequency seems to be delayed with a time constant in the range of 200-300 milliseconds.

The consequence of filtering the frequency measurement from the encoder is that the signal shows a slower frequency response than what is really the case. This is critical when the objective of the control that takes the frequency derivative as input, is to contribute with frequency support. The filter will lead to a delay in the frequency support, which means that the frequency will have dropped to a lower value before the system receives support to stabilize the frequency. Another consequence is that the unknown behaviour of the DAQ makes it challenging to model the synchronous generator in simulations.

7.6.5 Challenge: observed oscillations in the WG AC voltage

It is observed that the AC voltage oscillates during the load imbalance in the weak grid. The oscillations increase with increased inertia support, which can be seen in Figure 48. In the upper graph the inertia emulation and voltage support are disabled. In the bottom graph, the gains are high, and it is clear that the AC voltage is more oscillating than in the upper graph. Since the structure of the governor and AVR controls that are implemented in the synchronous generator in the lab are largely unknown, some difficulties were experienced when trying to recreate the frequency response from the weak grid equivalent. Due to the unknown control structures, the origin of the observed oscillations is hard to determine. Nevertheless, it is obvious that the converter amplifies the oscillations when inertia support is added.

7.6.6 Challenge: the effect of stored capacitive energy in the DC network

As illustrated in Section 5.5, when there is a step in the load in the weak grid, the inertia term will reduce the DC voltage set-point. When the DC voltage reduces, a given amount of energy will be released from the capacitances in the system. This "surplus" energy will flow into the weak grid, and affect the frequency transient following an imbalance in load. Figure 49 shows simulation results of this effect. It can be seen that the extra energy from the capacitances helps to reduce the ROCOF, but makes the nadir lower. There is also an overshoot when the frequency is rising that occurs because the capacitors have to recharge. It can be concluded that it is important to regard not only the power flowing from the one side of the converter to the other, but also the energy stored in the components that make up the DC network.

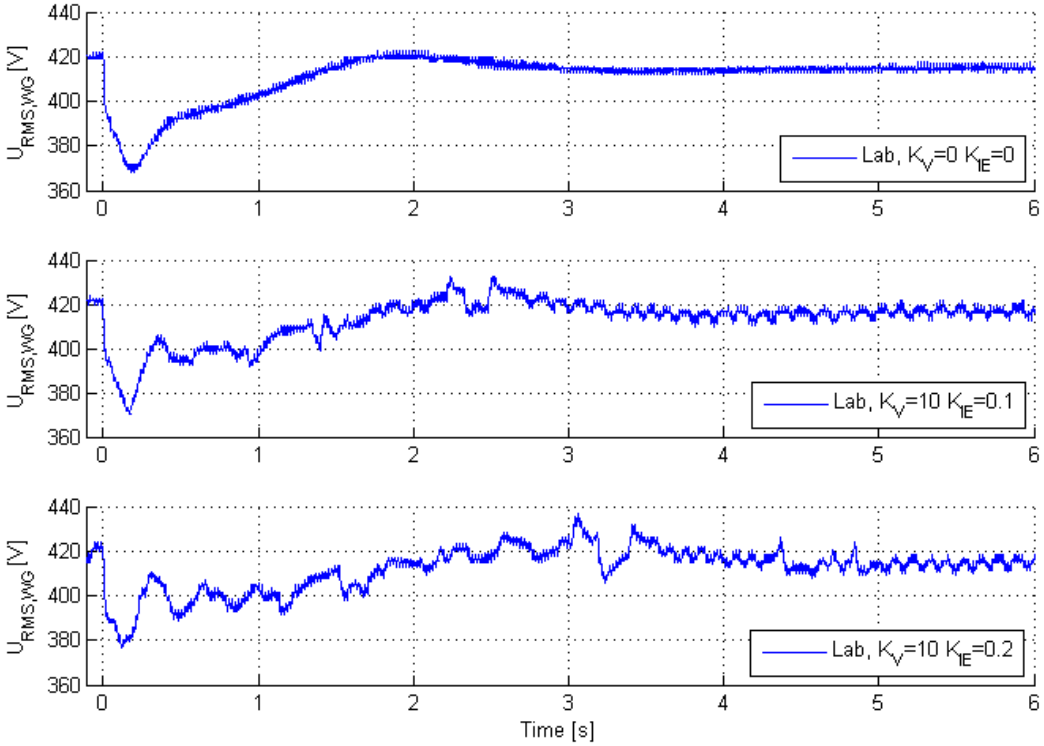

Figure 48: Measured RMS voltage in weak grid equivalent, for different combinations of K_{IE} and K_V.

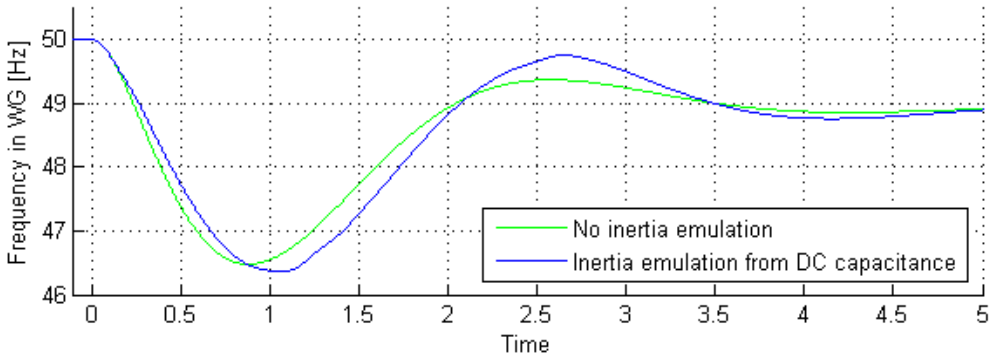

Figure 49: Simulation analysis showing the impact of the "surplus" capacitor energy that occurs from reducing the DC voltage on the frequency in the weak AC grid.

8. Case Studies

8.1 Effect of changing the gains in the inertia emulation and voltage support control loops

The value of the gains in the inertia emulation and voltage support control loops have a large impact on the frequency response following a load imbalance in the weak grid. The inertia emulation gain K_{IE} amplifies the change in frequency following an imbalance, and decreases the DC voltage set-point on the VSC converter terminals. The second converter terminal will respond to the deviation from nominal DC voltage by modifying the torque reference and taking energy that is stored in the rotating mass of the wind turbines with the purpose of restoring the power imbalance in the weak grid. The size of the deviation in DC voltage is amplified by the voltage support gain K_V and is proportional to the change in the speed of the wind turbine. See Section 5.3 and Section 5.4 for control block diagrams.

This section studies the effect of changing these gains by comparing the WG frequency response for different values and combinations of K_{IE} and K_V. The DC voltage on the WG connected converter terminal is also considered during the experiments. The goal is to improve both the ROCOF and the nadir of the frequency response in the weak grid following a large load imbalance.

For all cases, the load imbalance is 0.25 p.u. and with a rather slow acting speed control on the machine in the weak grid, this leads to a large dip in the system frequency. The disturbance is exaggerated to illustrate a worst case scenario. For all combinations of gains, the frequency response without support is also included. This is addressed as "base case", and is shown to illustrate the improvement that is achieved with inertial support from the VSC-HVDC connected wind farm.

8.1.1 Inertia emulation gain $\mathbf{K_{IE} = 0.1}$

The upper graph in Figure 50 shows the WG frequency response for an inertia emulation gain $K_{IE} = 0.1$ and varying the voltage support gain K_V in the range of 10-100. It is interesting to see that during the first part of the frequency transient, until about 400 millisecond have elapsed, the weak grid does not receive any frequency support. This is due to the system dynamics and the time delay associated with the control loops that are implemented. For instance, it takes approximately 250 milliseconds to measure and differentiate the frequency in the weak grid until the signal is sent to the DC voltage control. Continuing into the voltage support

control loop and reaching the torque control in the wind farm equivalent takes another 150 milliseconds, not regarding the dynamics of the inner loops in the converters or the DC grid itself. In total, only the inertia emulation and voltage support control loops have a time delay of approximately 400 ms.

Some key numbers from the results shown in the upper graph in Figure 50 are summarized in Table 9. The voltage support gain that results in the best improvement of the nadir is $K_V = 100$. However, the improvement compared to the improvement when $K_V = 40$ is only 0.8 %. Also, by looking at the frequency response when $K_V = 100$ it can be seen that the trajectory is more oscillatory than when $K_V = 40$. Hence, by increasing the K_V above 40 when K_{IE} is 0.1, gives a small improvement in the nadir, but brings the system close to its stability limit.

In Figure 51 it can be seen how the inertia emulation control decreases the DC voltage at the DC terminals of the weak grid. Since the inertia emulation gain is the same for all cases, the DC voltage decreases with the same amount independent on the value of the voltage support gain. The DC voltage trajectory for the highest voltage support gain oscillates which confirms that the system is close to its stability limit. The DC voltage is decreased with 5 V when $K_{IE} = 0.1$.

It is difficult to determine the origin of the DC voltage oscillations, since they are a result of the total system response following the disturbance in the weak grid. A simplified illustration of interactions between implemented controls was made in Section 5.5. To some extent, this gives an impression of the system dynamics that may cause or excite observed DC voltage oscillations.

8.1.2 Inertia emulation gain $\mathbf{K_{IE} = 0.2}$

The middle graph in Figure 50 shows the WG frequency response in the weak grid during a load imbalance with $K_{IE} = 0.2$ and varying K_V in the range of 10-60. Figure 52 shows the corresponding DC voltage at the DC terminals of the weak grid. Regarding the frequency response, it takes approximately 400 milliseconds before the weak grid receives frequency support from the wind farm for the same reasons as explained in the section above. The key results are summarized in Table 10. The best improvement in the nadir is 47.5 % based on the steady-state frequency deviation, and is achieved when $K_V = 60$. However, by looking at the DC voltage, it can be seen that it is oscillating and it may appear as if system is close to its stability limit. DC voltage oscillations are also present when the voltage support gain is 40, but they are less visible when the gain is decreased to 20. Going from $K_V = 60$ to $K_V = 20$ is not a large sacrifice in terms of nadir improvement, which will be 0.33 Hz less, but in terms of when the nadir appears in time it means that the frequency will reach its minimum approximately 300 milliseconds earlier. Nevertheless, the inertia emulation and voltage support controls should not jeopardize the stability of the system. Hence, a lower voltage support gain, not

giving the best improvement in the frequency response but resulting in less DC voltage oscillations, may be favourable to a large gain giving the best improvement in the frequency response but leading to DC voltage oscillations.

8.1.3 Inertia emulation gain $\mathbf{K_{IE} = 0.3}$

The lower graph in Figure 50 shows the WG frequency response in the weak grid during a load imbalance with $K_{IE} = 0.3$ and varying K_V in the range of 10-50. Figure 53 shows the corresponding DC voltage at the DC terminals of the weak grid. Regarding the frequency response, key results can be seen in Table 11. The best improvement in nadir is 48.2 %, and is achieved when $K_V = 50$. However, similar to the results from the other cases, it can be seen that the DC voltage oscillates. The DC voltage oscillations appear for $K_V = 50$, $K_V = 40$ and $K_V = 20$, but are not distinct for $K_V = 10$. The improvement of the nadir with $K_V = 10$ is 27.8 % which is not the best improvement possible when also regarding oscillations in the DC voltage in the overall assessment of the performance of the control loops.

8.1.4 Choice of parameters

This thesis does not seek to find the optimal value or combination of K_{IE} and K_V. Based on the results from the different combinations of the gains, it is chosen to use $K_{IE} = 0.2$ and $K_V = 0.2$ for further analyses of the system. This combination gives an 34.5 % improvement in the frequency nadir and does not cause oscillations in the DC voltage.

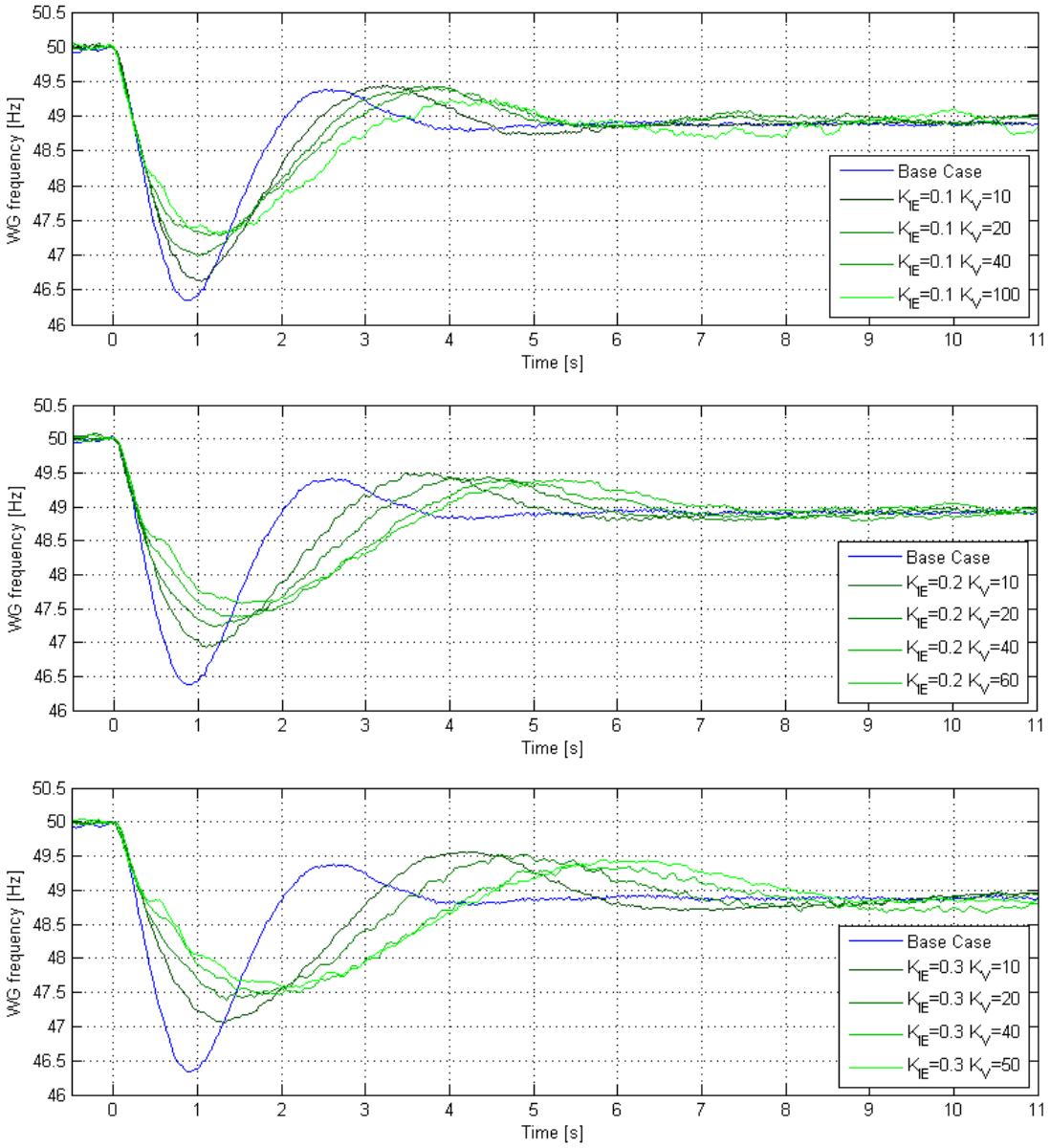

Figure 50: Laboratory measurements of the frequency response following a step in load of $\Delta P_L = 0.25$ p.u. in the weak AC grid equivalent. The experiments were performed with combinations of K_{IE} and K_V.

Table 9: Results from frequency response in WG for $K_{IE} = 0.1$.

	Base Case	**K_V=10**	**K_V=20**	**K_V=40**	**K_V=100**
Initial ROCOF [Hz/s]	5.00	5.00	5.00	5.00	5.00
Nadir [Hz]	46.35	46.63	46.99	47.28	47.30
Nadir improvement [Hz]		0.28	0.64	0.93	0.95
Nadir improvement [%]		11.0	25.1	36.5	37.3
Nadir time [s]	0.85	1.00	1.00	1.13	1.28
Nadir time impr. [s]		0.15	0.15	0.28	0.43

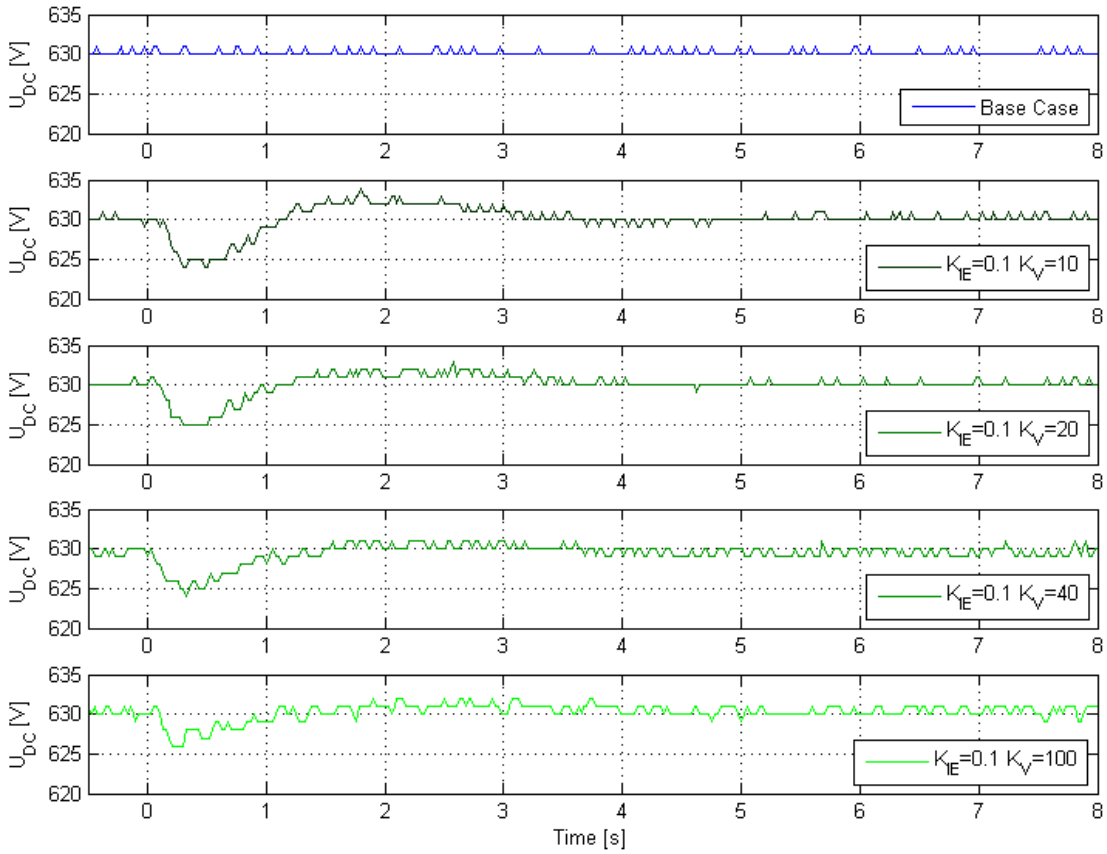

Figure 51: Laboratory measurements of the DC voltage following a step in load of $\Delta P_L = 0.25$ p.u. in the weak AC grid equivalent. The experiments were performed with $K_{IE} = 0.1$ for different values of K_V.

Table 10: Results from frequency response in WG for $K_{IE} = 0.2$.

	Base Case	**K_V=10**	**K_V=20**	**K_V=40**	**K_V=60**
Initial ROCOF [Hz/s]	5.00	5.00	5.00	5.00	5.00
Nadir [Hz]	46.35	46.93	47.23	47.37	47.56
Nadir improvement [Hz]		0.58	0.88	1.02	1.21
Nadir improvement [%]		22.7	34.5	40.0	47.5
Nadir time [s]	0.85	1.10	1.20	1.48	1.53
Nadir time impr. [s]		0.25	0.35	0.63	0.68

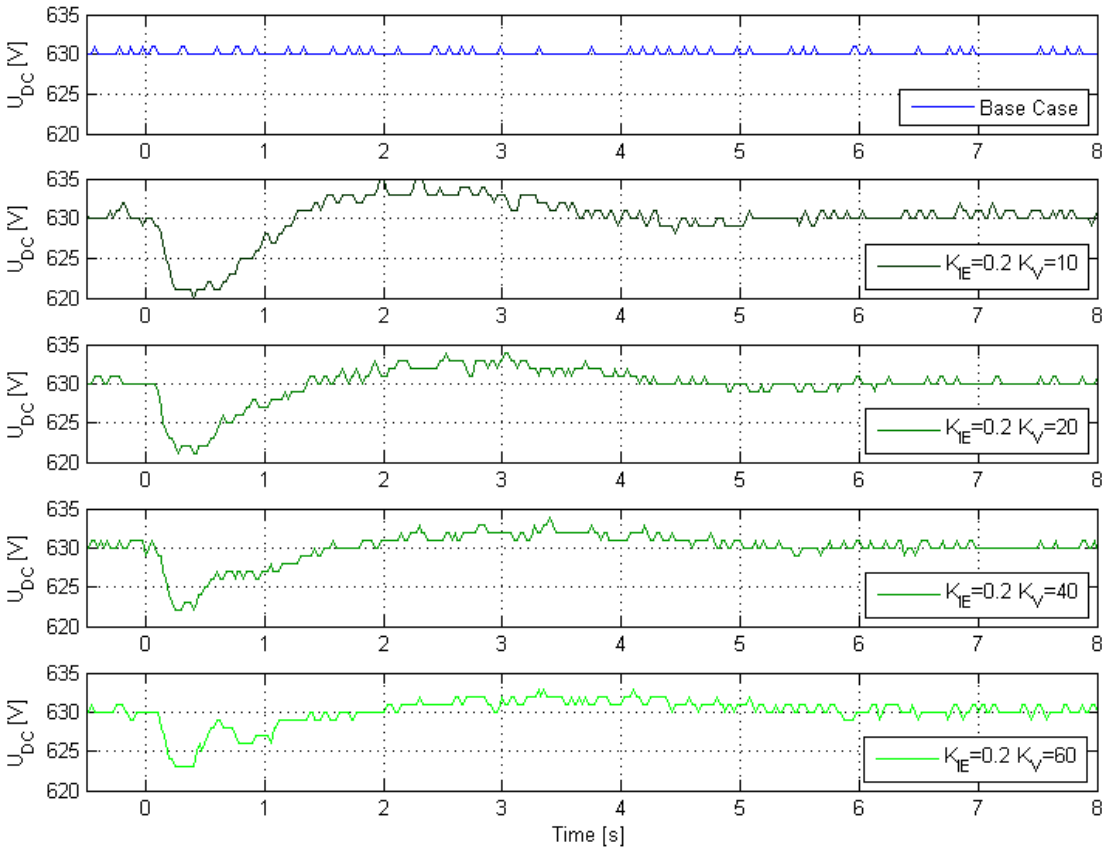

Figure 52: Laboratory measurements of the DC voltage following a step in load of $\Delta P_L = 0.25$ p.u. in the weak AC grid equivalent. The experiments were performed with $K_{IE} = 0.2$ for different values of K_V.

Table 11: Results from frequency response in WG for $K_{IE} = 0.3$.

	Base Case	K_V**=10**	K_V**=20**	K_V**=40**	K_V**=50**
Initial ROCOF [Hz/s]	5.00	5.00	5.00	5.00	5.00
Nadir [Hz]	46.35	47.06	47.40	47.47	47.58
Nadir improvement [Hz]		0.71	1.05	1.12	1.23
Nadir improvement [%]		27.8	41.2	43.9	48.2
Nadir time [s]	0.85	1.30	1.35	1.98	2.15
Nadir time impr. [s]		0.45	0.50	1.13	1.3

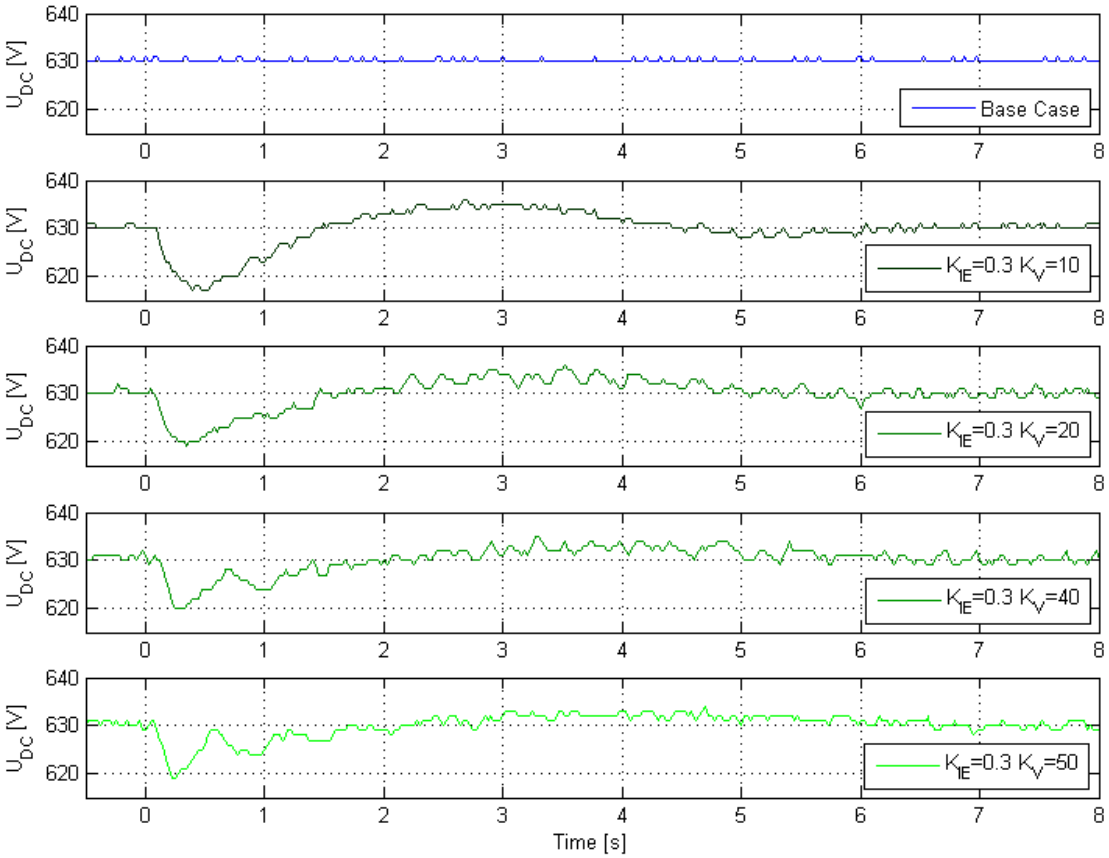

Figure 53: Laboratory measurements of the DC voltage following a step in load of $\Delta P_L = 0.25$ p.u. in the weak AC grid equivalent. The experiments were performed with $K_{IE} = 0.2$ for different values of K_V.

8.2 The effect of the DC droop on the frequency support

The effect of DC droop on the amount of power support from the wind farm during a load imbalance in the weak grid was demonstrated in Section 5.5. It can be seen from Equation 5.3 that during the first part of the frequency trajectory following a load imbalance in the weak grid, the change in DC voltage ΔV_{DC} is also dependent on the droop coefficient R_{droop}. Removing the DC droop is equivalent to a large droop coefficient, $R_{droop} = \infty$. It can be seen from the aforementioned equation that for a large droop coefficient, ΔV_{DC} will be larger. This will increase the change in DC power flowing in the DC cable ΔP_{DC}, as seen in Equation 5.4. In other words, removing the DC droop should in theory increase the frequency support from the wind farm.

The upper graph in Figure 54 shows the laboratory measurements of the frequency in the weak grid following a step in load for different values of the droop coefficient R_{droop}. The experiments were performed with $K_{IE} = 0.2$ and $K_V = 20$. It can be seen that there is no difference between the experiments with droops of 8.4 % and 6.3 %. There is however an improvement in the response when the DC droop is removed and the weak grid terminal acts as a master node. The improvement in the nadir is approximately 0.15 Hz with a time lag of approximately 200 milliseconds compared to the cases with DC droop.

The effect of removing the DC droop is smaller than expected. This is because ΔV_{DC} is relatively small, and the resulting ΔP_{DC} is also relatively small. Hence, during the transient period following the load imbalance, the operating point on the droop line is close to the steady state operating point. See Figure 22 for an illustration of droop line dynamics during the imbalance. Therefore, the consequence of removing the droop has a small effect on the frequency support. Also, the effect is less visible in the laboratory results compared to the simulation results which are shown in the lower graph because the resolution of the voltage measurement in the lab i 1 V which is too low to sense the small change in DC voltage when removing the droop. A comparison of laboratory measurements and simulation results of the DC voltage is given in Figure 55. In the simulations it can be seen that the difference between the change in DC voltage with and without droop is approximately 2 V. This difference in not visible in the corresponding laboratory measurement due to the low resolution of the voltage measurement. Nevertheless, Figure 54 shows that there is a small improvement in the frequency response, which is in compliance the theory discussed above.

Another observation was made when testing the system without DC droop. The lower graph in Figure 54 shows simulation measurements of the frequency response in the weak grid following a load imbalance, for different values of the droop

coefficient R_{droop}. It can be seen that without DC droop the frequency response is more oscillating. This effect is also visible in the DC voltage measurement from the simulation model in Figure 55. When increasing the droop coefficient, the converter terminal goes from being a voltage node to relating DC voltage change to the power flowing in the DC cable. Since the change in DC voltage is directly related to the DC power, the droop acts as a resistance during the transient state of the system, which will have a dampening effect on power oscillations.

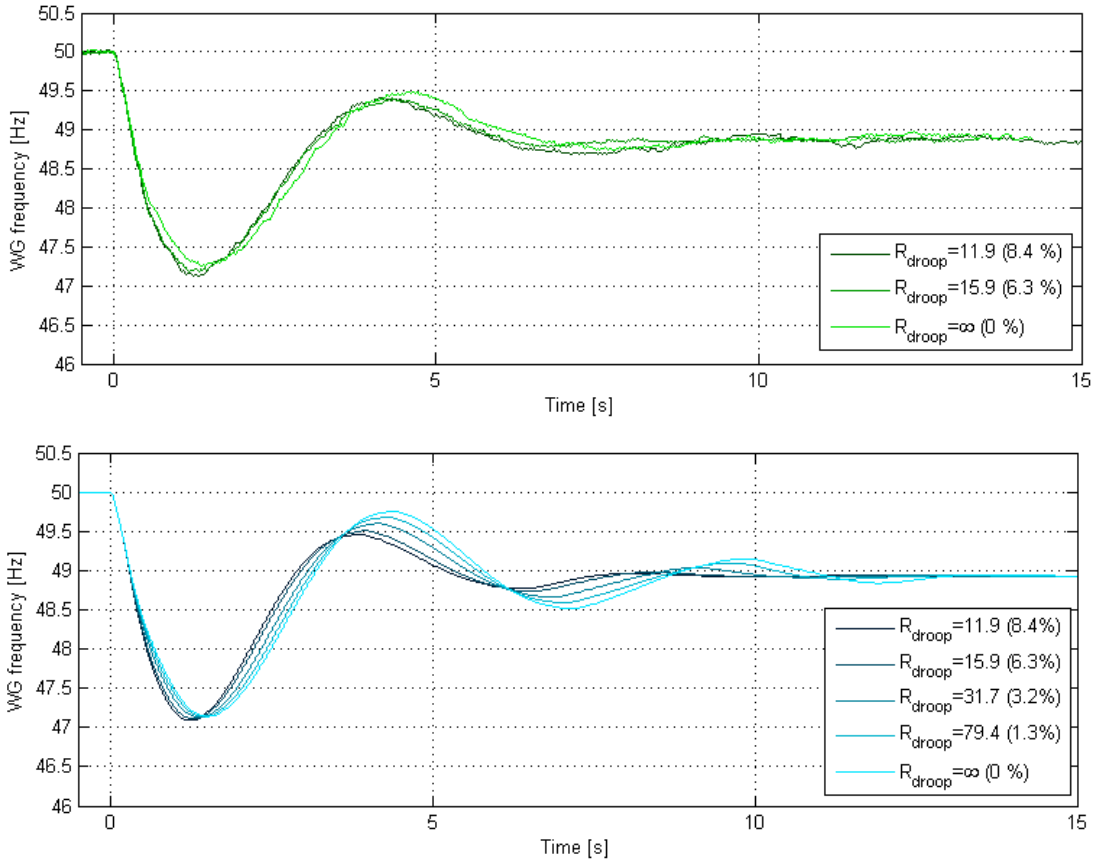

Figure 54: WG frequency following a step in load of $\Delta P_L = 0.25$ p.u. in the weak AC grid equivalent for different values of the droop coefficient R_{droop}. The experiments were performed with $K_{IE} = 0.2$ and $K_V = 20$. Upper graph shows laboratory measurements and lower graph shows simulation results.

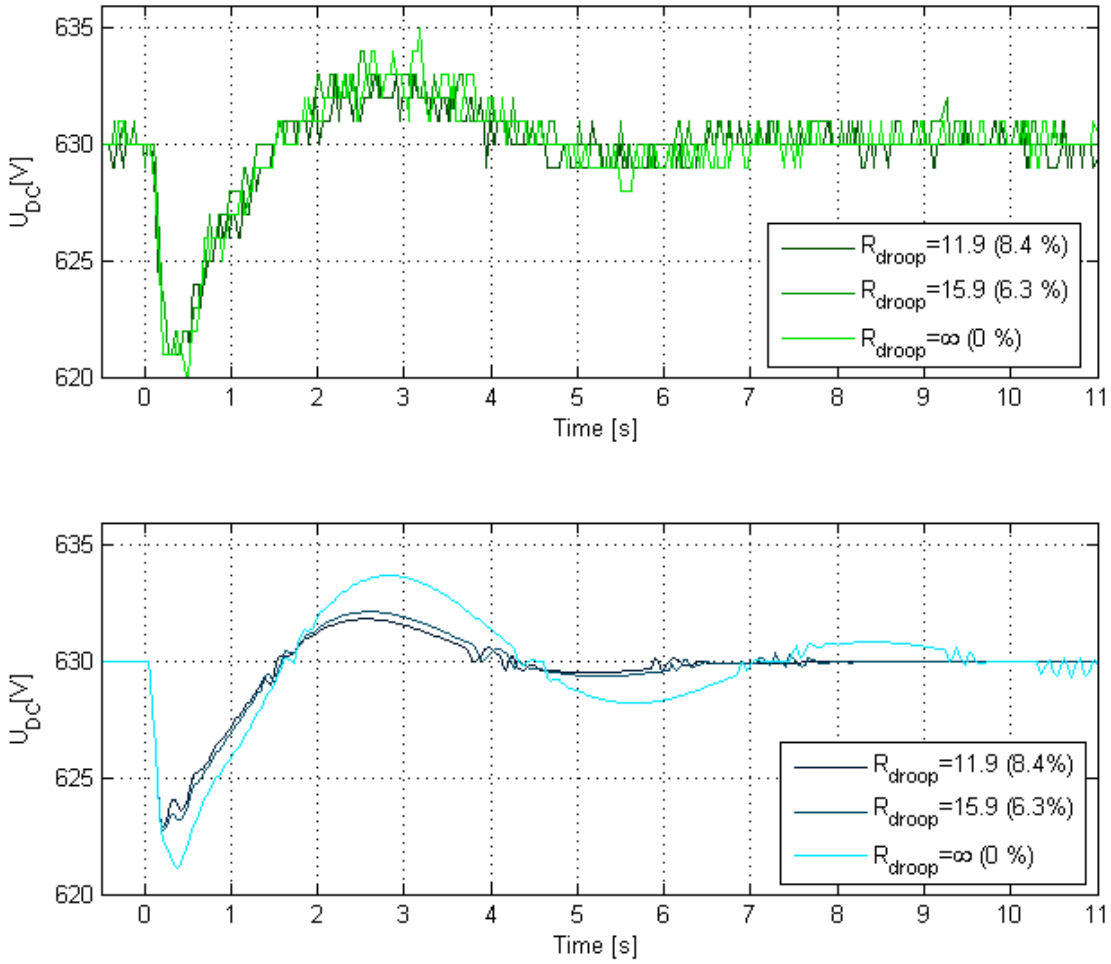

Figure 55: Comparison of laboratory measurements (upper) and simulation (lower) of the DC voltage on the WG terminals following a step in load of $\Delta P_L = 0.25$ p.u. in the weak AC grid equivalent for different values of the droop coefficient. The experiments were performed with $K_{IE} = 0.2$ and $K_V = 20$.

8.3 The effect of wind turbine operating point

The effect of the wind turbine operating point will have an impact on the amount of inertia support that the wind farm equivalent is able to provide. The operating point of a real wind turbine concerns several parameters. The variable speed turbine will operate according to a power curve that for all wind speeds, maximizes the power output, as discussed in Section 3.2. However, as explained in Section 5.4.1, the wind farm equivalent used in the laboratory model does not have a power output maximizing control. Therefore, during the assessment of the effect of wind turbine operating point, the power maximizing curve was not taken into account. For a load imbalance of $\Delta P_{DC} = 0.25$ p.u. in the weak grid equivalent with $K_{IE} = 0.2$ and $K_V = 20$, the effect of the wind turbine operation point is analysed only by varying the wind turbine speed reference between 200 rpm and 1000 rpm.

Figure 56 shows laboratory measurements of the frequency in the weak grid. It can be seen that increasing the wind turbine speed improves the frequency response. This is expected since change in wind farm power is proportional with the wind turbine speed, as shown in Equation 5.4. Figure 57 shows the change in wind turbine speed $\Delta\omega_{WT}$ during the inertial support. Since the load imbalance in the weak grid is the same for all cases, short-sighted thinking implies that $\Delta\omega_{WT}$ will be also be the same in all cases. However, it can be seen in Figure 57 that this is not the case. For an increasing wind turbine speed reference, the change in the turbine's speed during the transient event decreases. This can be explained by considering the coordinated system response to the load imbalance. With higher wind turbine speed, more inertial support will reach the weak grid. This will improve the frequency derivative, and the reference for inertia support will decrease. Therefore, the change in wind turbine speed is lower for high speed references. Note that the instant at which the weak grid receives inertial support from the wind farm equivalent is the same regardless of the operating point of the turbine.

The effect of varying the wind turbine operating point was also analysed in the simulation model. The results are shown in Appendix 10.2. It can be seen that the simulation model gives the same results as the laboratory set-up discussed above. A plot showing the DC voltage is also included in the appendix.

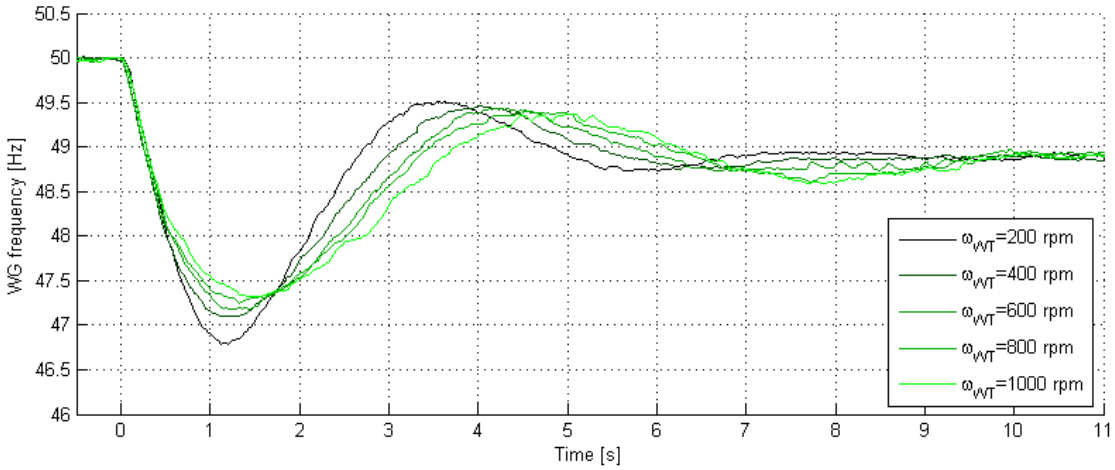

Figure 56: Laboratory measurements of the WG frequency following a step in load of $\Delta P_L = 0.25$ *p.u. in the weak AC grid equivalent for different WT speeds. The experiments were performed with* $K_{IE} = 0.2$ *and* $K_V = 20$.

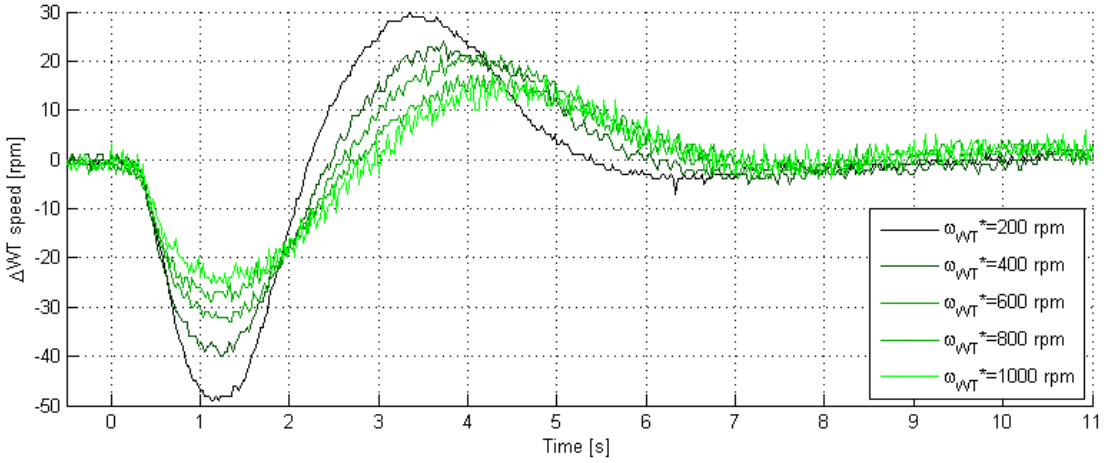

Figure 57: Laboratory measurements of the change in wind turbine speed during inertia emulation for different operating points. The experiments were performed with $K_{IE} = 0.2$ *and* $K_V = 20$.

8.4 Simulation study: what brings the system towards instability?

During the experiments in Section 8.1 to Section 8.3 some observations on what brings the system towards instability were made. Based on this, a simulation study was made where some parameters are varied in order to push the system towards instability. The results are presented in the following sections.

8.4.1 DC droop

Figure 59 shows simulation results of the WG frequency, DC voltage and DC power during a load imbalance in the weak grid for different values of the DC droop coefficient R_{droop}. It can be seen that for a decreasing R_{droop} the system gets more oscillatory and for the smallest value of R_{droop} the system is unstable. In practice, decreasing R_{droop} means that the converter terminal changes towards having the characteristics of a power node. Having two nodes trying to determine the power at their terminals, is not possible. The results is that power will oscillate between the weak grid and the wind farm equivalent. In addition, for a given change in DC power ΔP_{DC}, the resulting change in DC voltage ΔV_{DC} will be larger when R_{droop} is smaller, see Figure 58. This will also lead to power oscillations.

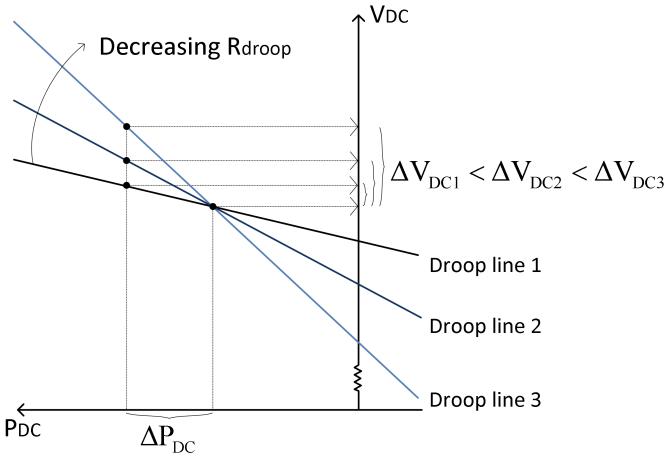

Figure 58: Illustration of effect of decreasing R_{droop}. For a given change in power ΔP_{DC}, the resulting change in DC voltage ΔV_{DC} increases for a decreasing droop coefficient R_droop.

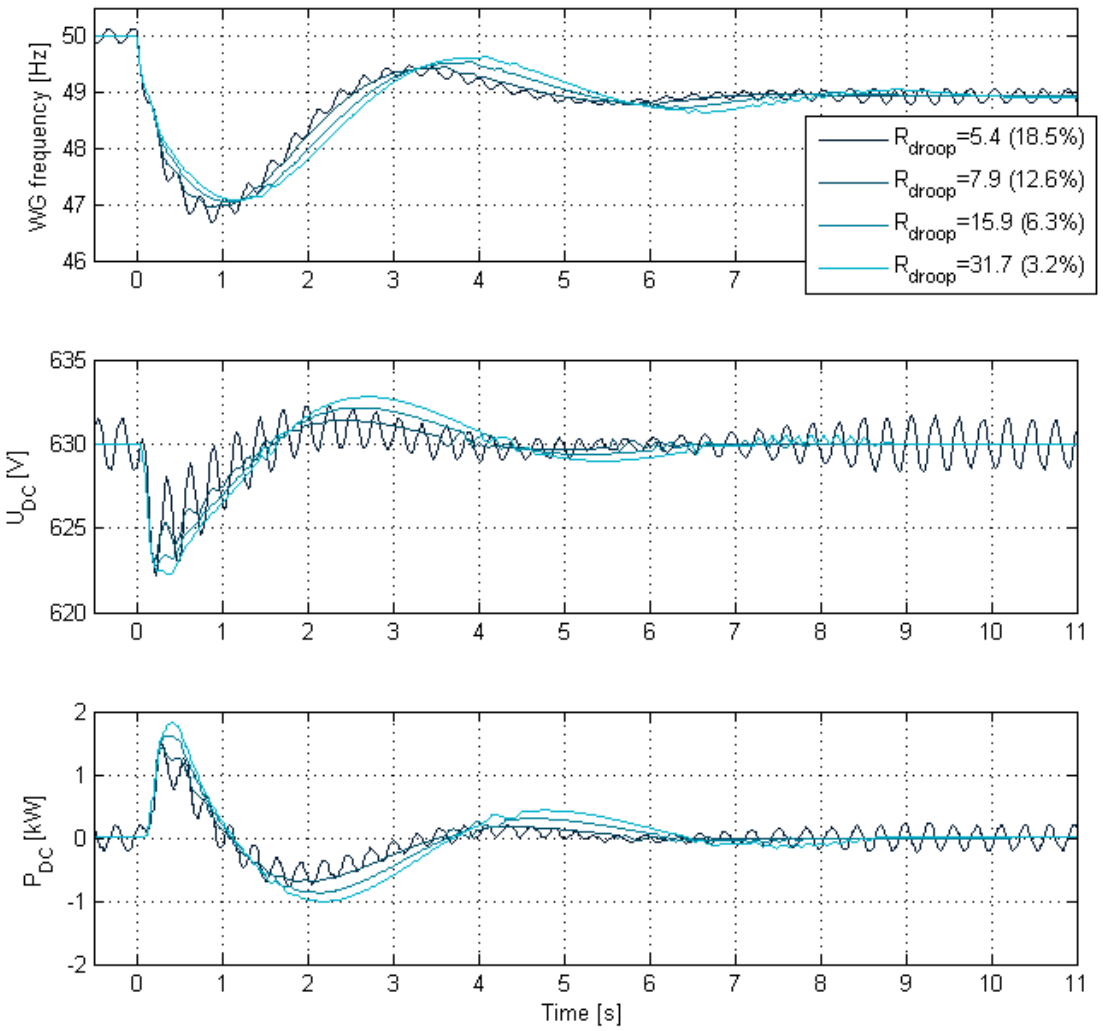

Figure 59: Simulation results showing the speed in the weak grid, the DC voltage and the power flowing in the DC cable following a step in load of $\Delta P_L = 0.25$ p.u. in the weak AC grid equivalent for different values of the droop coefficient R_{droop}. The experiments were performed with $K_{IE} = 0.2$ and $K_V = 20$.

8.4.2 Gains

Any control system can push the system that it controls towards instability. A simulation study was performed with increasing the inertia emulation gain and the voltage support gain until the system showed signs of instability. Figure 60 shows the simulation results from varying the inertia emulation gain K_{IE}. During this experiment the voltage support gain was kept constant equal to $K_V = 20$. It can be seen that increasing K_{IE} from 0.2 to 0.4 improves the frequency response in the weak grid but results in oscillations in the DC voltage. The system becomes oscillating for $K_{IE} = 0.8$.

Figure 61 shows the simulation results from varying the voltage support gain K_V. During this experiment the inertia emulation gain was kept constant equal to $K_{IE} = 0.2$. It is clear from looking at the WG frequency, DC voltage and DC power, that the system is oscillating for $K_V = 65$.

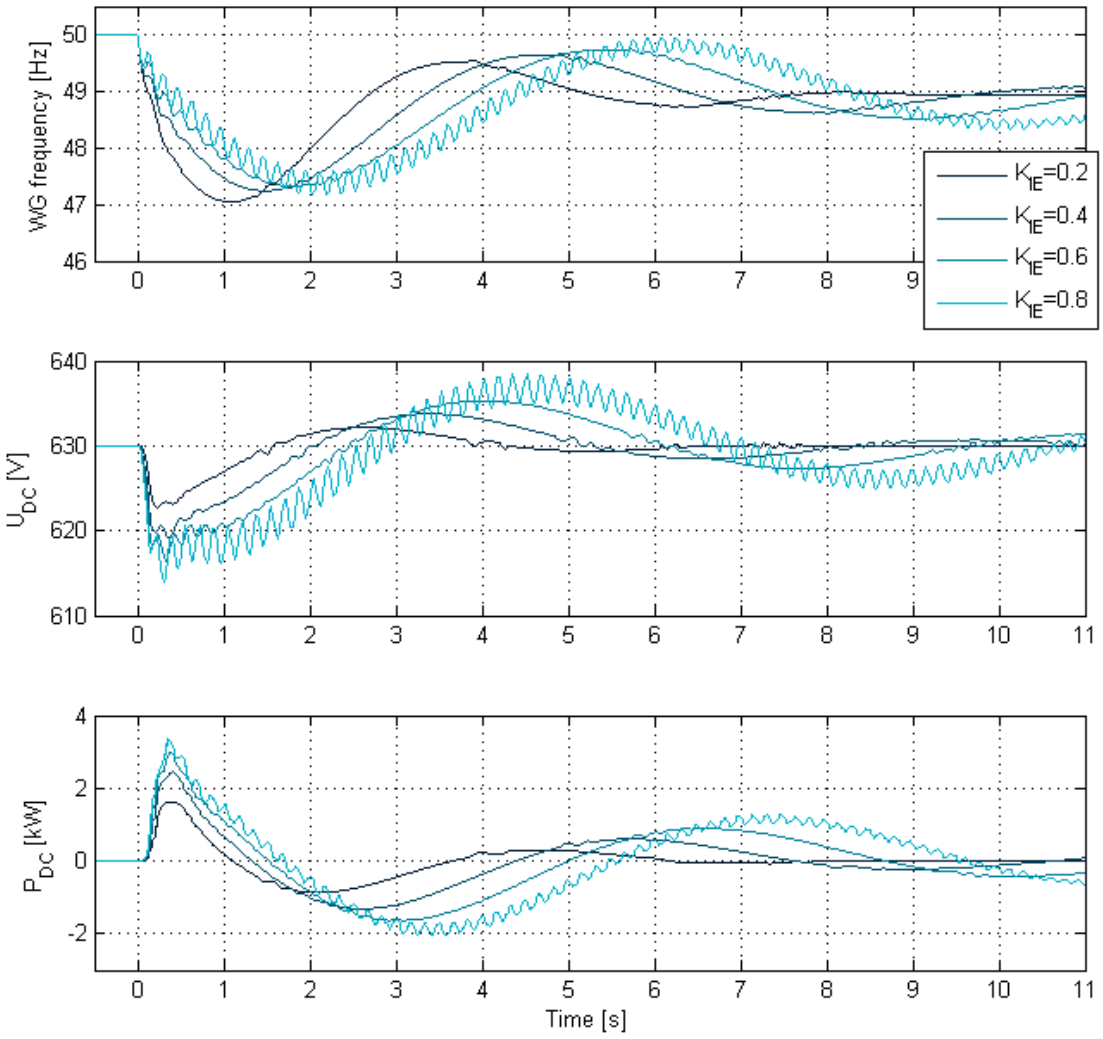

Figure 60: Simulation results showing the speed in the weak grid, the DC voltage and the power flowing in the DC cable following a step in load of $\Delta P_L = 0.25$ p.u. in the weak AC grid equivalent while increasing the inertia emulation gain K_{IE}. The experiments were performed with $K_V = 20$.

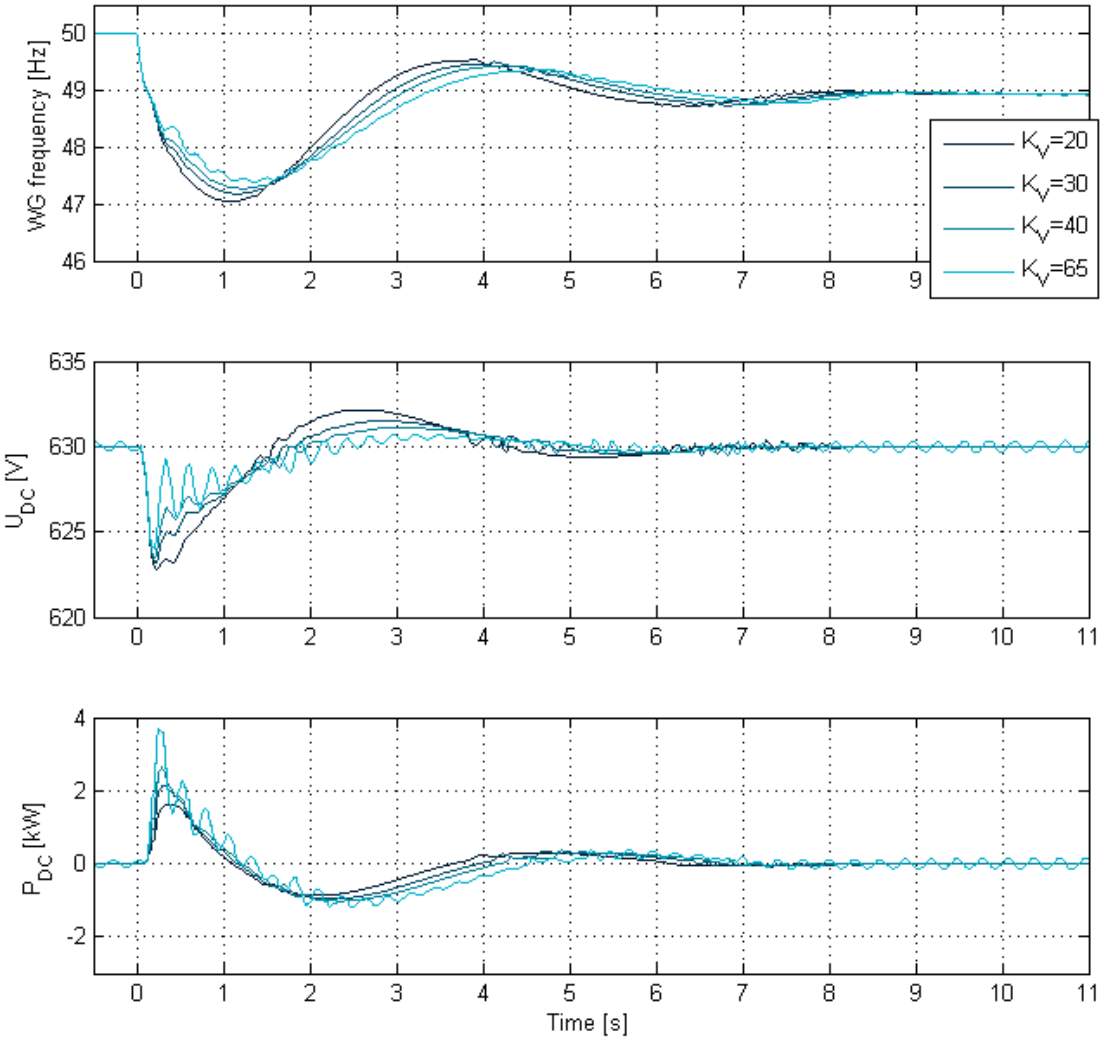

Figure 61: Simulation results showing the speed in the weak grid, the DC voltage and the power flowing in the DC cable following a step in load of $\Delta P_L = 0.25$ p.u. in the weak AC grid equivalent while increasing the voltage support gain K_V. The experiments were performed with $K_{IE} = 0.2$.

8.5 Simulation study: sensitivity of key parameters

The initial part of the frequency response in the weak grid is dependent on the total system inertia H_s and the load imbalance ΔP_{load}, as shown in Equation 3.2. When receiving inertial support from the wind farm, the wind farm equivalents' inertia H_{WT} becomes part of the total system inertia. Since both ΔP_{load} and H_{WT} are key parameters when regarding the improvement in the weak grid frequency response, a sensitivity analysis on these parameters was performed. The results are presented in the following sections.

8.5.1 Sensitivity analysis of the equivalent wind turbine inertia constant $\mathbf{H_{WT}}$

Figure 62 shows the simulation results of the weak grid frequency response as well as the DC voltage and wind turbine speed. As expected, increasing H_{WT} leads to an improvement in the frequency response. It can be seen that the change in wind turbine speed during the inertial support decreases when H_{WT} increases. The same characteristic was observed in 8.3 for an increasing wind turbine speed reference. Increasing H_{WT} or $\Delta\omega_{WT}$ results in the same behaviour because both measures increase the kinetic energy stored in the turbine. For a higher kinetic energy, the wind turbine speed will change less than for a lower amount of stored kinetic energy. This is explained in detail in Section 8.3.

8.5.2 Sensitivity analysis of the calculation of the step in load $\Delta\mathbf{P_L}$

Figure 63 shows simulation results of the WG frequency, DC voltage and wind turbine speed for different steps in load ΔP_{load}. It can be seen that the frequency response is very sensitive to the change in load. This is expected since the frequency derivative is proportional to ΔP_{load} as seen from Equation 3.2.

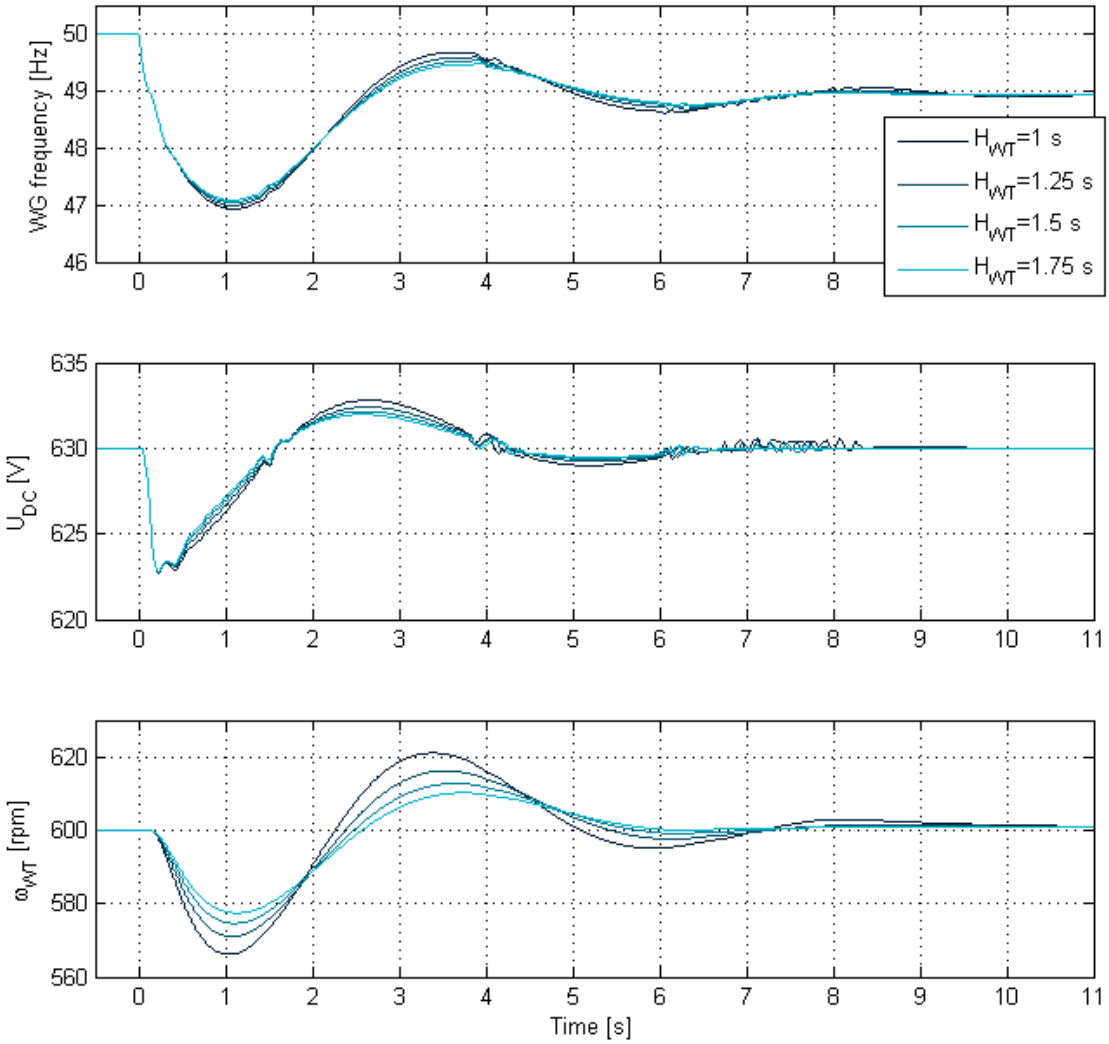

Figure 62: Simulation results showing the speed in the weak grid, the DC voltage and the wind turbine speed following a step in load of $\Delta P_L = 0.25$ p.u. in the weak AC grid equivalent for different values of the inertia of the wind farm equivalent. The experiments were performed with $K_{IE} = 0.2$ and $K_V = 20$.

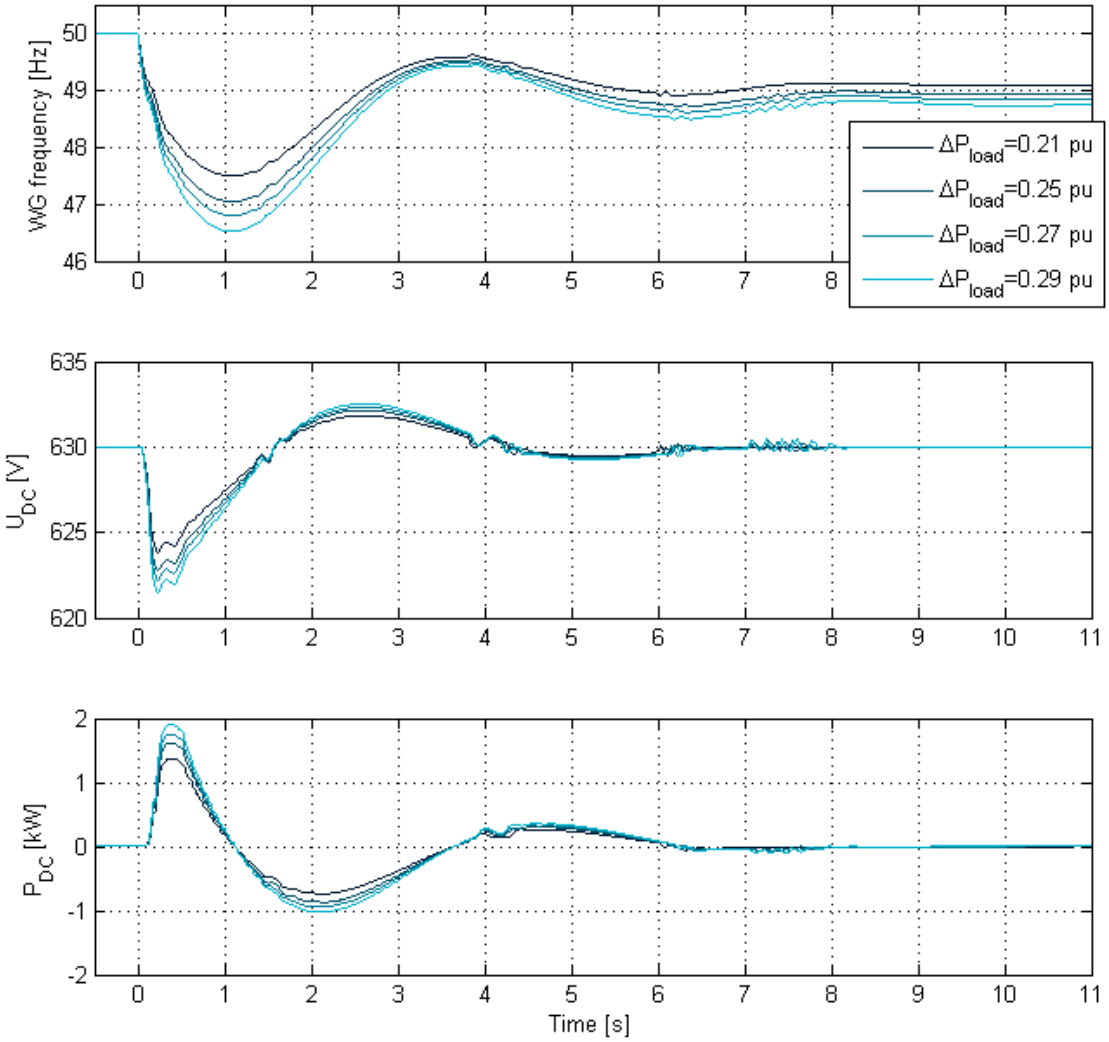

Figure 63: Simulation results showing the speed in the weak grid, the DC voltage and the power flowing in the DC cable for different steps in load $\Delta P_L = 0.25$ p.u. in the weak AC grid equivalent. The experiments were performed with $K_{IE} = 0.2$ and $K_V = 20$.

8.6 Discussion

The case studies conducted on the laboratory model show that the implemented inertia emulation and voltage support controls are performing as intended. By adjusting the gains K_{IE} and K_V, the amount of inertia support from the wind farm equivalent is varied and the resulting frequency response in the weak grid is investigated. The impact of the DC droop and wind turbine operational point is analysed and simulation results are included to investigate what brings the system towards instability. Also, sensitivity analyses of key parameters are made. This section discusses constraints related to the amount of inertial support possible to obtain from the wind farm equivalent and addresses the question; can the laboratory model represent a full scale system?

8.6.1 Inertial support constraints

The most obvious constraint is the amount of available kinetic energy from wind turbines. In a real system, variable speed wind turbines will operate according to an allowed speed decrease. This maximum speed decrease will determine the maximum amount of inertial support possible from the individual turbines. Another constraint is the current limits in all power electronic converters. If the system is operating at rated conditions when a load imbalance occurs in the weak grid, converter current limit may inhibit the transmission of the amount of power that is requested by the weak grid. Also regarding the converters, are the constrains related to the maximum decrease or increase in DC voltage. The minimum allowed DC-voltage is the physical rectifying limit, whereas the maximum allowed DC voltage is related to insulation in for instance the switches (IGBTs) and the DC cables. In most situations there are some available reserve capacity on the cables, and short term overloading will not damage it. However, the switches in the VSCs are sensitive to current overload.

Nevertheless, the main observation during the experiments on the laboratory set-up was that the main constraint to inertial support is the system stability. When adjusting the control system parameters in order to maximize the received inertial support, the system becomes unstable before any of the above-mentioned limits are violated. While this has shown to be the main constriction in the laboratory set-up it is not clear whether the situation will be the same in a real system. The following section discusses the main differences between the laboratory model and a full scale system.

8.6.2 Differences between the laboratory model and a full scale system

Regarding the weak grid equivalent, it can be seen from the results that the initial ROCOF and the nadir are significant. This is due to the small inertia in the system and the amount of load imbalance which is 25 % of the rating of the system. In addition, the generator speed control is made deliberately slow to worsen the frequency recovery period. Compared to Ireland which is considered to be one of the most fragile grids in Europe, the laboratory case has even lower inertia and higher ROCOF. Frequency dynamics and wind farm inertial support in Ireland has been demonstrated in [42]. In a real system larger inertia would give more time to react to changes in the frequency.

Regarding the wind farm equivalent, a major simplification is made through disregarding the internal wind farm AC grid as explained in 5.4.1. Including this step will have a negative impact on the performance due to time delays related with the additional control systems needed. Another simplification is to disregard the aerodynamic efficiency, i.e. the $C_p - \lambda$ characteristic. In a real turbine, the efficiency decreases when operating at a rotational speed differing from the optimal one. Hence, the energy needed to bring the turbine back to nominal speed in higher than the energy extracted as inertial support. However, this does not impact the first part of the frequency response. When designing the maximum allowable turbine speed decrease, it is important to consider its recovery period so that when the turbine accelerates after the inertial support, it does not cause a second dip in frequency with a larger nadir than the first one.

Regarding the DC network, the DC cables in the laboratory set-up are modelled as resistance, i.e. the the inductance and capacitance are neglected. This means that the dynamic behaviour of the cable in the laboratory is not the same as it would be in a real system. For instance, in case of a short circuit in the DC grid, the laboratory model would not be able to limit the short circuit current, whereas in a real system, the inductance in the cables would limit di/dt to some extent. However, the inductive time constant in a real DC cable is in the range of a few milliseconds which is too small to have a large impact on the inertial support.

9. Conclusion

This work contributes to research on primary frequency control services from VSC-HVDC connected wind farms. A laboratory model of a two terminal HVDC grid connecting a wind farm equivalent and a weak AC grid has been used. The overall goal has been to implement a control that enables the wind farm to contribute with inertial reserves during a load imbalance in the weak AC grid. The inertial support control on the weak grid connected converter relates changes in the system frequency to the DC voltage. The voltage support control on the wind farm connected converter relates changes in DC voltage to the wind turbine speed. A simulation model of the laboratory set-up was created for comparison purposes and for analysing the effect of changing key parameters. It was able to recreate the behaviour of the system to a large extent. Furthermore, the laboratory model is able to capture the most important characteristics of a real system.

The implemented inertia emulation control works as intended. The wind farm equivalent is able to contribute with inertial support during the occurrence of a load imbalance in the weak grid. In the best case the first frequency dip is reduced from 3.7 Hz to 2.5 Hz, which corresponds to an improvement of 48.2 % based on the steady-state frequency deviation. The first dip is also shifted in time with approximately 1.3 seconds, compared to base case. However, the system appeared close to its stability limit for the cases with best nadir improvement. The optimal control parameters is a trade-off between improvement in nadir and stability margins.

It was observed that the DC voltage droop limits the inertial response from the wind turbine since it counteracts changes in DC voltage. However, removing the DC droop made the system more oscillatory. It was found that since the DC droop does not only relate to the DC voltage, but also to the DC power, it provides damping to the system during transient events.

It was discovered that decreasing the DC voltage on the weak grid terminals as part of the inertial support control also triggered an inertial response from the DC grid itself. When the DC voltage decreases, the capacitances in the system release a certain amount of stored energy which also contributes to inertial support.

It was found that the main constraint to the amount of inertial support that is possible to obtain in the laboratory model is the stability of the system. Also, the performance of the controls is limited by significant time delays associated with implemented filters.

Further Work

9.1 Adding extra terminals in the HVDC grid

It was briefly mentioned in the introduction of the thesis, that the original intent was to have a three terminal HVDC network, similar to the system shown in Figure 64. Since this plan had to be revised, adding an extra terminal in the HVDC grid is proposed as further work. The challenge in having a three terminal system lies in achieving a coordinated response between the inertial emulation control and the droop control on the third terminal.

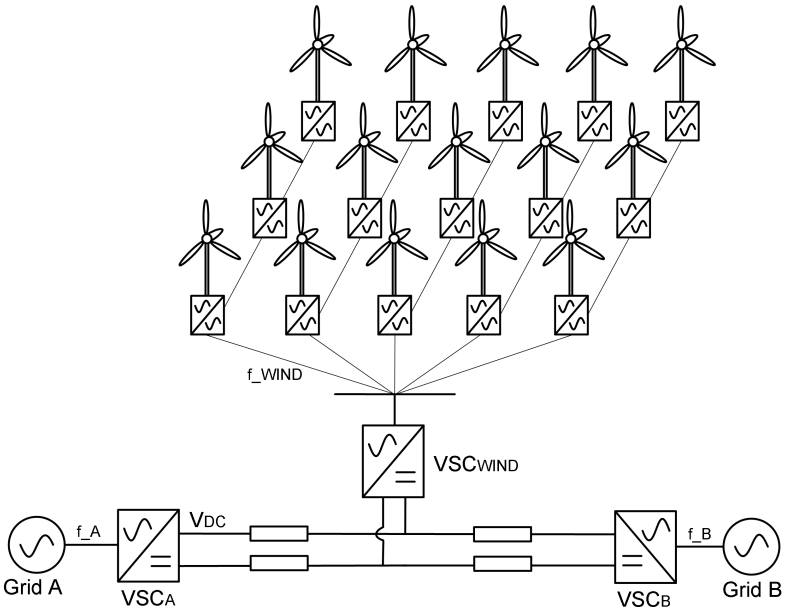

Figure 64: An example of a multi-terminal HVDC grid composed of two conventional AC grids (Grid A and Grid B) and an offshore wind power plant.

9.2 Include turbine frequency converter in the wind farm equivalent

A more realistic model of the wind farm equivalent can be achieved by including a fully controllable frequency converter, also called a back to back converter (B2B) to represent the wind turbine converter, see Figure 64. Since the B2B separates the rotational speed of the turbine from the frequency in the collection grid, implementing extra controls is necessary to obtain an inertial response. This was discussed in Section 3.3. Adding a turbine converter between the HVDC converter and the wind turbine generator is proposed as further work. It is highlighted that such a converter is already available in the SINTEF/NTNU laboratory.

9.3 Improve measurements and optimize proposed control system

A challenge in the practical work was to obtain an accurate frequency measurement in the weak grid equivalent. See section 7.6 for a discussion on this topic. It is already planned to upgrade the laboratory FPGA converter controls to have a significant higher resolution, and this can be utilized in further work. As mentioned before, the DC-voltage controllers operate with 1 V resolution in the voltage measurement. A higher resolution would reduce noise and oscillations in the DC-grid, which in turn may improve the stability of the entire system. It has been pointed out that Labview/CAN-bus is not the optimal interface for control of the outer loops in the system. It is recommended that e.g. a real-time simulator is included in further work, in order to reduce the sampling time of the control loops. The main advantage of reducing sampling time and improving measurements is the possibility to reduce filter and increase bandwidth of controllers, which in turn will lead to a faster inertial response without compromising the system stability.

Finally, the key control system parameters were mostly found through comparing results from a large number of combinations. A more systematic approach using e.g. state-space and eigenvalue techniques can be helpful in this respect. This has particular relevance if the objective of further work is to achieve the optimal improvement in the weak grid frequency response.

9.4 Impact of proposed controls during faults and abnormal operating conditions

Although fault analysis was out of the scope of this work, some thoughts were made on how the implemented controls on the HVDC converters may influence the system during AC and DC faults. For any control system, it is important that the design accounts for even the most extreme operational scenarios that may occur in a power system. In order to contain the system during a fault, it is important that the implemented controls do not drive the system further towards instability. The outer controls that are discussed in this thesis should be pacified during faults so that they are not stand in the way of protection equipment or contributes to harming the system in any way.

Bibliography

[1] J. Aho, A. Buckspan, J. Laks, Y. Jeong, F. Dunne, L. Pao, P. Fleming, M. Charchfield, and K. Johnson. Tutorial of wind turbine control for supporting grid frequency through active power control. In *NREL*, 2012.

[2] B. Silva, C.L. Moreira, Seca L., Y. Phulpin, and J. A. Peas Lopes. Provision of inertial and primary frequency control services using offshore multiterminal hvdc networks. *Sustainable Energy, IEEE Transactions on*, 3(4):800–808, 2012.

[3] H. Støylen. Laboratory demonstration of an offshore grid in the north sea with dc droop control. Specialization Project, 2013.

[4] F. Blaabjerg, Z. Chen, and K. Baekhoej. Power electronics as efficient inertface in dispersed power generation systems. *IEEE Transactions on Power Electronics*, 19, 2004.

[5] A. D. Hansen. Evaluation of power control with different elelectric and control concept of wind farm. Technical report, Risø National Laboratory for Sustainable Energy, 2010.

[6] Pieter Tielens and Dirk Van Hertem. Grid inertia and frequency control in power systems with high penetration of renewables. In *Electrical Energy Computer Architectures*. KU LEUVEN, 2012.

[7] Lorenzo Zeni, Andreas Jakob Rudolph, Janus Münster-Swendsen, Ioannis Margaris, Anca Daniela Hansen, and Poul Soerensen. Virtual inertia for variable speed wind turbines. *Wind Energy*, 16(8):1225–1239, 2013.

[8] Johan Morren, Jan Pierik, and Sjoerd W.H. de Haan. Inertial response of variable speed wind turbines. *Electric Power Systems Research*, 76(11):980 – 987, 2006.

[9] Xue Yingcheng and Tai Nengling. Review of contribution to frequency control through variable speed wind turbine. *Renewable Energy*, 36(6):1671 – 1677, 2011.

[10] Z. Miao, L. Fan, D. Osborn, and S. Yuvarajan. Wind farms with hvdc delivery in inertial response and primary frequency control. *IEEE Transactions on Energy Conversion*, 25, 2010.

[11] T.M. Haileselassie, R.E. Torres-Olguin, T.K. Vrana, K. Uhlen, and T. Undeland. Main grid frequency support strategy for vsc-hvdc connected wind farms with variable speed wind turbines. In *PowerTech, 2011 IEEE Trondheim*, pages 1–6, 2011.

[12] J. M. Mauricio, A. Marano, A. Gómez-Expósito, and J. L. M Ramos. Frequency regulation contribution through wind energy conversion systems. *IEEE Transactions on Power Systems*, 24, 2009.

[13] EURELECTRIC. Ancillary services: Unbundling electricity products - an emerging market. Technical report, Thermal Working Group, 2004.

[14] A. Bangar and V. Hamidi. Control strategy requirements for connection of offshore windfarms using vsc-hvdc for frequency control. In *AC and DC Power Transmission (ACDC 2012), 10th IET International Conference on*, pages 1–6, 2012.

[15] Yannick Phulpin and Damien Ernst. Ancillary services and operation of multi-terminal hvdc grids. In *Proceedings of the International Workshop on Transmission Networks for Offshore Wind Power*, 2011.

[16] Hannele Holttinen, Juha Kiviluoma, Nicolaos Cutululis, Andrej Gubina, Andrew Keane, and Frans Van Hulle. Ancillary services: technical specifications, system needs and costs. Technical report, REserviceS, 2012.

[17] ENTSO-E. Draft network code on high voltage direct current connections and dc-connected power park modules, 2013.

[18] ENTSO-E. Network code on load-frequency control and reserves, 2013.

[19] ETSO. Balance management harmonisation and integration 4th report, 2007.

[20] ENTSO-E. Entso-e operational handbook, 2014.

[21] James R. Bumby Jan Machowski, Janusz W. Bialek. *Power System Dynamics Stability and Control*. John Wiley & Sons, Ltd., 2nd edition, 2012.

[22] N.W. Miller, K. Clark, and M. Shao. Frequency responsive wind plant controls: Impacts on grid performance. In *Power and Energy Society General Meeting, 2011 IEEE*, pages 1–8, 2011.

[23] J. F. Manwell, J. G. McGowan, and A. L. Rogers. *Wind Energy Explained*. John Wiley & Sons, Ltd., 2008.

[24] E. Muljadi, V. Gevorgian, M. Singh, and S. Santoso. Understanding inertial and frequency response of wind power plants. 2012.

[25] Temesgen Mulugeta Haileselassie. *Control, Dynamics and Operation of Multi-terminal VSC-HVDC Transmission Systems*. PhD thesis, NTNU, December 2012.

[26] Statnett. Projects. http://www.statnett.no/en/Projects/, [Accessed 2014-05-26], 2014.

[27] N. Miller, K. Clark, and M. Shao. Impact of frequency responsive wind plant control on grid performance. In *9th International Workshop on Large-Scale Integration of Wind Power into Power Systems*, 2010.

[28] Ned Mohan. *Advanced Electric Drives*. MNPERE, 2001.

[29] Dirk Van Hertem and Mehrdad Ghandhari. Multi-terminal {VSC} {HVDC} for the european supergrid: Obstacles. *Renewable and Sustainable Energy Reviews*, 14(9):3156 – 3163, 2010.

[30] Til Kristian Vrana. *System Design and Balancing Control of the North Sea Super Grid*. PhD thesis, NTNU, 2013.

[31] Til Kristian Vrana, Jef Beerten, Ronnie Belmans, and Olav Bjarte Fosso. A classification of dc node voltage control methods for hvdc grids. *Electric Power Systems Research*, 103(0):137 – 144, 2013.

[32] S. D'Arco and J.A. Suul. Generalized implementations of piecewise linear control characteristics for multiterminal hvdc. 2011.

[33] Kjell Ljøkelsøy. Control system for a three-phase grid connected converter (memo). Technical report, SINTEF Energy Research, 2013.

[34] SINTEF. Renewable Energy System Laboratory. http://www.sintef.no/home/SINTEF-Energy-Research/Laboratory-Services-/Renewable-Energy-System-Laboratory/, [Accessed 2014-05-21], 2014.

[35] ABB. Low and high voltage processperformace motors. Technical report, ABB LV Motors, 2006.

[36] Kjell Ljøkelsøy. 60 kva laboratory converter unit, documentation (memo). Technical report, SINTEF Energy Research, 2010.

[37] Kalle Teearu. Laboratory testing of multi-terminal vsc-hvdc. Master's thesis, NTNU, 2013.

[38] Astrid Petterteig. Distribution network laboratory model (memo). Technical report, SINTEF Energy Research, 2011.

[39] Astrid Petterteig. Specification of equiptment for the small hydro generator model for the sintef/ntnu renewable energy laboratory (memo). Technical report, SINTEF Energy Research, 2008.

[40] Astrid Petterteig. General description of mv distribution network model for the sintef/ntnu renewable eenrgy laboratory (memo). Technical report, SINTEF Energy Research, 2008.

[41] Astrid Petterteig. Specification of the hv/mv substation model for the sintef/ntnu renewable energy laboratory (memo). Technical report, SINTEF Energy Research, 2008.

[42] G. Lalor, J. Ritchie, Rourke S., D. Flynn, and M. O'Malley. Dynamic frequency control with increasing wind generation. *IEEE Power Engineering Society General Meeting Proceedings*, 2, 2004.

10. Appendix

10.1 All results from inertia emulation base case

The inertia emulation base case uses $K_{IE} = 0.2$ and $K_V = 20$.

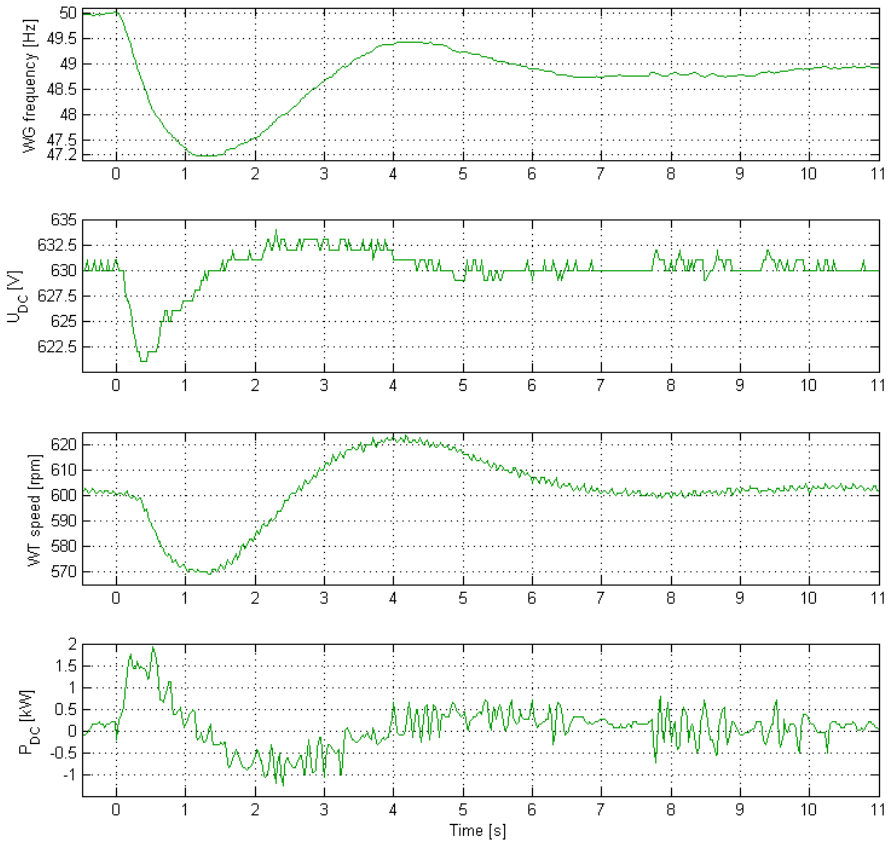

Figure 65: Laboratory measurements a step in load of $\Delta P_L = 0.25$ p.u. in the weak AC grid equivalent. The inertia emulation base case uses $K_{IE} = 0.2$ and $K_V = 20$.

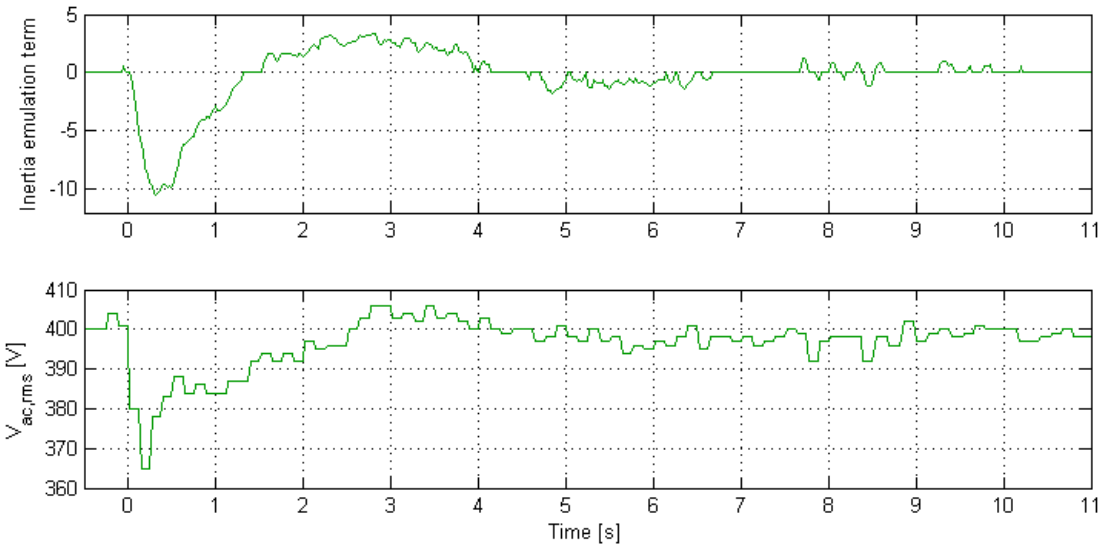

Figure 66: Laboratory measurements a step in load of $\Delta P_L = 0.25$ p.u. in the weak AC grid equivalent. The inertia emulation base case uses $K_{IE} = 0.2$ and $K_V = 20$.

10.2 The effect of the wind turbine operating point - simulation results

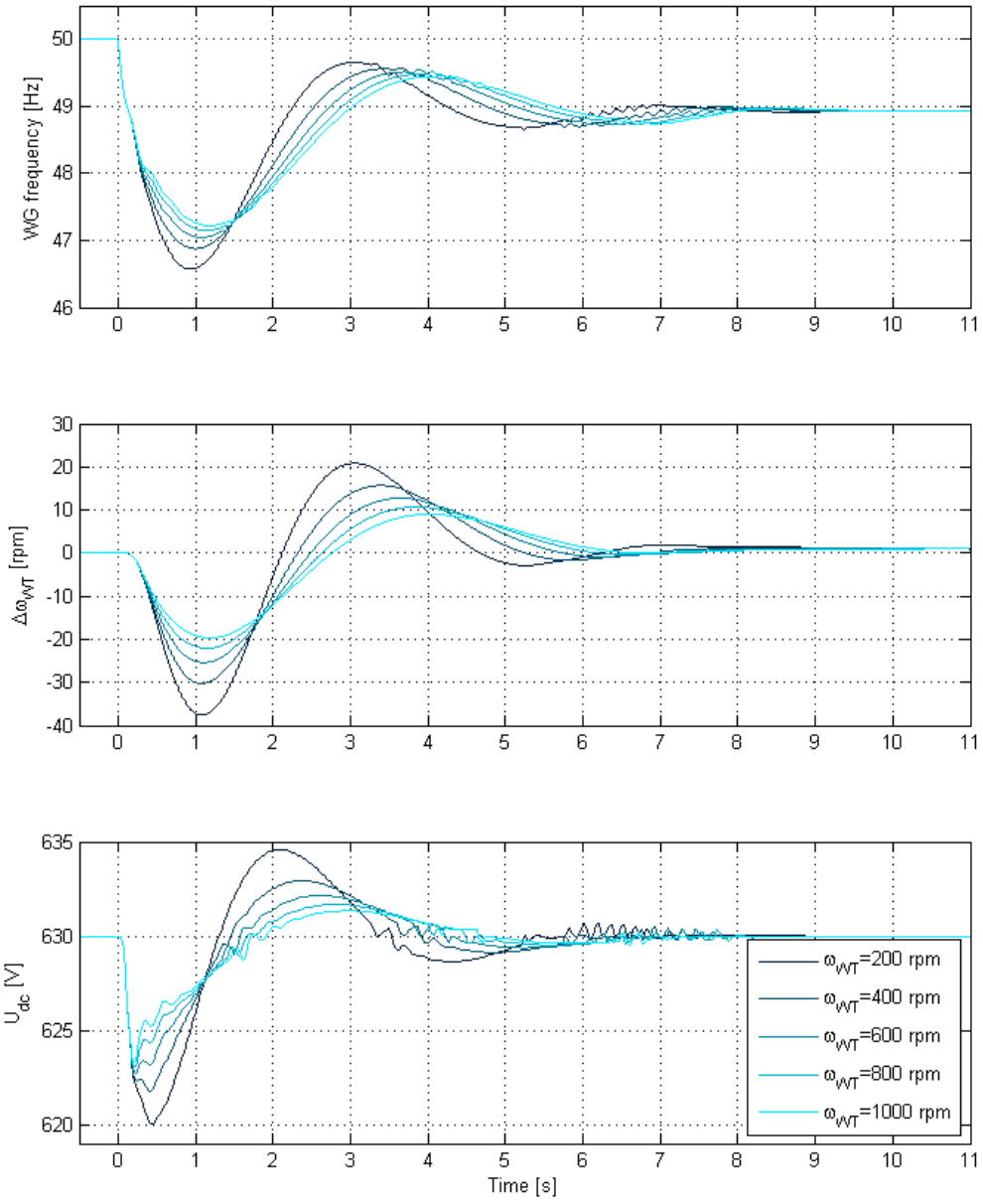

Figure 67: Simulation results showing effect of varying the wind turbine operation point during a load imbalance of $\Delta P_L = 0.25$ p.u. in the weak AC grid equivalent. The inertia emulation base case uses $K_{IE} = 0.2$ and $K_V = 20$.

10.3 The laboratory site

Figure 68: The laboratory site.

10.4 Siemens frequency converter settings

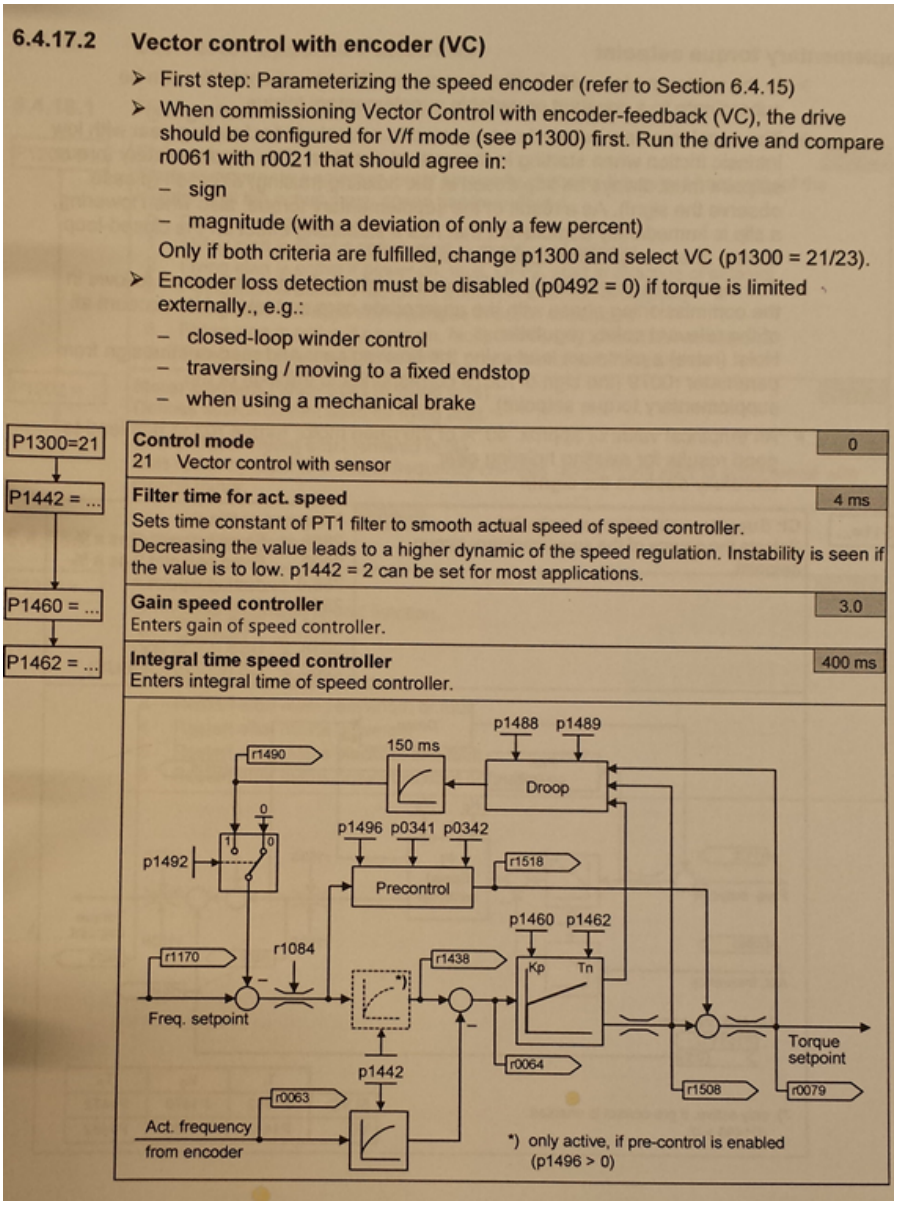

Figure 69: Vector control with encoder block diagram from "Kretsskjema-perm" (Frekvensomformer, page 53).

Figure 70: Micromaster code and setting for speed control gain K_p

Figure 71: Micromaster code and setting for speed control integrator time T_i

Figure 72: Micromaster code and setting for frequency droop control

10.5 Generator Protection Unit: AVR settings

Figure 73: Generator Protection Unit: AVR settings

10.6 Labview Control Front Panel

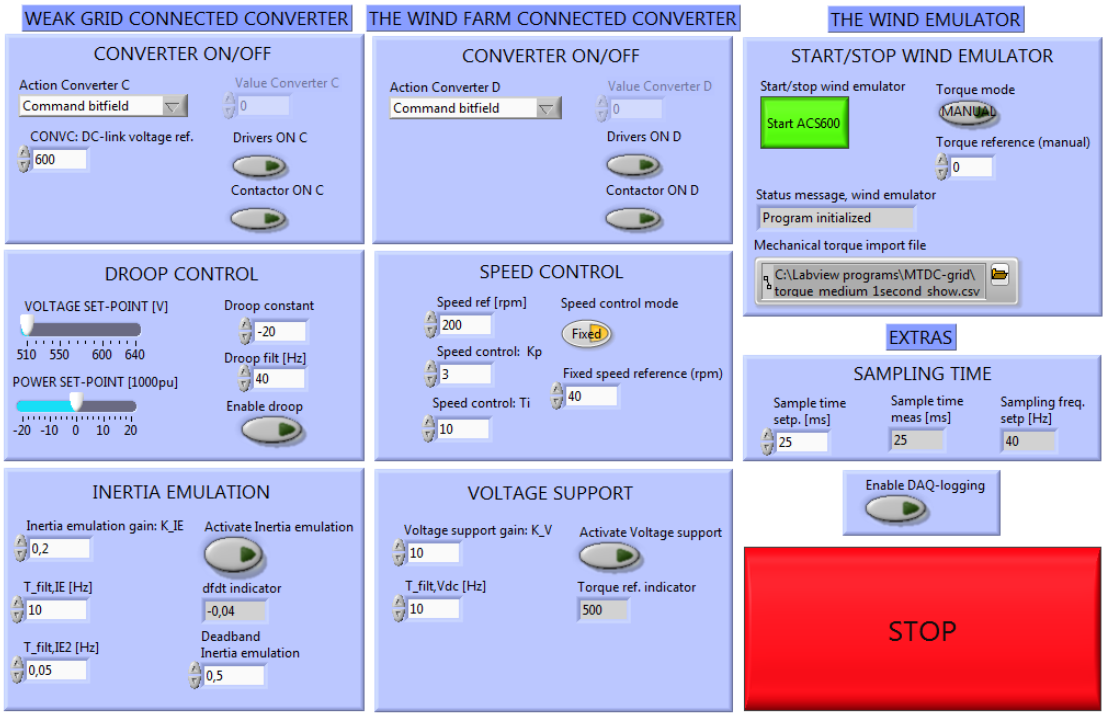

Figure 74: Screen shot of the control panel in Labview.

10.7 Labview Control Screen-shots

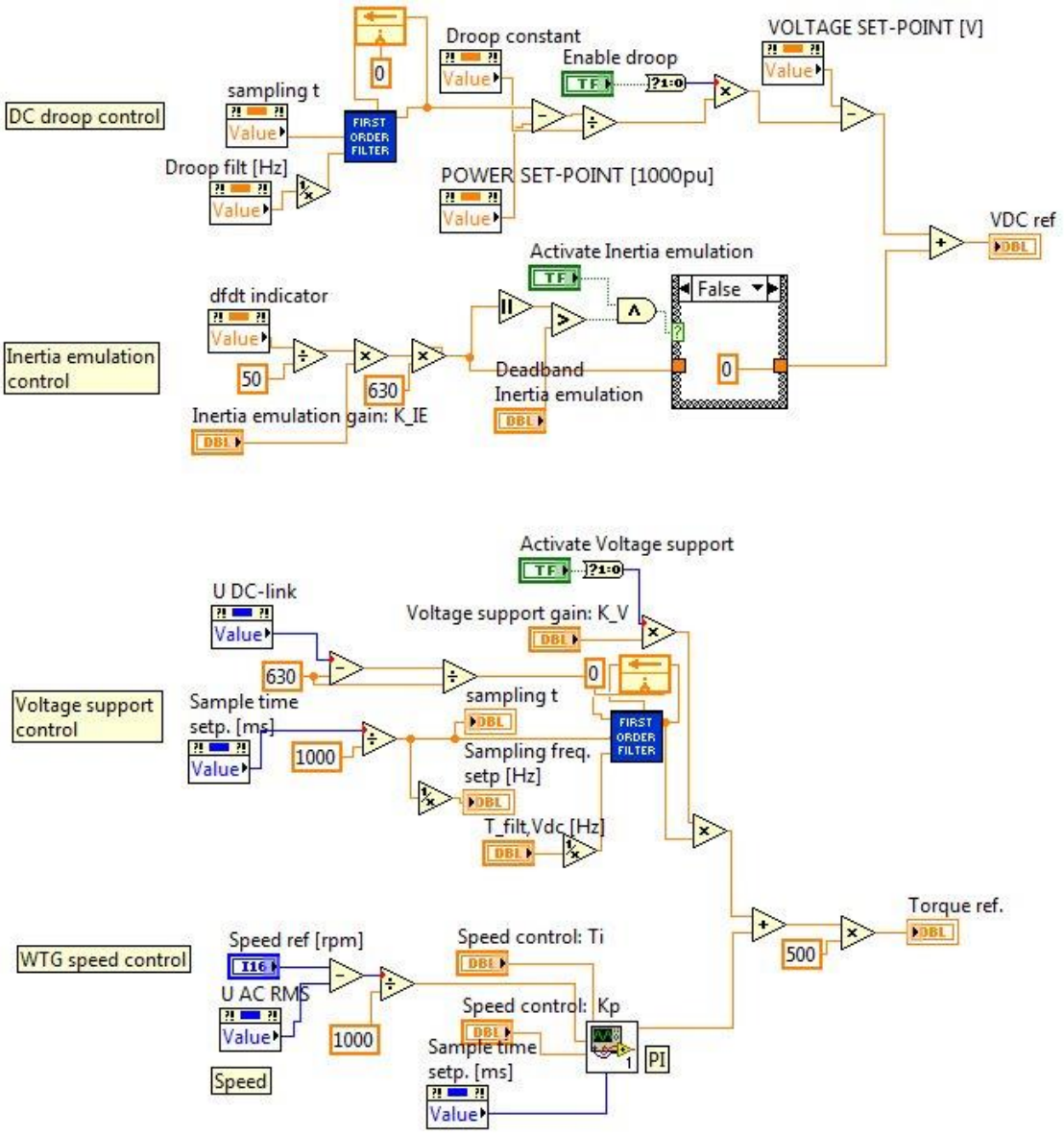

Figure 75: Outer controls implemented in Labview. The DC droop control and Inertia emulation control calculates the DC voltage reference on the weak grid connected converter. The voltage support control and wind turbine speed control calculates the wind turbine generator torque reference on the wind farm connected converter.

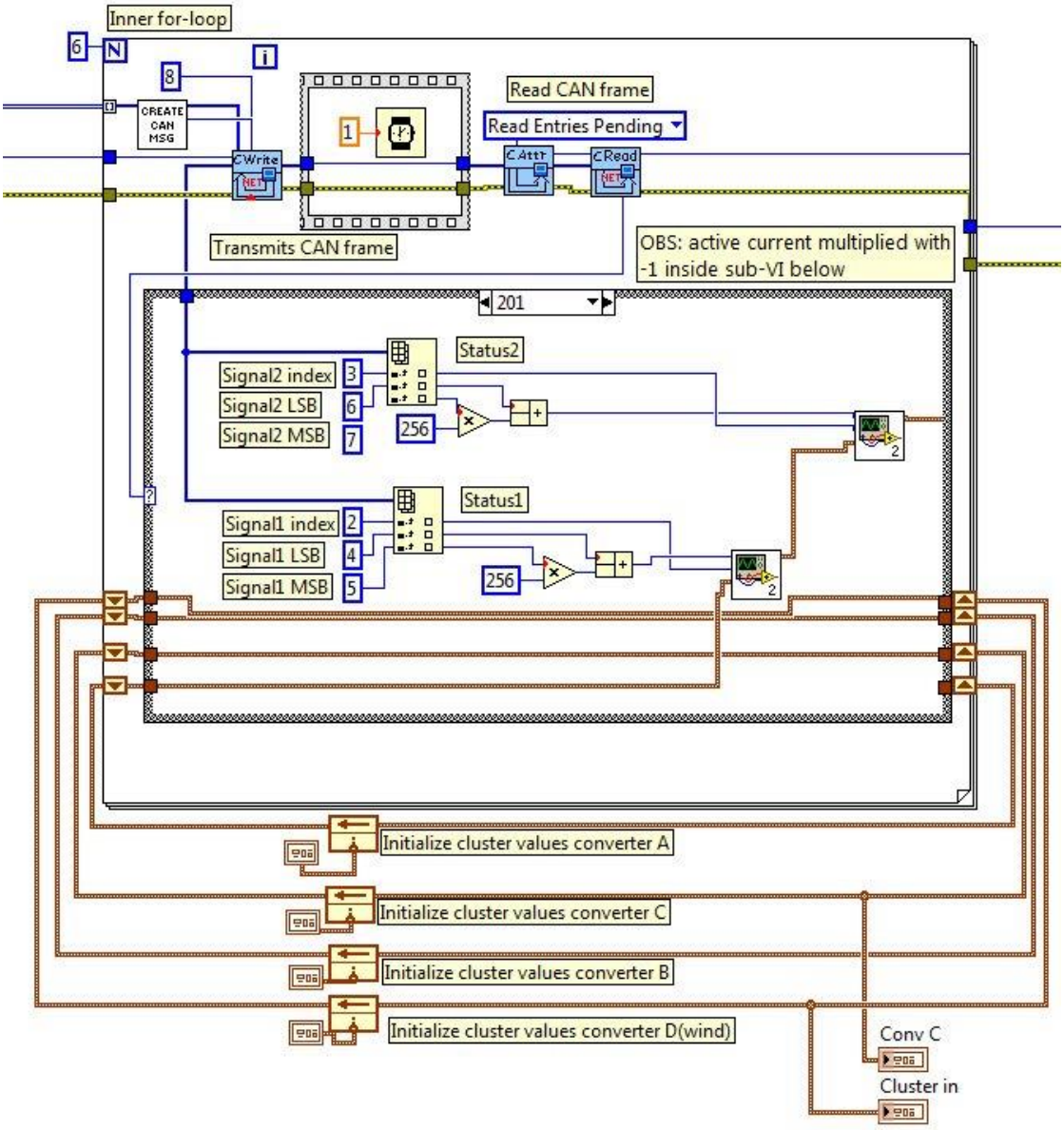

Figure 76: Inner for-loop in Labview control.

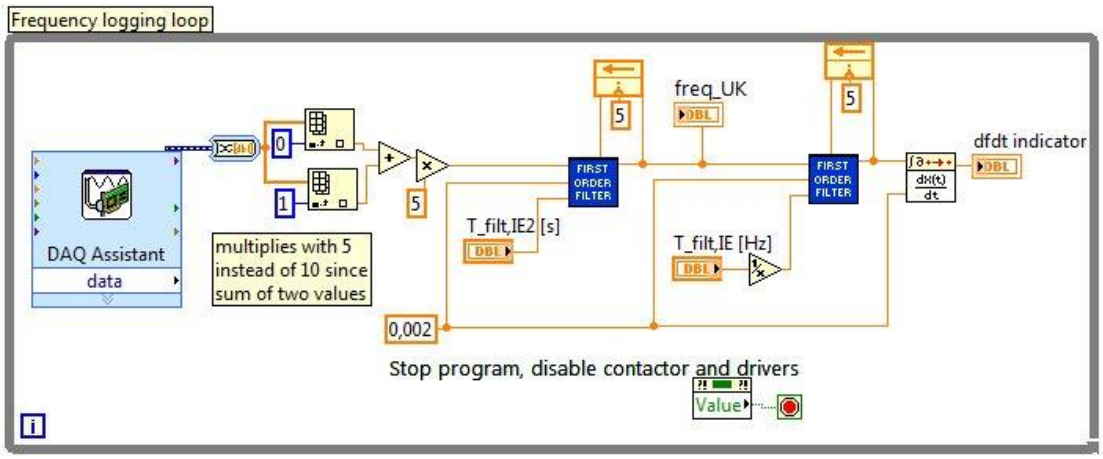

Figure 77: Frequency logging loop in Labview program.

10.8 FPGA control block diagram

A block diagram of the DC-link voltage controller is shown in Figure 78. This is the DC-link voltage controller embedded in the FPGA control card by the designer of the converters, and is explained in detail in [33]. The control created in Labview will modify the DC voltage reference value that is input in the block diagram shown below. "Reference" and "Actual value" refers to the DC-voltage reference and measurement. The value K_{droop} is set to zero since the droop term is implemented in the Labview program. The input "offset" is also not used, i.e. set to zero. The resulting quantity "Out" represents the active current reference, which is sent to the current control block.

Regarding the wind farm equivalent, it is implemented as a converter connected directly to an induction machine motor/generator-set. The "motordrive" control mode is therefore used. The FPGA converter control is controlling the torque and magnetic flux in the generator. The torque reference in obtained from a speed control realized in Labview and the voltage support control. The calculated reference is then through a CAN-bus.

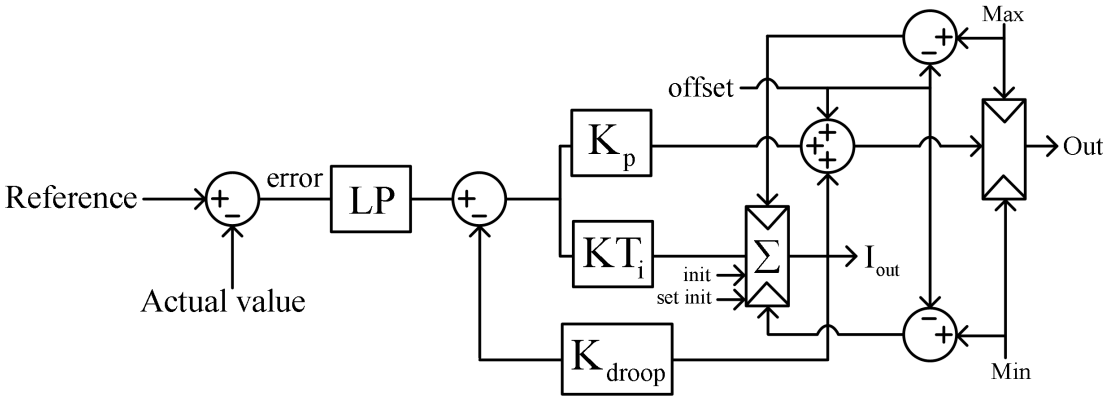

Figure 78: A block diagram of the DC-link voltage controller embedded in the FPGA control card (block diagram taken from [33]).

10.9 Publication of results

2014 Ninth International Conference on Ecological Vehicles and Renewable Energies (EVER)

Laboratory Demonstration of an Offshore Grid in the North Sea with DC Droop Control

Hanne Støylen
Kjetil Uhlen
Norwegian University of Science and Technology
Trondheim, NORWAY
Email: hanne.stoylen@gmail.com

Atle Rygg Årdal
SINTEF Energy Research
Trondheim, NORWAY

Kamran Sharifabadi
Statoil ASA
Oslo, NORWAY

***Abstract*—The system studied in this article is a multi-terminal HVDC (MTDC) network composed by four voltage-source converter terminals. It is intended to be a model of the future "super-grid" in the North Sea, where Norway, Germany and the UK are interconnected together with offshore wind farms on the east coast of England. The main challenges related with multi-terminal HVDC grids are market and regulatory issues, control and coordination of the grid, and protection and circuit-breakers. This article focuses on the technical challenges, especially those in relation with DC voltage control and power flow balancing. Several studies have proposed different methods for controlling the DC voltage in MTDC grids. This article uses a DC voltage droop control scheme. The system is analysed by means of simulations and experimentally in a down-scaled laboratory model with ratings in the range of 60 kVA. In order to evaluate the robustness of the droop-control strategy, several large disturbances are emulated: abrupt variation in wind production, sudden change in droop line set-points and loss of two converter terminals during full wind production. Finally, the similarities and differences between the experimental set-up and a real system are discussed.**

I. Introduction

In the future it is foreseen that there will exist a "Super-grid" that interconnects European countries' power systems and the regions around Europe's borders. The objective of such a transmission framework is to facilitate large-scale integration of renewable energy and to expand the European power market. An offshore grid in the North Sea, called the North Sea Super-grid, is proposed as one of the building blocks in the European Super-grid [1]. It received special attention in 2008 when a North Sea Offshore Grid was proposed by the European Commission and identified as one of the six priority energy infrastructure actions published in [2].

It is widely recognized that for long-distance bulk power transmission in the context of an offshore North Sea grid, HVDC transmission is favourable to AC transmission. For overhead lines the break-even distance between AC and DC is around 600 km, whereas for cable based solutions used for offshore transmission, the break-even distance is in the range of 50-100 km [3]. Furthermore, an techno-economic analysis performed in [4] showed that there can be a preference for adopting a meshed approach to grid design.

Regarding the converter technologies, there are mainly two types used in HVDC: Line Commutated Converters (LCC) and Voltage Source Converters (VSC). To change the DC flow in LCC technology, the voltage must be reversed. This leads to several challenges, for instance XLPE cables cannot be used as they do not tolerate voltage reversal. The VSC on the other hand can change the power flow through reversal of current direction. Thus, the nature of the VSC may be more suitable for a large, meshed DC grid.

One of the major stumbling blocks to the vision of a HVDC grid in the North Sea is the inability to break DC fault currents. Most of the HVDC topologies that exist today are used for point-to-point transmission, and fault scenarios are handled by disconnection the entire HVDC cable by activating AC switchgear and de-energizing the HVDC converter and the HVDC link [5]. In case of a meshed grid, fault handling in this manner would not be preferred as a single fault would lead to disconnection the entire DC grid. However, in late 2012, ABB announced the development of a "Hybrid HVDC breaker" [6]. This is a vital missing link which might boost the development of HVDC grids in the years to come.

Another challenge regarding multi-terminal HVDC grids is the ability to achieve precise power control. Precise and automated control of power enables possibilities for power balancing between countries. Also, the full potential of wind energy as a balancing power against other mainland-renewable sources, such as solar and hydro power, can be exploited by having the opportunity to control the power without the need for manual actions. Previous works [3][7][8] have demonstrated robust control strategies through numeric simulations. So far, there has been little focus on practical implementation. This report aims to implement a power and voltage control in a down-scaled laboratory model of a four-terminal VSC HVDC grid that ensures stable system operation.

It should be emphasized that this article is limited to primary control, i.e. secondary control actions, like making sure that a certain amount of power is transferred over a cross-section in the system, are not considered part of this work. Further, this article does not aim to study harmonics from power electronic switching or fast transients in voltage and current. Rather, it seeks to investigate phenomena in a larger time-span, related to the fundamental frequency voltage and current components. The objective of the control will be to ensure that the node voltages stay within their design limits. A well-controlled DC voltage is a key factor in ensuring stable operation of a MTDC grid, since it makes it possible to obtain power balance between the interconnected nodes [9].

II. State-of-the-art Control Strategies for Multi-Terminal HVDC-grids (MTDC)

The VSC is flexible and can offer a wide range of control objectives. Therefore, in a system made up of several terminals using VSC's, there are several possibilities regarding the control strategy. The first step before developing a control strategy for MTDC grids, is to define the technical requirements and specifications which should apply for the MTDC system. The most important control requirements for the MTDC system in the North Sea are assumed to be:

> The node voltages should be kept within their steady state limits.
>
> The system should be able to withstand unplanned events causing short-lasting or longer-lasting disturbances in voltage or power.
>
> The primary control should not rely on communication between terminals.
>
> The system should be flexible towards integration of new terminals.

It is possible to control the DC voltage based on current or power feedback. The current based control will use a I-V characteristic to control the voltage, whereas the power based control will use a P-V characteristic. This article studies power based state-of-the-art controls, but the same principles apply for control strategies that are current-based [3].

a) Master-Slave control: is an extension of the conventional point-to-point control where one terminal controls the DC voltage and the other controls the power flow. This is also known as the slack bus approach. In master-slave control one terminal is responsible for maintaining the DC voltage (master-node/slack bus) and the other terminals are defined to be constant power nodes (slave-nodes) [3]. Graphs showing the relation between voltage and power for the master-node and slave-nodes are shown in the two top graphs in Figure 1. A disadvantage with this type of control is that the master-node may be subjected to large strains, since it is responsible for handling all power deviations. Also, the system is entirely dependent on the master-node to maintain the DC voltage which does not comply with the the N-1 criterion.

b) Voltage-Margin control: is a modified version of the master-slave control where the constant power and constant voltage characteristics are combined. The slave-nodes are assigned a constant power region for a given voltage range and a constant voltage for any voltage outside this range [3][9]. The relation between voltage and power for the slave-nodes is given in the leftmost middle graph in Figure 1. However, in the normal operation region, it is still the master-node that is responsible for balancing the power.

c) Voltage-Droop control: is based on the philosophy of having distributed voltage control in the MTDC system. Each terminal is assigned a linear relationship between its DC voltage and the power flowing through its terminals, see the rightmost middle graph in Figure 1. This way, the terminals share the task of maintaining the system voltage as well as the duty of instantaneous power balancing in the power grid [3]. How large share each terminal contributes with as a balancing unit depends on the droop constant, which is the slope of the droop-line. The droop control does not rely on fast communication between the terminals. Neither is the system dependent on one particular node, since all nodes are active in maintaining the voltage.

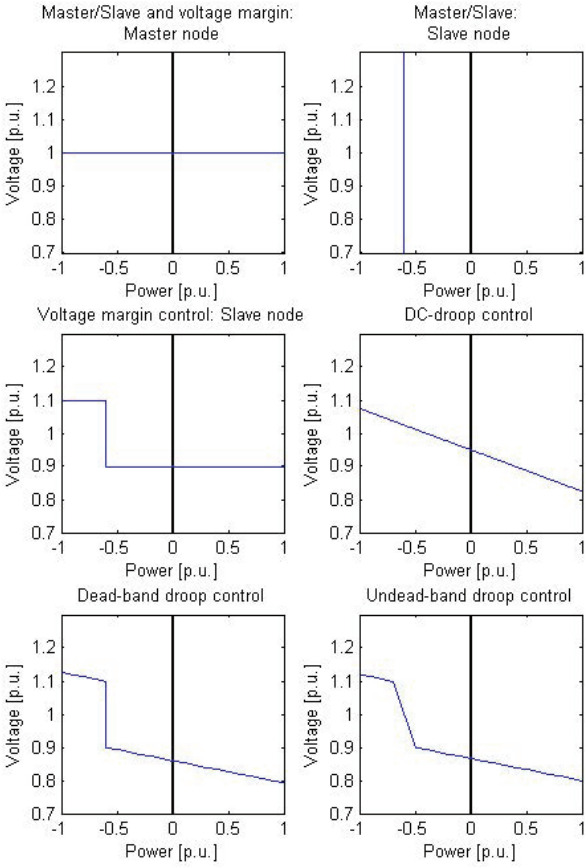

Figure 1. Power based voltage control methods in a MTDC network. In this work, negative power means that power flows from the DC side of the converter to the AC side of the converter, i.e. the converter is in inverter mode. The figures only show the relation between voltage and power for one terminal. In a system with two or more terminals the operating point will be in the equilibrium point where power balance is achieved in the system.

d) Dead-band and undead-band droop control: are combinations of the voltage margin and voltage droop control strategies. The principles are shown in the two bottom graphs in Figure 1. For the dead-band droop control the terminal is a constant power node for a given voltage range but for any voltage outside this range a droop is given. For the undead-band droop control the relation between voltage and power is always linear, but the droop constant differs for normal and disturbed operation [9].

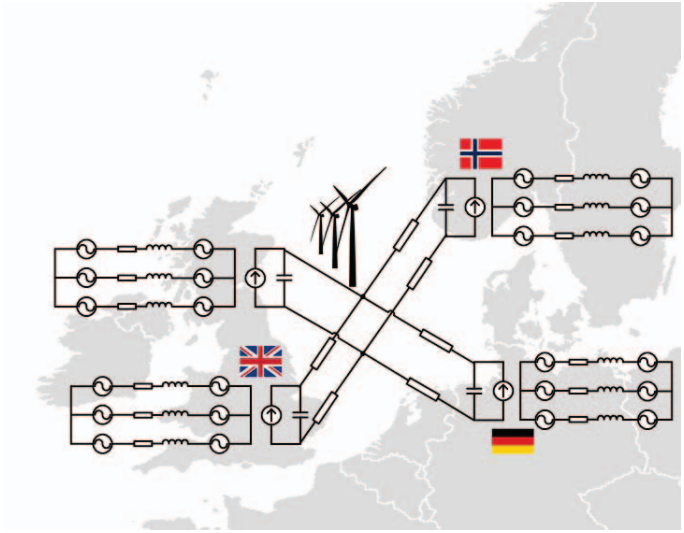

Figure 2. A circuit diagram showing the system as it is implemented in Matlab/Simulink. A background map is included to illustrate the placement of the converter-terminals.

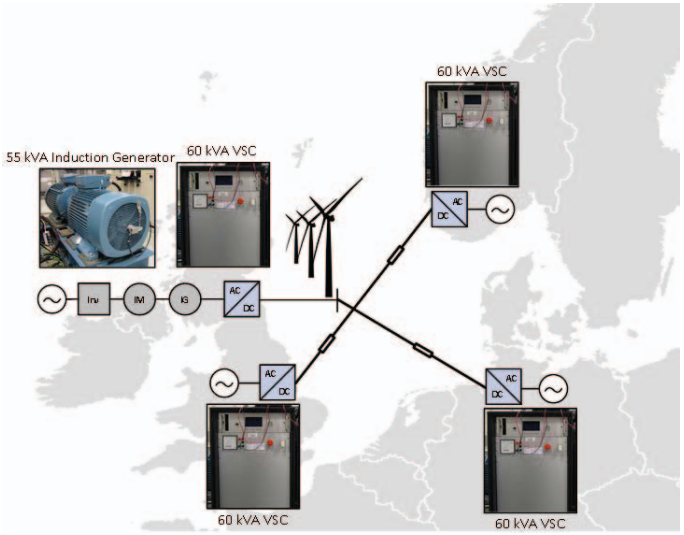

Figure 3. A principal sketch showing what components are used to create the laboratory set-up of the offshore HVDC grid. The wind-node converter is located offshore at the grid mid-point.

III. The Simulation Model

Figure 2 shows a sketch of the system as it is modelled in Matlab/Simulink. The system consists of four nodes representing Norway, Germany, UK and a wind farm on the east coast of England.

The VSCs are modelled by a time-averaged approach in the same way as in [3]. This is achieved by considering each converter terminal as a controllable voltage source connected to an AC transmission network. The AC transmission network is modelled by means of its thevenin equivalent, i.e. the voltage sources are connected through a series reactor and resistance. See section V for more details on converter modelling.

The converters are connected together at their DC sides in a star-configuration. Since this report does not focus on fast transient phenomena associated with cable dynamics, the capacitance and inductance of the DC cables are neglected. Thus, the HVDC cables are modelled as resistances. However, the capacitive filter of each converter is included. It is assumed that the wind farm is interconnected with the rest of the DC system close to the common mid-point connection. Hence, the DC cable resistance is assumed to be zero between the wind farm and the connection point.

IV. The Laboratory Set-Up

Figure 3 shows the configuration of the down-scaled laboratory model of the four-terminal HVDC grid. Pictures of important components are also included. A similar implementation of a MTDC grid has been analysed in [10]. The current set-up has been implemented in the SINTEF/NTNU Renewable Energy Systems Laboratory [11] and consists of:

Four 60 kVA voltage-source converters

A 55 kVA motor-generator set used as wind farm equivalent

Motor-drive for the 55 kVA motor used to emulate wind power profiles

Resistor network used as DC cable models

400 V laboratory supply used to model AC grids

The converters used in the experiment are two-level VSCs, see Table IV for relevant data. All converters are connected together at their DC sides using a resistor network. The DC cables are modelled as resistances with the same argument as for the simulation model. The resistor network for the laboratory set-up was built as part of [12] and makes it possible to achieve resistances in the range of 50-350 m per pole.

The motor-generator set is used together with a motor-drive to represent a wind farm. The 400 V laboratory power supply is used to model the AC grids in Norway, Germany and UK. The converters and the motor-drive are equipped with an interface which enables receiving status messages and measurements and sending control actions through the CAN-bus protocol. The control is achieved by using the Labview programming environment.

The control system for the 60 kVA laboratory converters is developed by SINTEF and is documented in [14]. It runs on a Xilinx Virtex5 FPGA-based processor system. Time critical parts are implemented as FPGA blocks while the rest is implemented as processor software routines.

Table I. Laboratory converter data [13].

Main supply voltage	0-400 V RMS (AC)
DC voltage	550-750 V
Rated Power	60 kVA
Rated current	100 A RMS (AC)
Switching frequency	maximum 7 kHz
LCL filter	500 H 50 F 200 H
DC filter capacitance	14 F

V. Implementation of droop control

The control system applied in this article consists of a cascaded control structure with one inner and one outer control loop. The inner loop is the standard vector current control [15]. The structure of the outer loop is different for the converters representing a country and the converter in the wind farm. For the converters representing a country, a voltage-droop control scheme is applied, whereas the wind farm converter is always delivering the available power (slave-node). It has been chosen to implement the voltage-droop scheme because it has a simple structure and low complexity. Also, although voltage droop control has been studied extensively in the literature, few works have showed experimental results [10][16].

It is possible to implement droop control directly acting on the inner current control loop [17]. Another alternative is to utilize a standard DC voltage controller, and let the droop control act on the DC voltage reference [3]. Since the laboratory converters used in this work already contains a closed loop DC voltage controller, it has been chosen to implement the droop control by modifying the DC voltage reference. The mathematical expression for the droop-line is given in Equation 1. and are the voltage and power set-points. Together with the droop constant , they form the droop line and the control system objective is to force the converter to have an operating point on the droop line.

(1)

In order to find the closed loop transfer function for the DC-voltage control, a relation between the d-axis current and the DC voltage is needed. A detailed circuit diagram of the VSC modelled by an average approach is given in Figure 4. Here, represents the AC grid voltage, is the converter voltage, and and make up the filter impedance. On the DC side, is the DC voltage, is the converter DC-side current, is the current flowing out of the terminals into the DC grid and is the current flowing into the DC-link filter capacitance. Using this figure and setting up Kirchoff's current law on the DC side gives:

(2)

The converter current and the current through the capacitor can be expressed by the DC-link voltage :

— – ——— (3)

By linearising and disregarding the impact from it can be shown that the relation between the d-axis current and DC voltage becomes [15]:

——— – —— (4)

Applying the Laplace transform gives:

– —— — (5)

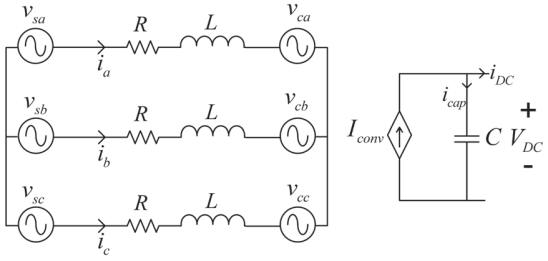

Figure 4. Average model of voltage source converter (VSC).

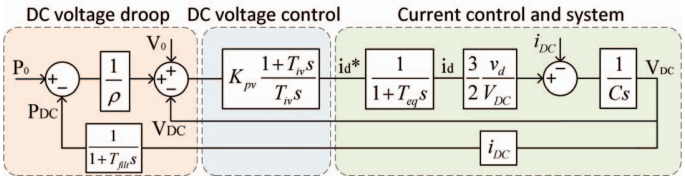

Figure 5. Block diagram of DC voltage droop control as it is implemented in the Simulink model.

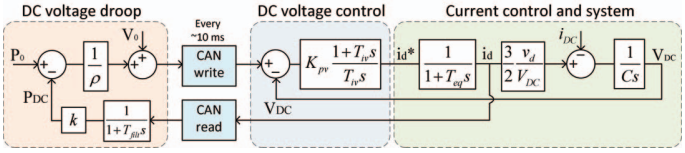

Figure 6. Block diagram of DC voltage droop control as it is implemented in the laboratory set-up.

The current control is tuned according to the modulus optimum criterion. The DC-voltage control parameters are found experimentally, and are adjusted in the simulation model in order to match the laboratory response.

The entire control loop can now be presented by using a block diagram. The block diagram in Figure 5 shows how this is implemented in the simulation model. The inner current control is represented as a first order response with an equivalent time constant .

The block diagram in Figure 6 shows how the droop is implemented in the laboratory experiment. There are two differences between this and the one describing the simulation model. Firstly, there is a time delay of approximately 10 ms due to the sampling time of the communication between the converters and Labview program. Secondly, real measurements of the power flowing through the DC terminals of the converters are not available with the present FPGA control card. Instead, the d-axis current is used, based on the assumption that the active power on the AC side is proportional with the d-axis current. The measured d-axis current is multiplied with a calibration constant in order to convert from current to power. The measured "power" is then withdrawn from the power set-point and divided with the droop constant. Adding the voltage set-point generated the DC voltage reference value, which is sent through the CAN bus and received by the converter.

VI. Case Studies

Three case studies are defined to investigate if the voltage droop control will ensure stable operation in the MTDC grid:

Abrupt variation in wind production

Sudden change in droop line set-points

Loss of two terminals during full wind production

Table II describes the droop-line characteristics for all converters during the case studies. For the case study where the power set-point is varied, the table gives the initial state of the system. The droop-line is identical for all converters representing a country. In practice, this means that the power produced by the wind farm will be shared close to equally between the countries, if the DC cable resistances are the same. The power production from the wind farm varies, and is specified for each case study. Table III gives the DC cable resistances between each country and the mid-point. In the resistor banks the resistances are set to be 150 but because of stray resistance in cables and bus contacts the resulting resistances are not equal and larger than the setting.

Table II. Droop-line characteristics for the converters representing a country during the three case studies.

Parameter	Symbol	Value
Voltage set-point		630 V
Power set-point		0 kW
Droop-constant		15 ———— (6.67 %)

Table III. Resistances in DC cables.

Distance	Resistance [ ]
Norway - Mid-point	180
Germany - Mid-point	182
UK - Mid-point	153

A. Case 1: Abrupt variation in wind power production

The system response is tested against abrupt variations in wind power production. The production is changed in steps according to Table IV. In the simulations steps in active power produced from the wind farm can be applied directly. In the laboratory model the power production can be changed by changing the motor-torque. This is done by using the motor-drive for the 55 kVA motor which is used to emulate wind power profiles.

Table IV. Wind power production profile for case 1

Time [s]	Wind power production [kW]
t=0	-2.0
t=1	4.4
t=6	16.5
t=11	38.5
t=16	4.4
t=21	27.5
t=26	-2.0

The simulation results show that the produced power from the wind farm is shared equally between the three countries, see Figure 7. This is because their respective droop lines have identical set-points and the resistances between the terminals are close to identical, see Table II and Table III. Figure 8 shows the resulting DC voltage and active power in the laboratory model during varying wind production.

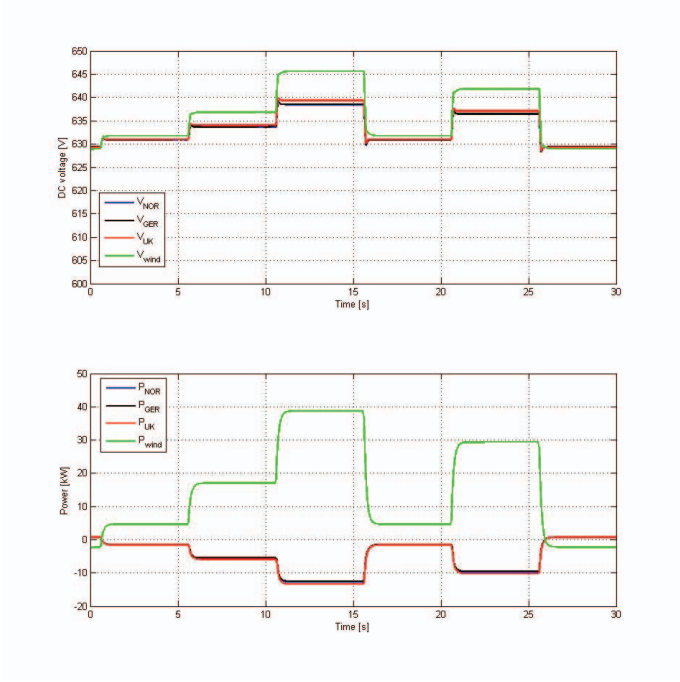

Figure 7. Simulation results for the case with varying wind farm power production. The graphs show voltage and power trajectories for Norway, Germany, UK and the wind farm.

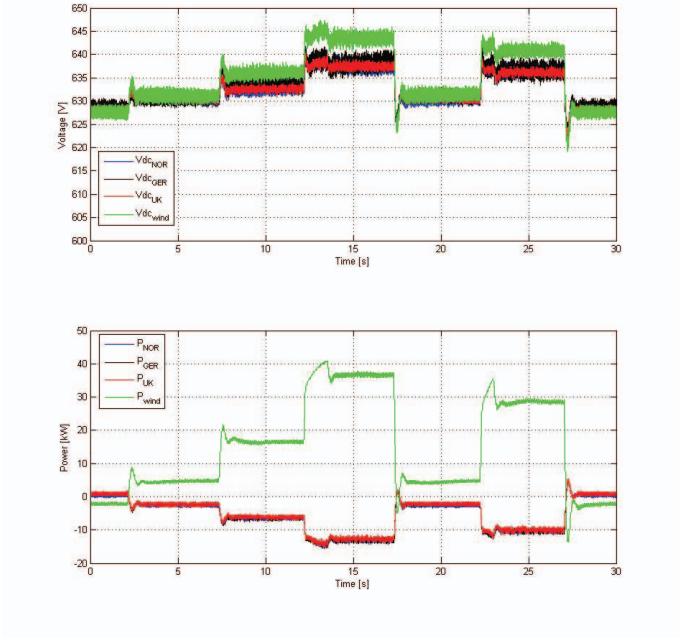

Figure 8. Laboratory results for the case with varying wind farm power production. The graphs show voltage and power trajectories for Norway, Germany, UK and the wind farm.

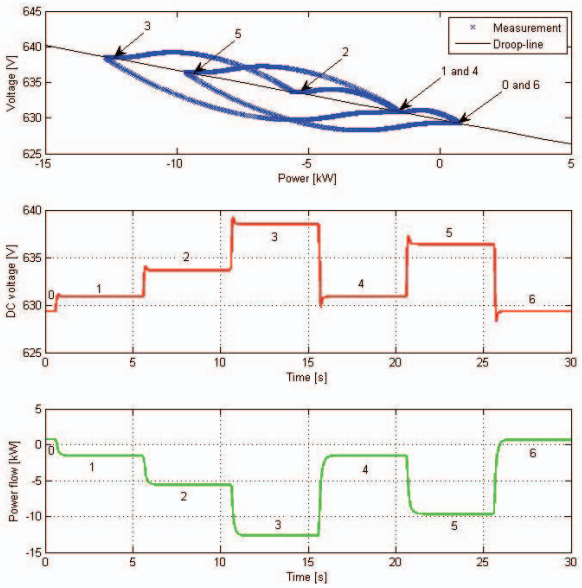

Figure 9. The middle and lower graphs show how the voltage and power varies with time in Norway during case 1. The upper graph shows how the voltage and power is moving along the droop-line.

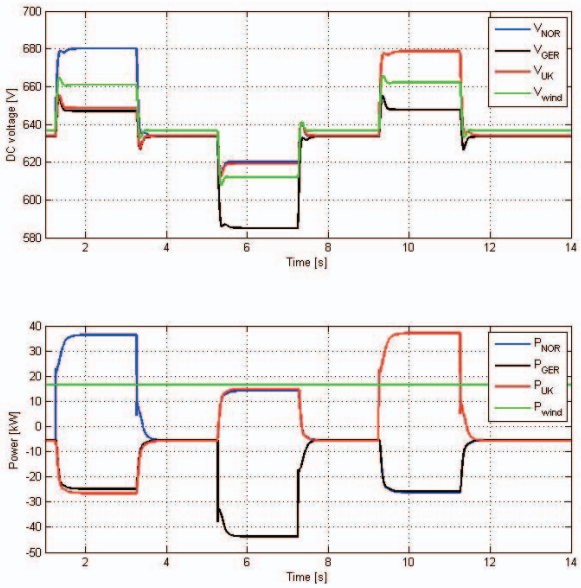

Figure 10. Simulation results when changing the power set-points for the droop-line for each converter.

The motor drive controller is not optimally tuned which results in an overshoot in the power production from the wind farm. Except from this overshoot, the match between the results from the simulations and experiment is good.

With changes in wind power production the nature of the voltage droop-control can be illustrated. Figure 9 shows a plot of the active power versus DC voltage during varying wind production in Norway. The droop-line has been included to show that the steady-state voltage and power always lie on the droop-line (points 0 to 6). There is a transient deviation in the transition between two steady-state points. This is due to the response time of the DC-voltage control systems.

B. Case 2: Sudden change in droop line set-points

Figure 10 shows how the DC voltage and active power change when changes in droop-line set-points are applied in the simulation model. The power set-point is changed in a step from its initial value to either or . This change is applied to each converter in turn, starting with the one representing Norway which has a positive step in its power set-point. This is followed by the converter representing Germany with a negative step, and finally in the UK-node with a positive step.

Even though a step of 1.8 p.u. in active power is requested, the actual step is 0.83 p.u. (50 kW). The reason why the active power does not reach its set-point value is the droop-line relation between power and voltage. When one of the converters has an increase in its power set-point its voltage will immediately increase. Because of the droop-lines the other converters will follow the voltage change by also increasing their DC voltage. The resulting power flow will be lower than in case of constant DC voltages. In other words, the droop-lines will counter-act the requested steps in power.

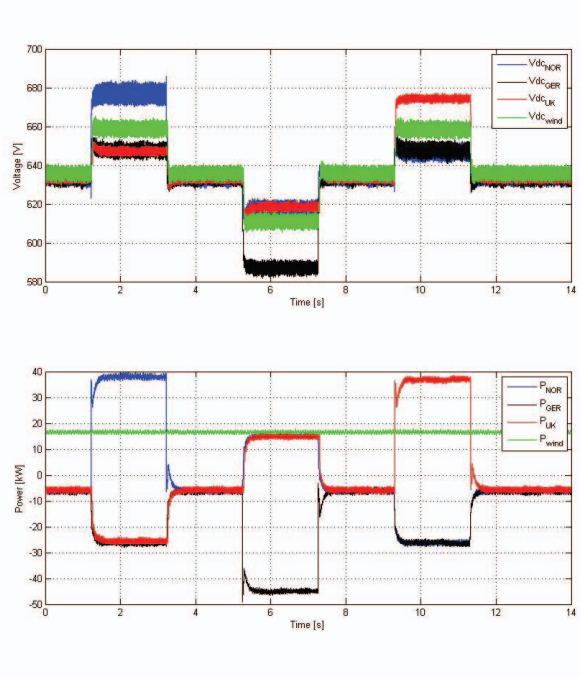

Figure 11. Measurments from the laboratory model when changing the power set-points for the droop-line for each converter.

Figure 11 shows how the DC voltage and active power change when changes in droop-line set-points are performed on each of the converters in the laboratory model. Due to the switches in the converters the measurements contain some ripple compared to the results from the simulations with the average model. The measurements are filtered with a sliding

window average every 1.6 milliseconds. Other than this, the match between the results for the experiment and the results from the simulations is good.

C. Case 3: Loss of two terminals during full wind production

A kind of ”worst case scenario” featuring loss of two converters during high wind power production is included in order to test if the system is able to ride through large disturbances. The wind farm is set to produce approximately 40 kW when the converter in Norway is disconnected at t=0.75 s. Two seconds later the converter in UK is also disconnected.

The event is simulated and the DC voltage and active power trajectories can be seen in Figure 12. While all converters are connected, the power produced by the wind farm is equally shared between the countries. This is because the droop-line characteristics are equal. When Norway is disconnected the power is shared between the remaining terminals. It can be seen that Germany imports all the power from the wind farm when it is the only terminal left connected.

The simulated system remains stable throughout the large disturbances. However, it should be noted that in a real system the power rating of the DC cable between the wind farm and Germany might not be the same as the rating of the wind farm. Such constraints in power have not been accounted for in the simulations or in the laboratory model. In practice it is important to not exceed any limits in either the converters or DC cables. In a situation when only one terminal is connected, a transmission limit could be withheld by decreasing the wind power production.

Figure 13 shows that the laboratory model also remains stable throughout the disconnection of the converters in Norway and Germany. It can be observed that the system dynamics are the same in the simulations and in the lab, but the steady-state values are not exactly the same.

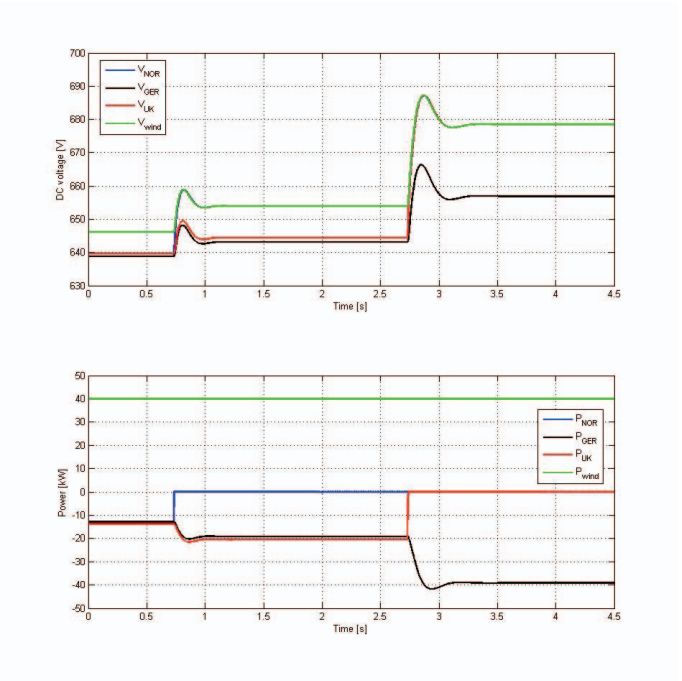

Figure 12. Simulation results showing voltage and power trajectories when loss of converter terminals during full wind production is analysed

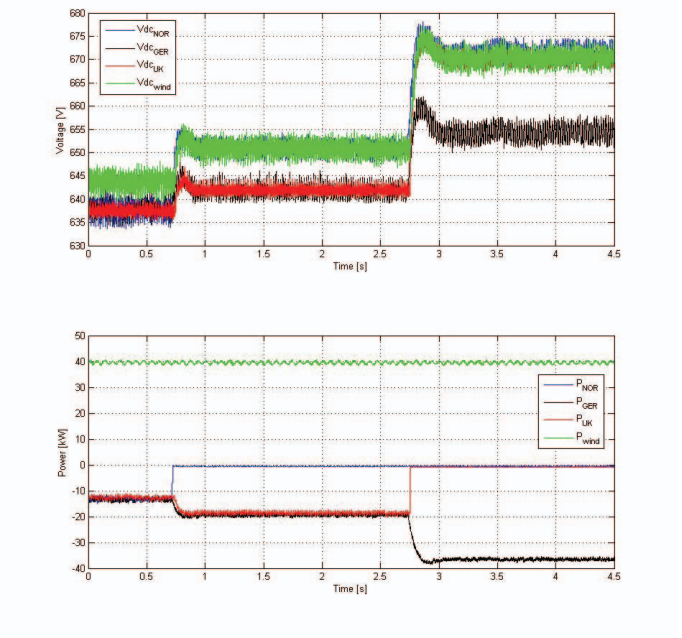

Figure 13. The voltage and power trajectories from the laboratory model when loss of converter terminals during full wind production is analysed

VII. Discussion

A. Is the comparison between simulation results and experimental results valid?

A model of the laboratory MTDC grid was built in Matlab/Simulink in order to evaluate the nature of the voltage-droop control and have an idea of what the performance of the control should be before it was implemented in the laboratory model. A comparison between the results from each model was made and the responses showed very good match. Some deviations between the results were however observed and a discussion is made in order to evaluate the sources of error that may be the reason why the results do not at all times match perfectly.

Firstly, the present version of the converter control system does not measure the power on any sides of the converters. Therefore, the d-axis current has been used as a replacement since it is assumed that it is proportional to the DC power. This relation is however not perfectly linear, and thus it may cause deviation between the results from the simulation model and the lab set-up. Secondly, the resistances used to model the DC cables are not constant. If the actual values of the resistances in the laboratory model are not the same as the values used in the simulation model, there will be a mismatch between the results from the two models.

B. Can the down-scaled MTDC laboratory model represent a real system?

The voltage-droop control has successfully been implemented on the converters in the laboratory model. The droop-control strategy acts as expected and the system remains stable throughout small and large disturbances. It is tempting to say that this shows that a MTDC grid in the North Sea would act the same. However, there are some sources of error that make it difficult to say that the behaviour of the down-scaled model can be equivalent to that of a real system.

Firstly, the DC-side filter capacitance in the voltage-source converters is relatively larger than it would be in a real system where cost-reduction is crucial. The large capacitance makes it easier to withhold the DC-voltage in the laboratory model than in a real system with a smaller amount of stored energy in the DC-filter and cable capacitances. This means that the experimental MTDC model may be more stable than a real MTDC system in the North Sea.

Secondly, the DC cables are modelled as resistances in the laboratory model, i.e. the cable inductance and capacitance are neglected. This means that the dynamic behaviour of the cable in the laboratory is not the same as it would be in a real system.

Lastly, the switching frequency of the 2L-VSCs in the lab is around 6 kHz, which is higher than it could be in a real system. HVDC converters are designed with a significantly lower switching frequency due to limitations in the semi-conductors. Using 6 kHz in the lab makes it possible to obtain a faster current control.

VIII. Conclusion

This work has demonstrated voltage droop control in a down-scaled laboratory model of a multi-terminal VSC-HVDC grid. The results have been compared with a corresponding simulation model in Matlab/Simulink. Three scenarios have been used to test the performance of the droop-control and evaluate the stability of the system:

Abrupt variation in wind power production

Sudden change in droop line set-points

Loss of two terminals during full wind production

Even though these scenarios are considered to be significantly tough to handle, the voltage-droop control strategy ensures that the voltages stay within their steady state limits and that the system reaches a stable operation point after a disturbance is applied. Further, the implemented converter control is independent on communication with the other nodes in the system, and it is indifferent to adding extra or removing terminals in the network. Thus, it can be concluded that the voltage-droop control scheme has been successfully implemented in both the simulation and laboratory model.

It has been discussed whether the down-scaled model is a good representation of a real MTDC system. Some sources of error have been analysed, but overall the laboratory model is assumed to give a good impression of the behaviour of an actual MTDC grid.

Acknowledgment

This work has been supported by the Norwegian Research Centre of Offshore Wind Technology (NOWITECH). In addition, the authors would like to thank Kalle Teearu, Tommy Berre, Kjell Ljøkelsøy, and others on SINTEF/NTNU that have contributed to the development of the laboratory set-up. Additional thanks go to Prof. Marta Molinas and Jon Are Suul for valuable guidance and encouragements towards publication of the results.

References

[1] Friends of the Supergrid, A Supergrid for Europe, [online] 2013, http://www.friendsofthesupergrid.eu/a-supergrid-for-europe.aspx (Accessed: 25.09.2013).

[2] The European Commission, An EU Energy Security and Solidarity Action Plan, [online] 2008, http://eur-lex.europa.eu/LexUriServ/LexUriServ.do?uri=COM:2008:0781:FIN:EN:PDF (Accessed: 25.09.2013).

[3] T. M. Haileselassie, K. Uhlen, "Precise Control of Power Flow in Multiterminal VSC-HVDCs Using DC Voltage Droop Control," in *IEEE Power and Energy Society General Meeting*, San Diego, CA, 2012. *Temesgen M. Haileselassie, Kjetil Uhlen, Member, IEEE*

[4] NSCOGI Working group 1, "Initial Findings - Grid Configuration", NSCOGI, 16.11.2012.

[5] D. V. Hertem, M. Ghandhari, "Multi-terminal VSC HVDC for the European supergrid: Obstacles", *ELSEVIER Renewable and Sustainable Energy Rev.*, vol. 14, no. 9, pp. 3156–3163, Dec., 2010.

[6] M. Callavik et al., "The Hybrid HVDC Breaker, An innovation breakthrough enabling reliable HVDC grids," ABB, Nov., 2012.

[7] T. K. Vrana, "System Design and Balancing Control of the North Sea Super Grid," Ph.D. dissertation, Dept. Electr. Eng., NTNU, Trondheim, Norway, 2013.

[8] A. Egea-Alvarez, J. Beerten, D. Van Hertem, O. Gomis-Bellmunt, "Primary and Secondary Power Control of Multiterminal HVDC Grids," *10th IET International Conference on AC and DC Power Transmission*, Birmingham, 2012, pp. 1-6.

[9] T. K. Vrana, J. Beerten, R. Belmans, O. B. Fosso, "A classification of DC node voltage control methods for HVDC grids," *Electric Power Systems Research*, vol. 103, pp. 137-144, Oct., 2013.

[10] A. Egea-Alvarez, F. Bianchi, A. Junyent-Ferré, G. Gross, O. Gomis-Bellmunt, "Voltage Control of Multiterminal VSC-HVDC Transmission Systems for Offshore Wind Power Plants: Design and Implementation in a Scaled Platform," *IEEE Trans. Ind. Electron*, vol. 60, no. 6, pp. 2381-2391, June, 2013.

[11] SINTEF, SINTEF Renewable Energy System Laboratory, http://www.sintef.no/home/SINTEF-Energy-Research/Laboratory-Services-/Renewable-Energy-System-Laboratory/ (Accessed: 15.11.2013).

[12] K. Teearu, "Laboratory Testing of Multi-terminal VSC-HVDC," M.S. thesis, Dept. Electr. Eng., NTNU, Trondheim, Norway, 2013.

[13] K. Ljøkelsøy, "Project memo - 60 kVA Laboratory converter unit. Documentation.," SINTEF, Dec., 2010.

[14] K. Ljøkelsøy, "Project memo - Control system for a three-phase grid connected converter," SINTEF, Nov., 2013.

[15] C. Bajracharya, M. Molinas, J. A. Suul, T. M. Undeland, "Understanding of tuning techniques of converter controllers for VSC-HVDC," *Proceedings of the Nordic Workshop on Power and Industrial Electronics*, Helsinki, 2008.

[16] A. Egea-Alvarez, et al., "Experimental implementation of a voltage control for a Multiterminal VSC-HVDC offshore transmission system, *3rd IEEE PES International Conference and Exhibition on Innovative Smart Grid Technologies*, Berlin, 2012, pp. 1-7.

[17] R. T. Pinto et al., "Comparison of direct voltage control methods of multi-terminal DC (MTDC) networks through modular dynamic models," *Proceedings of the 14th European Conference on Power Electronics and Applications*, Birmingham, 2011, pp. 1-10.